2020

Cosmic-Ray Acceleration in the Cygnus OB2 Stellar Association

Binita Hona
Michigan Technological University, bhona@mtu.edu

COSMIC-RAY ACCELERATION IN THE CYGNUS OB2 STELLAR ASSOCIATION

By

Binita Hona

A DISSERTATION

Submitted in partial fulfillment of the requirements for the degree of

DOCTOR OF PHILOSOPHY

In Physics

MICHIGAN TECHNOLOGICAL UNIVERSITY

2020

This dissertation has been approved in partial fulfillment of the requirements for the Degree of DOCTOR OF PHILOSOPHY in Physics.

Department of Physics

Dissertation Advisor:	*Dr. Petra Huentemeyer*
Committee Member:	*Dr. David Nitz*
Committee Member:	*Dr. Brian Fick*
Committee Member:	*Dr. Qiuying Sha*
Department Chair:	*Dr. Ravindra Pandey*

Contents

List of Figures

List of Tables

Acknowledgments

There is a long list of people without whose help in my journey as a PHD student, this dissertation would not have been possible.

First, my deepest gratitude to my advisor Petra Huentemeyer for introducing me to the field of gamma-ray astrophysics. Not only you taught me everything I know about gamma-ray astrophysics but also on how to present my work and how to make my voice heard. I have been extremely fortunate to work with you, the best mentor I had. Thank you for all the support and encouragement.

I am deeply grateful to Henrike Fleischhack for countless help and guidance every step of the way. You always had time to answer my dumb questions and to lend your expertise even in your busiest hours.

I would like to thank all of my group members here at MTU. It has been a wonderful experience working together and most of what I learned about the gamma-ray sources came from our passionate discussion during the group meetings.

I also wish to thank my thesis committee: Dr. David Nitz, Dr. Brian Fick and Dr. Qiuying Sha for their feedback on my thesis.

I am indebted to the HAWC collaboration for many questions and suggestions during the presentations, paper draft/proceedings review and via slack messages that kept me motivated throughout my studies. My special thanks to to Sabrina Casanova and Ke Fang for helping me immensely with the physics interpretation of the Cocoon results and making time to have meetings at their oddest hours.

It would be impossible to be where I am at without the help from a number of friends. I am very grateful to Rakshya Khatiwada, Smita Raithore and Sandamali Weerasooriya for keeping me inspired. Our chats ranging from our frustrations, hopes, Physics and Philosophy always left me re-energized and optimistic.

Last but not the least, I would like to thank my family. No words can convey my gratitude for my parents: my mom, Guna Maya Hona and my dad, Krishna B. Hona, who always believed in me. I am extremely fortunate and thankful for Sunil Hona, Sabina Awal, Subin Hona, Grishma Shakya, Renuka Hona and Abhishek Dhungana for being my cheerleaders. Thank you Shawon, my partner for always being there for me. As a PHD student yourself, I am extremely grateful that I had someone so close in this journey together.

Dedication

This dissertation is dedicated to my late grandmother, Hera Maya Hona.

List of Abbreviations

ARGO-YBJ	Astrophysical Radiation with Ground-based Observatory at YangBaJing
BPL	Broken Power Law
CR	Cosmic Ray
GCR	Galactic Cosmic Ray
DAQ	Data Acquisition
eV	Electron Volt
Dec	Declination
EAS	Extensive Air Shower
LAT	Large Area Telescope
GP	Ground Parameter
HAWC	High-Altitude Water Cherenkov
HE	High Energy
HEGRA	High-Energy-Gamma-Ray Astronomy
H.E.S.S	High Energy Stereoscopic System
IACT	Imaging Atmospheric (or Air) Cherenkov Telescope
LE	Low Energy
LHAASO	Large High Altitude Air Shower Observatory

MAGIC	Major Atmospheric Gamma Imaging Cherenkov Telescopes
NKG	Nishimura-Kamata-Greisen
NN	Neural Network
PE	Photoelectron
PL	Power Law
PLC	Power Law with an exponential Cut-off
PMT	Photo Multiplier Tube
PSF	Point Spread Function
PWN	Pulsar Wind Nebula
RA	Right Ascension
SED	Spectral Energy Distribution
SFCF	Super Fast Core Fit
SFR	Star Forming Region
SNR	Supernova Remnant
SWGO	Southern Wide Field-of-view Gamma-ray Observatory
TDC	Time-to-Digital-Converter
threeML	Multi-Mission Maximum Likelihood framework
ToT	Time over Threshold
TeVCat	TeV Catalog
VERITAS	Very Energetic Radiation Imaging Telescope Array System
VHE	Very High Energy

WCD	Water Cherenkov Detector

Abstract

The Cygnus region of our Galaxy consists of an active star forming region and a wealth of various astrophysical sources such as pulsar wind nebulae (PWN), supernova remnants (SNRs), and massive star clusters. Massive stellar clusters and associations have been postulated as possible sources of cosmic rays (CRs) in our Galaxy. One example of a gamma-ray source associated with a stellar association lies in the Cygnus region known as the "Cygnus Cocoon". It is an extended region of gamma-ray emission in the Cygnus X region and attributed to a possible superbubble with freshly accelerated CRs which are hypothesized to produce gamma rays via interaction with the ambient gas nuclei. The emission region is an environment of lower particle density and is surrounded by ionization fronts like a carved-out cavity or a cocoon.

CRs in the Cocoon could have originated in the OB2 association and been accelerated at the interaction sites of stellar winds of massive type O stars. So far, there is no clear association at TeV energies. In the study presented in this thesis, I used data collected by the HAWC Observatory over 1038 days to disentangle the TeV gamma-ray emission from 2HWC J2031+415, a source which was previously reported in the 2nd HAWC catalog and is collocated with the Cygnus Cocoon, into two components: a pulsar wind nebula and the Cygnus superbubble. The contribution from the Cygnus superbubble is detected at a significance level of $\sim$12 σ with maximum photon energies

above 100 TeV, the highest measured yet. Based on the spectrum and morphology of gamma-rays across six decades of energy, and the non-detection of radio and X-ray photons from this region, the gamma-rays are plausibly of a hadronic origin. There is a spectral softening above 1 TeV, which can be explained by two hadronic scenarios. Either there is a leakage of CRs from the superbubble resulting in a spectral break from GeV to TeV or the spectral softening is due to cut-off energy, an upper limit to the particle acceleration by the stellar winds.

Chapter 1

Introduction

Our understanding about the universe is derived from years of observations and study of the light and the particles. γ-ray Astrophysics studies the universe through the highest energy electromagnetic radiation spectrum, shown in Fig. 1.1, to learn about the non-thermal processes in the most extreme astrophysical environment. The energy range (beyond 10^8 eV) of γ-ray observation covers more than eight decades. Because of the wide energy range, a range of observation techniques are required. In general, the γ-ray energy band is divided into low energy (LE) covering (0.1-100) MeV, [1] high energy (HE) covering (0.1-100) GeV, very high energy (VHE) covering (0.1-100) TeV and ultra high energy (UHE) covering beyond 100 TeV energy [2]. This thesis will focus on γ-ray astrophysics at HE and beyond.

[1] for the eV conversion to MeV, GeV and TeV see the appendix A

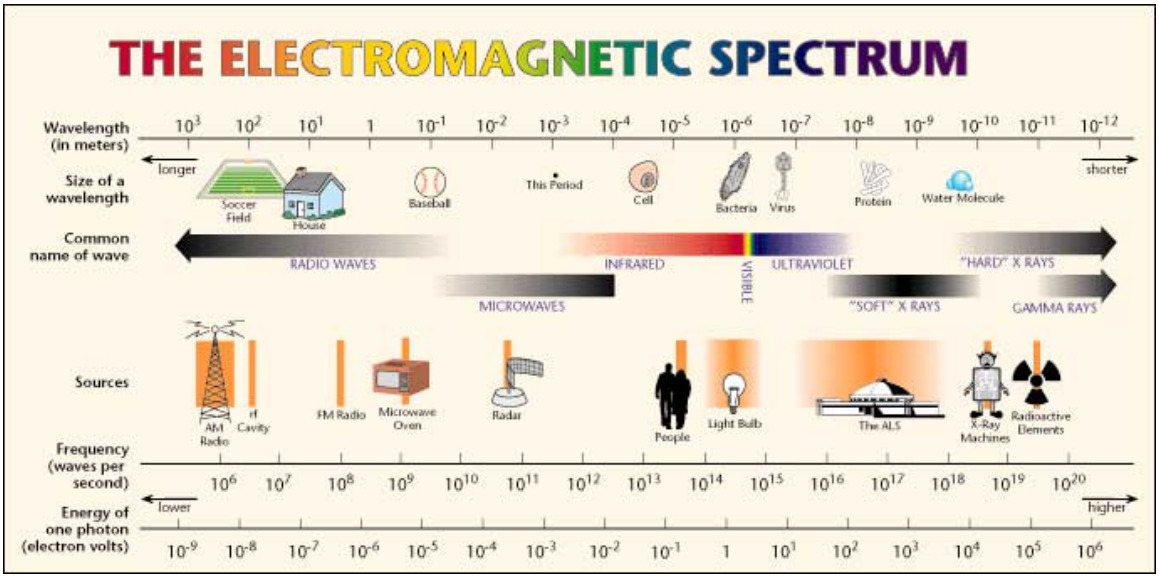

Figure 1.1: The electromagnetic spectrum from http://son.nasa.gov/tass/content/electrospectrum.htm. Image Credit: NASA.

Through the study of γ-ray emission at HE and beyond, we learn about the origin, propagation and acceleration of the highest energy cosmic rays (CRs) in our Galaxy. CRs are the ionized atomic nuclei travelling with the speed almost equal to the speed of light. A large fraction of the CRs consists of Hydrogen nuclei (protons) ($\sim$89%), $\sim$10% Helium nuclei and $\sim$1% nuclei of heavier elements. A small fraction (1%) of the Galactic CRs (GCRs) are electrons.

They were first discovered in the year 1912 by V.F. Hess [18] for which he was awarded the Nobel Price in 1936. The CR spectrum is approximately described by exponentially decreasing function shown in Fig. 1.2. At $\sim 3 \times 10^{15}$ eV, known as the knee region, the flux starts to decrease more steeply. Up to the knee, the flux is attributed predominantly to the Galactic source population and this feature might be an indication of the maximum acceleration energy of Galactic sources [19]. At $\sim 5 \times 10^{18}$

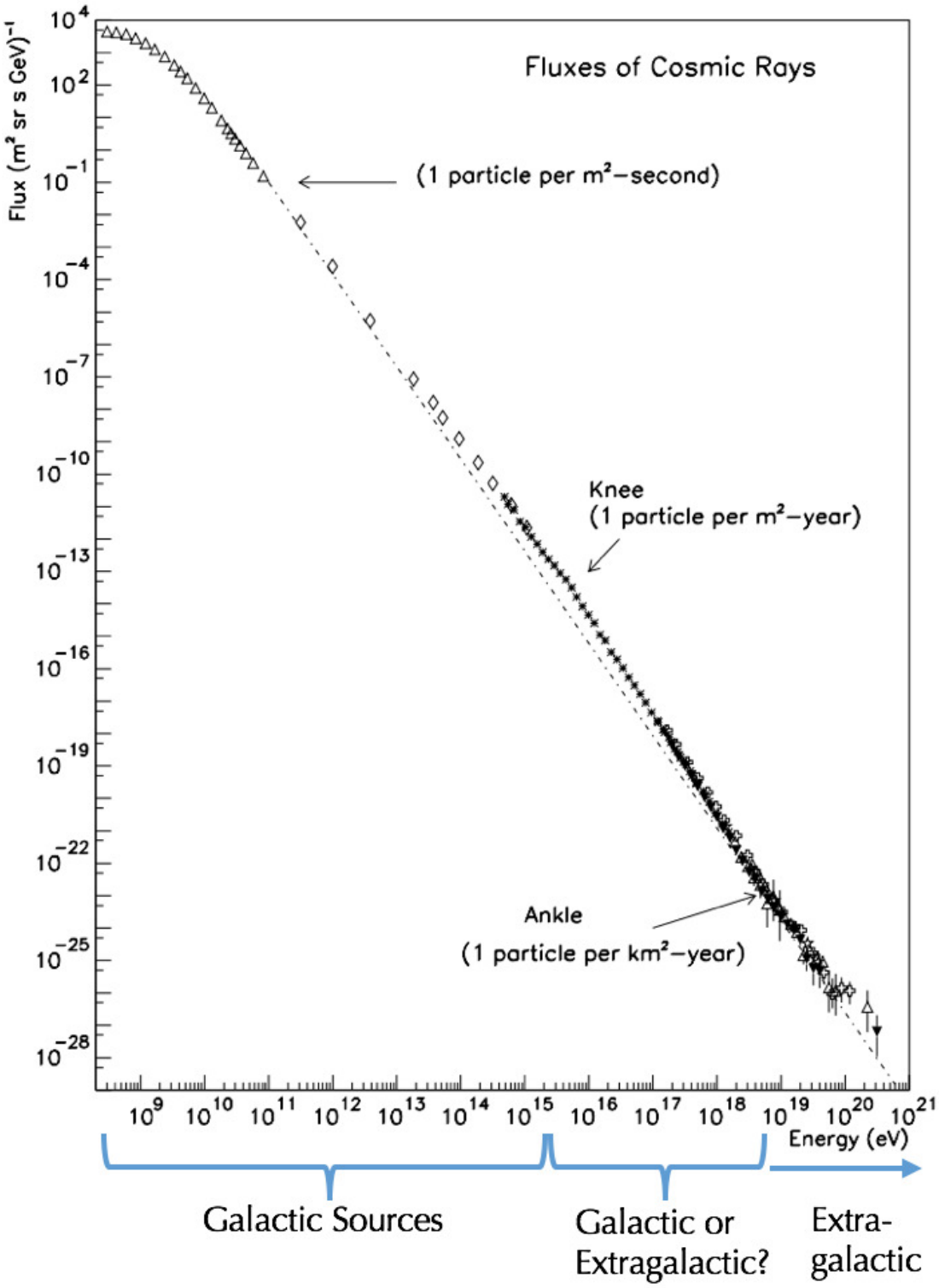

Figure 1.2: Distribution of CR flux as a function of energy adopted from https://link.springer.com/article/10.1023/A:1013828611730 S.P. Swordy.

eV, the spectrum flattens and the corresponding feature is called ankle. The CR flux beyond the ankle is thought to be from extra-galactic sources. The energy range between the knee and the ankle feature indicates the transition from Galactic to extra-galactic sources [19].

In our Galaxy, CRs are hypothesized to be accelerated up to a few PeV [20]. However, even after a century of their discovery, the physics behind the processes that can impart such high energy to a CR charged particle is not understood in detail and understanding them has become one of the main challenges of Galactic Astrophysics. Since Galactic CRs are charged particles, they are deflected in the magnetic field of the galactic medium throughout their path of travel. Hence, they no longer have the directional information of the sources, where they originate. These accelerated charged particles produce gamma rays via interactions with the interstellar medium in the vicinity of their acceleration sites, which then travel without deflection by galactic magnetic fields. Therefore, by studying gamma rays, we probe the origin of the highest energy CRs in our Galaxy along with their acceleration and propagation mechanisms. In γ-ray astrophysics, the search for the astrophysical sources/source type which can explain the very high PeV acceleration of the CR rays is intense. Stellar associations in a star forming regions have been postulated as a possible sites/sources of up to PeV acceleration

One such region of γ-ray emission associated with the stellar association has been

detected at GeV energies in the Cygnus constellation. This thesis provides the detailed spectral and morphological analysis of γ-ray emission from the direction of the Cygnus constellation with 1038 days data collected with the HAWC Observatory along with the combined spectral study using data points of the Fermi-Large Area Telescope (LAT) to offer a deeper understanding of the region across six decades of energy.

The first two chapters (1) and (2) introduce the field of γ-ray astrophysics, γ-ray production mechanisms, γ-ray sources and what I my work will add to the field; the motivation behind this analysis. The third chapter (3) describes the various aspects of the HAWC detector and how the raw data collected by the instruments are processed before the data analysis steps. The fourth chapter (4) discusses what we call the Cygnus region (the area in the sky collocated with the Cygnus constellation), a unique discovery in the region called the Cygnus Cocoon and its multi-wavelength observations. Before diving into the HAWC observations, the fifth chapter (5) describes the various statistical modelling and the comparison methods used in the analysis of the HAWC data for this study.

The sixth chapter (6) is the longest chapter which details the disentanglement of the emission region of the source 2HWC J2031+415 previously detected by HAWC into two sources: the Cygnus Cocoon and a Pulsar Wind Nebula (PWN). The chapter

describes the morphology of the Cocoon at TeV energies, its spectral energy distribution and offers an interpretation of the results in terms of particle acceleration and propagation by and near Star Forming Regions (SFRs). The final short conclusion chapter (7) summarizes the results and provides an outlook on possible avenues for future studies.

Chapter 2

VHE γ-ray emission

2.0.1 Acceleration of Cosmic Rays

There are certain mechanisms in the astrophysical objects which allow the transfer of energy to CRs resulting in the CR acceleration to relativistic energies. First order Fermi acceleration or diffusive shock acceleration as illustrated in Fig. 2.1 was proposed as an efficient mechanism for the CR acceleration. The acceleration mechanism is collisionless and energy gain happens via crossings the shock front resulting in the energy gain linear in the shock velocity. Shock waves are the discontinuities created between regions by disturbances in the gas propagating with a velocity higher than the speed of sound. Such shock waves are produced in the various astrophysical systems such as the stellar winds, SNRs and other similarly disturbed environments.

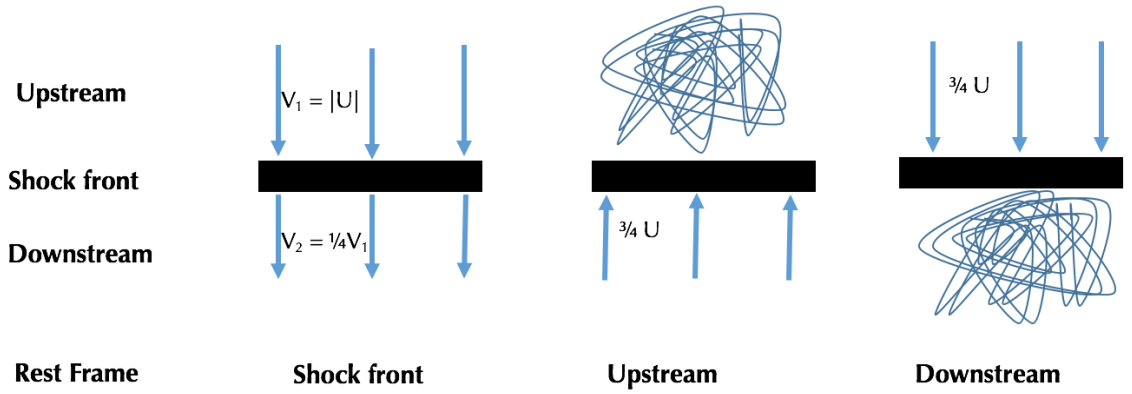

Figure 2.1: Schematic of the dynamics of high energy particles near the shock wave propagating at a velocity U adopted from [1]. **left**: It depicts the flow of the interstellar gas observed in the reference frame in the rest frame of the shock front. The upstream gas is moving into the shock with velocity V_1 while the downstream gas is moving away with velocity V_2. **middle**: The flow of gas in the reference frame in which the upstream gas is at rest. Due to the scatterings, the high energy particles distribution is isotropic in the upstream frame. The downstream gas is diffusing towards the shock with velocity 3/4 U and the shock is propagating with velocity U. **right**: The flow of gas in the reference frame in which the downstream gas is at rest. Vice-versa of the middle scenario.

High energy particles present in the astrophysical shock environment stream through the upstream and downstream region and in the process are scattered by irregularities in the magnetic field and plasma density. The random scatterings will result in the isotropic velocity distribution of the particles in the reference frame of the moving fluid on either side of the shock. When these high energy particles cross from upstream to downstream and vice-versa, at each crossing, the particles gain a net energy until the energy gain from the multiple crossing is high enough to escape [1, 21].

Let us define the average energy (E) of a particle in one shock crossing in term of constant β, $E = \beta E_0$, where β is fractional energy gain per crossing. Let us further

define that the probability of a particle remaining in the acceleration region after one crossing is P. Then, after k crossings, the number of the particles in the acceleration region is $N = N_0 P^k$ with energies $E = E_0 \beta^k$. From these two quantities, we can derive,

$$\frac{N}{N_0} = \left(\frac{E}{E_0}\right)^{lnP/ln\beta} \tag{2.1}$$

Some fraction of N will further accelerate to even higher energies. Eq. 2.1 can be written as a function of energy with $N(E)$ as the number of high energy particles with energy $\geq$E,

$$N(E)dE \propto E^{-1+(lnP/ln\beta)}dE \tag{2.2}$$

The detailed derivation for the value of β and P is presented in [1]. The shock front as illustrated in the Fig. 2.1 is moving with velocity U, which is much less than the velocity of the particles, propagating near the speed of light. In the rest frame of the upstream gas, the downstream gas flows toward the shock at the velocity $V = (3/4)U$ and vice versa. An relativistic upstream particle crossing the shock-front has an energy gain $\frac{2}{3}V/c$. In one complete trip from the upstream to downstream and back again, it has an average energy gain of $\frac{4}{3}V/c$ [1]. Therefore, β is given by

$$\beta = \frac{E}{E_0} = 1 + \frac{4V}{3c} = 1 + \frac{U}{c} \tag{2.3}$$

The probability that the particle will make it back to upstream once it crosses the downstream region is $P = 1 - U/c$ [1].

Hence, we have

$$lnP = ln\left(1 - \frac{U}{c}\right) = -\frac{U}{c} \tag{2.4}$$

and

$$ln\beta = ln\left(1 + \frac{4V}{3c}\right) = \frac{U}{c} \tag{2.5}$$

Substituting the values for ln β and ln P in Eq. 2.2 gives

$$N(E)dE \propto \times E^{-2}dE \tag{2.6}$$

It results in the power law energy distribution with spectral index of -2 for CRs [21]. This -2 index is harder in comparison to -2.7 spectral index obtained for the GCRs up to the knee region as shown in Fig. 1.2. The propagation effects such as energy losses of CRs impacts the spectral energy distribution resulting in the observed softer spectral index of -2.7 for the GCRs.

2.1 γ-ray Production Mechanisms

The primary products of cosmic accelerators are the CRs which are accelerated to very high energies. These accelerated particle then produce gamma rays as the secondary products via hadronic or leptonic processes. It is difficult to distinguish between two origins of the γ-ray emissivity. According to Aharonion, the detection of a harder γ-ray spectrum favors hadronic origin [22]. However, a detailed particle modeling of the emission region is required to distinguish the hadronic or leptonic origin of gamma rays.

2.1.1 Hadronic Origin

In case of hadronic processes, the accelerated particles are protons or nuclei which interact with nuclei of the ambient medium resulting in pion production. During the process, neutral pions (π^0) and charged pions ($\pi^{\pm}$) are produced with the same probability. Compared to the charged pions which have a lifetime of $\sim 2.6 \cdot 10^8$ s, the neutral pions have a much shorter lifetime of $\sim 10^{-16}$ s. The latter will decay into γ-ray photons. The branching ratio for decaying into two photons 99% and 1% for decaying into $e^+e^-\gamma$. As for the charged pions, they will eventually decay into electrons and neutrinos; $\pi^+ \rightarrow \mu^+\nu_\mu \rightarrow e^+\nu_e\overline{\nu}_\mu\nu_\mu$.

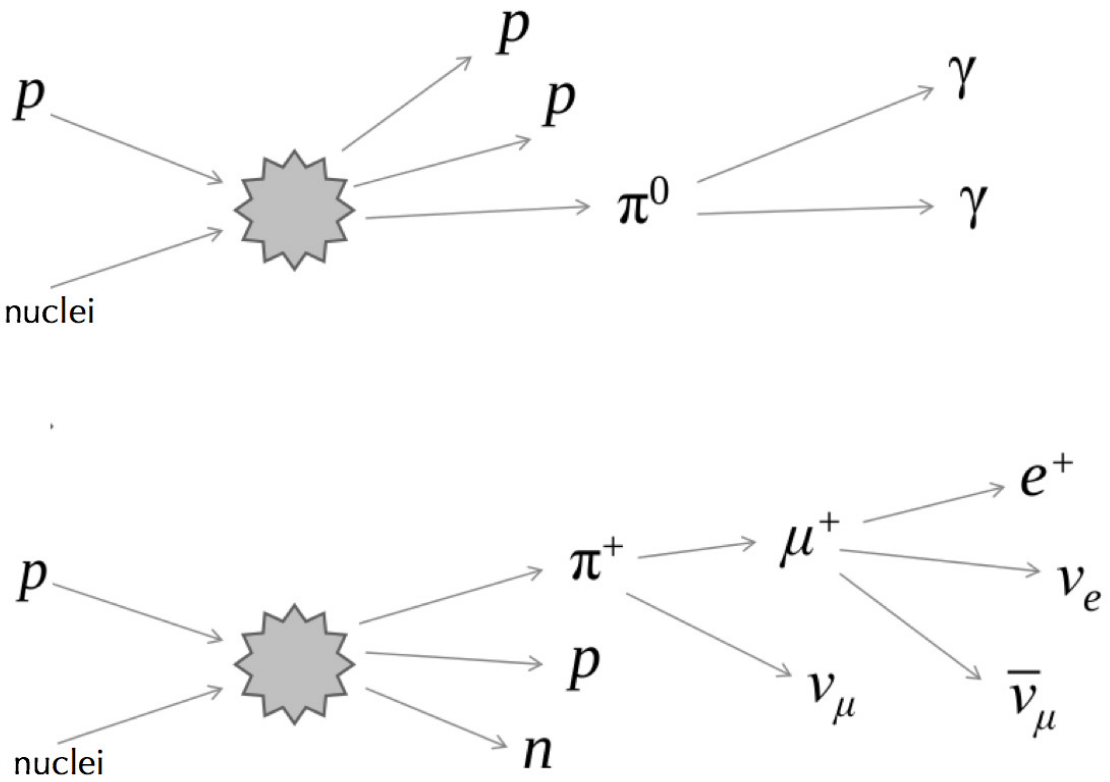

Figure 2.2: Schematic of pion decay channels in proton-nuclei interaction

The γ-ray emissitivity from the neutral pion decay can be calculated as [22]:

$$q_\gamma(E_\gamma) = 2\int_{E_\pi^{min}(E_\gamma)}^{\infty} dE_\pi \frac{q_\pi(E_\pi)}{\sqrt{E_\pi^2 - m_\pi^2}} \tag{2.7}$$

where $E_\pi^{min}(E_\gamma)$ is the minimum energy of a π^0 decaying into photons with energy E_γ and is calculated from kinematics as $E_\pi^{min}(E_\gamma) = E_\gamma + m_\pi^2/4E_\gamma$. The function $q_\pi(E_\pi)$ is the π^0 spectrum produced in the hadronic scenario and is described as,

$$q_\pi(E_\pi) = 4\pi n_H \eta \int_{E_p^{min}(E_\pi)}^{\infty} dE_p J_p(E_p) \frac{d\sigma_\pi(E_\pi, E_p)}{dE_\pi} \tag{2.8}$$

where $E_p^{min}(E_\pi)$ is the minimum energy for the CR proton determined by kinematics. $J_p(E_p)$ is the CR proton flux and n_H is the gas density of the ambient medium. The parameter η is defined as the factor for the π^0 production from the channels involving heavier than proton, CR nuclei and the ambient gas. The expression $\frac{d\sigma_\pi(E_\pi, E_p)}{dE_\pi}$ is the differential cross section for a proton of energy E_p to create a π^0 of energy $E(\pi)$.

2.1.2 Leptonic Origin

As the name suggests, in this process, γ-rays originate from the accelerated leptons via different mechanisms.

2.1.2.1 Inverse Compton Scattering

At TeV energies, Inverse Compton Scattering is the dominant leptonic process. Relativistic electrons scattering off low energy photons, for example from the cosmic microwave background, transfer part of their energy to the low energy photons and thus turning them in γ-ray photons.

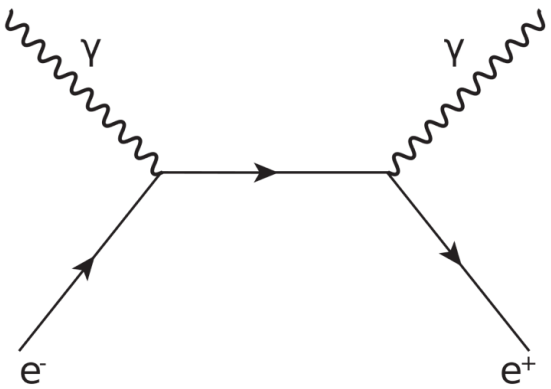

Figure 2.3: Feynman diagram of inverse Compton scattering

For $E_e E_\gamma << m_e^2 c^4$, the cross section for this process is given by the Thomson cross-section, $\sigma_T = \frac{8}{3}\pi r_e^2$, where r_e is the classical radius of the particle. For $E_e E_\gamma \sim m_e^2 c^4$, the cross section for the Inverse Compton process is given by the Klein-Nishina formula. For the ultrarelativistic electrons, the Klein-Nishina cross section is [1]

$$\sigma_{KN} = \pi r_e^2 \frac{1}{\epsilon}\left(ln2\epsilon + \frac{1}{2}\right) \tag{2.9}$$

where $\epsilon = \frac{E_\gamma}{m_e c^2}$. The parent electrons suffer large energy losses and the maximum energy gain by the low energy photons can be calculated by $E_{max} \sim 4\Gamma^2 E_\gamma$. For Lorentz factors of $\Gamma \sim 10^2 - 10^3$, keV photons from the cosmic microwave background can be upscatttered into GeV-TeV photons.

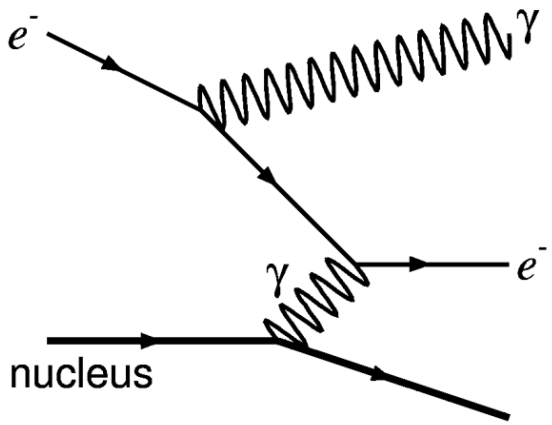

Figure 2.4: Feynman diagram of Bremsstrahlung.

2.1.2.2 Bremsstrahlung

Bremsstrahlung, also known as braking radiation, is the process in which an electron deaccelerating in an electric field of the ISM loses energy and emits γ-ray photon. If an electron (e^-) with speed c passes a proton of mass m_p in an ambient gas, the average energy loss rate by the electron can be calculated as

$$-\left(\frac{dE_e}{dt}\right) = \left(\frac{cm_p n}{X_0}\right) E_e \tag{2.10}$$

where n is the number density of the ambient gas medium and X_0 is the radiation length which is inversely proportional to the cross section of the interaction.

2.2 Galactic γ-ray Sources

Various regions of γ-ray emission have been studied and based on the Physics processes have been associated with different astronomical objects. One fifth of the $\sim$ 200 TeV γ-ray sources[1] lack a clear relation with objects at other wavelenghts [3]). Out of the known Galactic particle accelerators, I have provided a brief description of three source types relevant to this thesis in the following section

2.2.1 Supernova Remnants (SNRs)

When a massive star ($M_{star} \geq 8M_{\odot}$) runs out of fuel required for the fusion reactions to counteract the gravitational pressure, the stellar core collapse ejecting the stellar material releasing an energy of the order $\sim 10^{44}$ J. This process is called a supernova explosion. The ejected material in the process forms an expanding structure as it sweeps up interstellar material along its way and this is known as a SNR. While the explosion last for only about a few order of seconds, the expansion of the SNR shell continues up to $\sim$ 30,000 years before finally merging with the ISM. Along its expansion timeline, as this expanding shell sweeps up the surrounding gas, strong shocks form and accelerate the charged particles in the SNR environment to very

[1] `http://tevcat.uchicago.edu/`

high energies. The famous example of a SNR is the Crab nebula, the brightest γ-ray source. Chinese, Japanese and likely the native Americans recorded the explosion event 1,000 years ago in 1054 AD [2]. It is regarded as the standard candle in the field of γ-ray astrophysics.

Among the different sources of CRs, SNRs have been postulated to be the dominant sources of CRs in our Galaxy. To maintain the energy density of the GCRs, an estimated power of $0.3 - 1 \times 10^{41} \mathrm{erg\,s^{-1}}$ is required to be supplied by the CR source population [23]. The mechanical energy released per SN explosion is of the order of 10^{51} erg and multiplying this energy with SN explosion rate in the galaxy i.e. about 3 per century results in available power of $10^{42} \mathrm{erg\,s^{-1}}$ from the SN explosion[24]. Thus, an acceleration process amounting to 10% efficiency for conversion of the kinetic SN energy to CR energy is required. While the studies of SNRs confirm the acceleration of particles up to a few hundreds of TeV, the cutoffs in the γ-ray spectra of SNRs at several TeV until now provide no firm evidence that SNRs accelerate particles up to PeV energy [25].

2.2.2 Star Forming Regions

Other than SNRs, Star Forming Regions (SFRs) in different phases of their evolution have been speculated to be possible galactic CR acceleration sites [26]. There are

[2] https://hubblesite.org/image/3885/category/35-supernova-remnants

four processes by which electrons and protons can be accelerated in an SFR. When an SFR is in an early stage, a massive protostar or a collection of protostars are present embedded in molecular clouds. Radio observations of protostars reveal thermal elongated jets. Strong shock waves created at end of the jets can accelerate charged particles [27]. The maximum energy to which particles are accelerated by these shock waves at the terminal ends is 3 TeV for the electrons and 60 TeV for the protons [27]. Another process for particle acceleration could be due to colliding wind binaries after early massive stars are formed. When the strong winds of these stars collide with terminal velocities, strong shocks are created [28]. Thus, these colliding wind binaries can then accelerate electrons and protons via diffusive shock acceleration to the MeV-GeV energy range [27]. As the SFR evolves into stellar clusters and associations, CRs can be accelerated via two different ways. The interaction of supersonic winds of these stars in the clusters creates a collective bubble called superbubble. Strong shock waves are formed at the interaction sites of the stellar winds and can accelerate charged particles up to PeV energy [29, 30]. The particles are accelerated via diffusive shock acceleration mechanism at the wind boundary [26]. Other than the collective effect of strong winds, SN explosions of the massive stars after a few Myrs can also contribute additional kinetic energy to accelerate charged particles [31]. An example of a stellar association as a CR accelerator, the OB2 association is discussed in the Chapter 4.

2.2.3 Pulsar Wind Nebulae

Pulsar Wind Nebulae (PWNe) are powered by Pulsars and emit gamma rays. Pulsars are rapidly-rotating, highly-magnetic neutron stars (NS), remains of collapsed cores of massive stars after a supernova explosion. They can be modelled as non-aligned rotating magnets with large magnetic dipole moments surrounded by a magnetized region called the magnetosphere [1]. Since pulsars are rotating magnetized neutron stars, they release their rotational energy in the form of EM emission or high-energy particles such as electron and positrons [32]. The emitted power is given by

$$\dot{E} = -\frac{dE}{dt} = 4\pi^2 I \dot{P} P^{-3} = I\Omega\dot{\Omega} \tag{2.11}$$

where I is moment of inertia, P is the rotation period and $\Omega = 2\pi/P$ is the angular frequency of rotation of the pulsar. Similarly, the characteristics age of the pulsar is given by [33].

$$\tau_c = \frac{P}{2\dot{P}} \tag{2.12}$$

High-energy particles are accelerated by the large electric fields in the magnetosphere which then produce electromagnetic cascades. As a result, there is a relativistic outflow of a dense $e^{\pm}$ wind originating from the magnetosphere and terminating in the

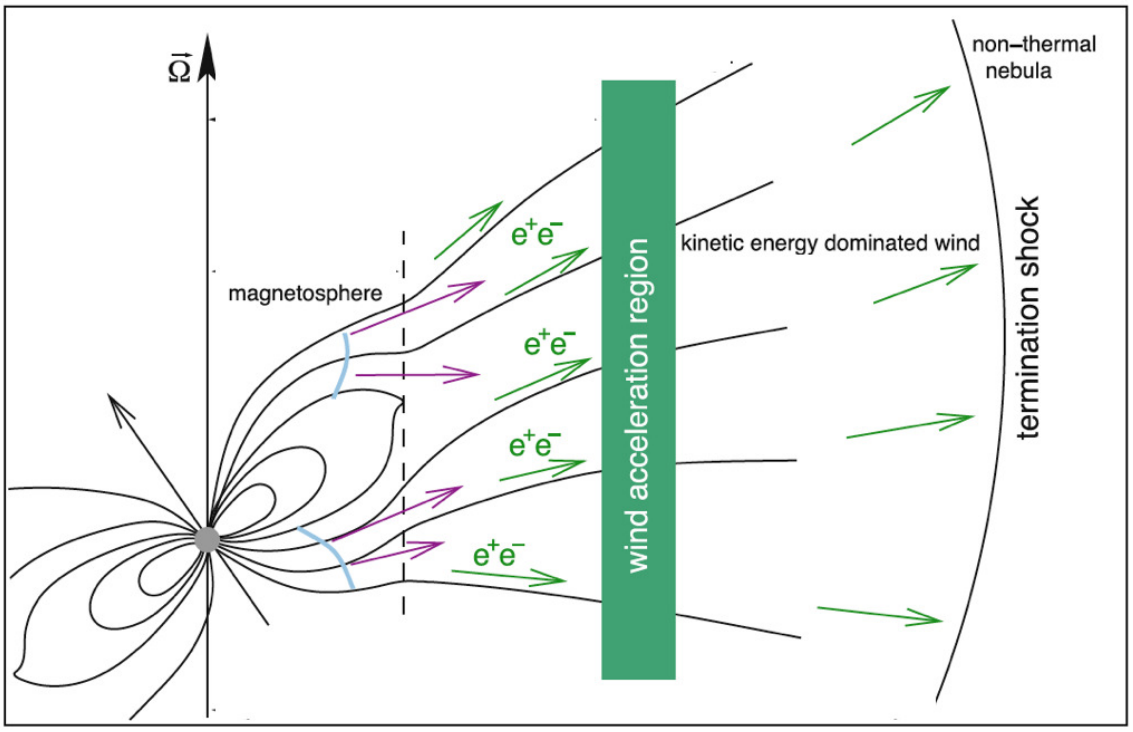

Figure 2.5: Sketch of $e^{\pm}$ pairs acceleration in wind acceleration zone of the pulsar environment and injection into PWN [2].

interstellar medium by a strong magnetohydrodynamic termination shock as illustrated in Fig. 2.5 [22]. The leptons at the termination shock region can inverse Compton (IC) scatter ambient photons from the cosmic microwave background radiation to TeV energies [22]. This non-thermal emission results in a luminous nebula, or PWN.

The three source types discussed here are present in my analysis region and contribute to TeV γ-ray emission I am studying which is discussed in more details in the Chapter 6.

2.3 Detection Techniques

Gamma ray energy ranges from above 100 keV to above 100 TeV covering over 7 decades of energy. A variety of observatories are required to measure different energy bands of gamma rays. LE gamma rays are blocked by the atmosphere from reaching the ground. Hence, to detect them, space-based instruments are needed. However, the detection area of a space-based detector such as Fermi-Large Area Telescope (LAT) is insufficient for the detection of VHE gamma rays. So, in order to have a large detector area to detect HE and VHE gamma rays, a ground-based technique is required.

2.3.1 Space-based Observatory: Fermi-LAT

Space-based γ-ray instruments directly observe the γ-ray photons and employ the principle of pair-creation by the incident γ-ray in the detector to detect the γ-ray signals. Fermi-LAT[3] is one such leading satellite-based γ-ray observatory. It is sensitive to γ-ray emission from 20 MeV to beyond 1 TeV range [10].

The Fermi-LAT γ-ray instruments include a tracker which tracks the e^-e^+ pair produced from the primary gamma ray, a calorimeter which measures the energy of the

[3] https://fermi.gsfc.nasa.gov/science/instruments/table1-1.html

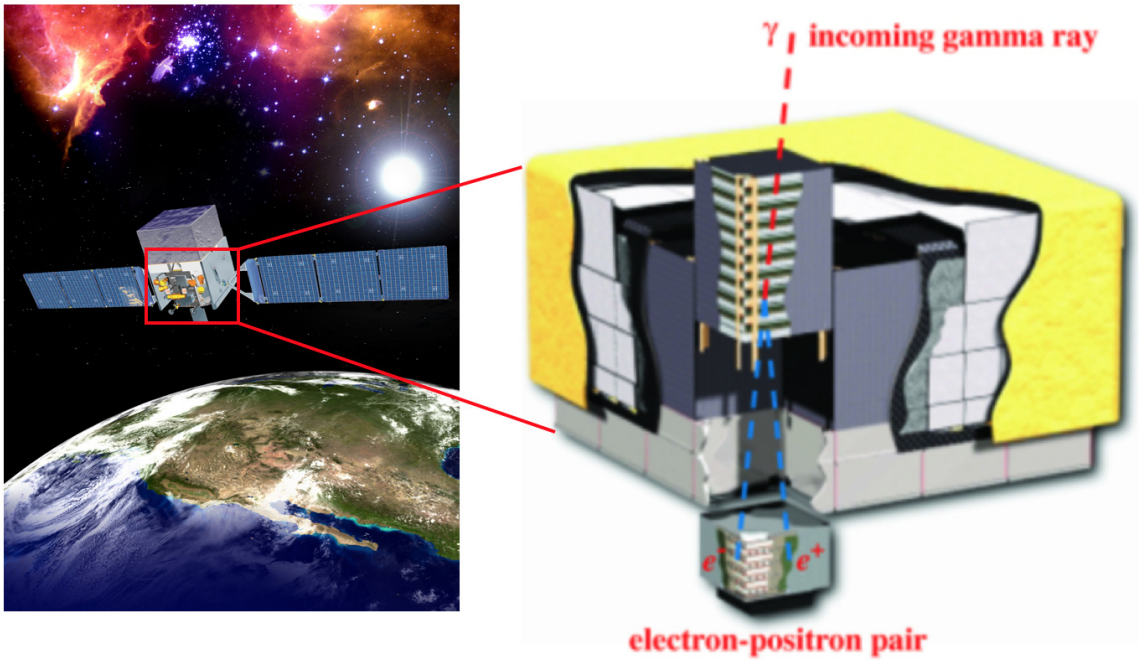

Figure 2.6: Fermi-LAT detector. Image credit: NASA.

e^+e^- pair and thus the energy of the primary gamma ray, and an anti-coincidence detector to identify the CR background. The trackers consist of 36 layers of silicon strip detectors with 16 layers of tungsten foil to allow pair creation. The total surface area of the Large Area Telescope (LAT) detector is 1.8m $\times$ 1.8m with about 80% of the surface area consisting tracker area. The trigger rate of the detector is $\sim$ 3KHz, which consist of predominately the CR proton background. After the reconstruction of these events and additional gamma-hadron cuts to reject the proton background, the total photon rate is a few Hz. The LAT has an effective collection area of $\sim 0.7m^2$ above $\sim$ 1GeV and has a field of view of 2.4 steradian at 1 GeV decreasing at lower and higher energy. The angular resolution at GeV is $> 3.5^\circ$ at 1 GeV and $< 0.15^\circ$ above 10 GeV. The live time of the LAT instrument is $\sim$ 75%. The LAT

detector was launched in June 2008 and from the regular monotoring of the sky since then to now has contributed to a significant improvement in our understanding of the MeV to GeV γ-ray sky. The fourth Fermi-LAT catalog consist of over 5000 galactic and extra-galactic γ-ray sources. For the galactic sources, it consists of 239 pulsars, 40 SNRs, 17 PWNe and one extended source (Cygnus Cocoon) associated with the massive stellar association.

2.3.2 Ground-based Observatories and Extensive Air Showers

Ground-based detectors detect secondary particles produced in γ-ray interactions with the atmosphere. Our atmosphere is opaque to γ-rays. When a γ-ray photon enters the atmosphere, it produces an electron-positron pair in its first interaction in the B-field of an atmospheric nucleus. The altitude of the first interaction is about a radiation length to the atmosphere. The electron-positron pair produces secondary photons by the Bremsstrahlung process. These secondary photons have enough energy to initiate more pair production and the pairs in turn produce more photons. These iterative processes create a cascade of secondary particles called an extensive air shower (EAS) as shown in Fig. 2.7.

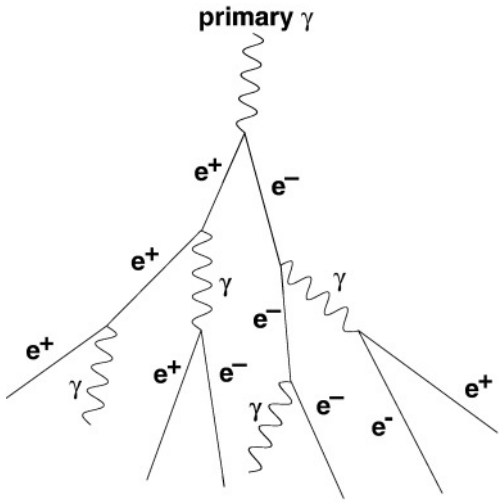

Figure 2.7: Schematic of γ-ray induced particle shower after the primary gamma ray enters the earth atmosphere.

As the penetration depth of the EAS increases, the number of secondary particles increases. The cascading process drops off after the average energy of the secondary electrons and positrons reaches $\sim$80 MeV, the critical energy at which the cross section for ionization losses becomes comparable to that for bremsstrahlung. This is called shower maximum. After this point, the number of secondary particles in the air shower drops rapidly as the dominating process i.e. the ionization losses does not produce additional air shower particles. Ground-based γ-ray instruments observe the EAS particles induced by the γ-ray showers and reconstruct the features of the primary gamma rays based on the observable parameters.

There are two principle ways of measuring EAS produced by the primary gamma ray (or CR):

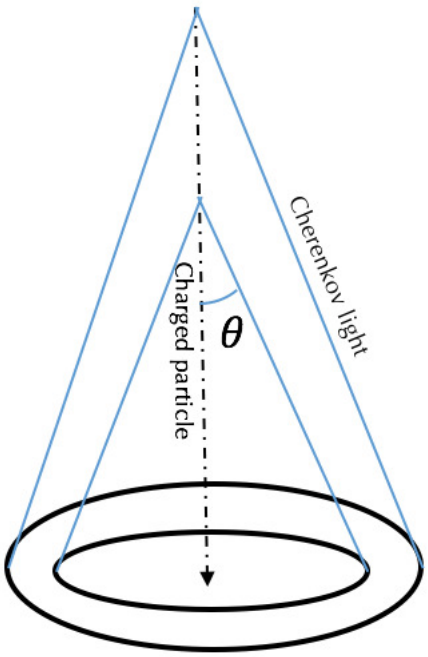

Figure 2.8: Sketch of a Cherenkov radiation cone emitted by the charged particle.

1. Imaging Atmospheric Cherenkov Telescopes (IACTs),

2. Air Shower Particle Detectors (ASPDs).

Before I describe the observatories of the two types that are relevant for the analysis that I am presenting here, I will provide a short description of a physics phenomenon that is used for EAS detection in both techniques: Cherenkov radiation.

2.3.3 Cherenkov Radiation

When a charged particle travels at a speed greater than the phase velocity of light in that medium, it emits Cherenkov radiation, in the shape of a narrow cone of

optical/UV light around the direction of the particle. This effect was first observed by Pavel Cherenkov in 1934. An expression for the half angle of the cone (Cherenkov angle) θ can be derived via

$$\cos\theta = \mathrm{c_n}/\mathrm{v_{particle}} \tag{2.13}$$

where $c_n = \frac{1}{n}$ is the phase velocity of the light and n is the refractive index.

Among the ground based detectors, an IACT detects the Cherenkov radiation of the EAS in the atmosphere whereas Water Cherenkov detectors which are of the ASPD type detect the Cherenkov light produced by EAS particles reaching water-filled detectors on the ground.

2.3.4 IACTs: VERITAS Observatory

An IACT observes the Cherenkov light produced by EAS particles with mirrors that reflect the light onto a fast camera in the focal plane of the mirrors. The amount of light detected provides a calorimetric measurement of the EAS energy. For, a 0.1 TeV shower, approximately, 100 m^2 of mirror area is required to trigger a telescope with 100 photo-electrons. Some of the observatories that operates on the IACT techiques are H.E.S.S., MAGIC and VERITAS.

Figure 2.9: VERITAS detector. Image credit: https://veritas.sao.arizona.edu/.

VERITAS (Very Energetic Radiation Imaging Telescope Array System) is a ground-based γ-ray instrument located in southern Arizona, USA. It consists of four IACTs with mirror size of 106 m^2. They are sensitive to VHE energy band of 50 GeV – 50 TeV with maximum sensitivity from 100 GeV –10 TeV range[4]. Each telescope has 350 individual mirrors, an aperture of 12 m and 499 pixel camera. The camera has a field of view of 3.5°. The γ-ray instruments have a limited duty cycle of less than 20% and angular resolution (68%$containmentradius$) of 0.08° at 1 TeV and 0.13° at 200 GeV. The observatory started its operation on 2007 and since then published a detailed study many γ-ray sources.

2.3.5 ASPDs: HAWC and ARGO-YBJ

ASPDs require the shower particles to reach the ground and hence are typically built at higher altitudes. They have a higher energy threshold and larger angular

[4] `https://veritas.sao.arizona.edu/`

resolution compared to IACTs. Because of this, ASPDs are typically less sensitive to point sources compared to IACTs. However, ASPDs have a high duty cycle and continuously monitor the entire sky above the detector. Due to their large field of view of the order of 2 steradians and high $> 95\%$ duty cycle, they are well suited to perform unbiased sky surveys. Also, since IACT data analyses usually calculate the residual background within a small field of view, compared to IACTs, ASPDs are better suited for extended source ($> 1^{\circ}$) analyses. Both kind of instruments have complementary capabilities and together they provide a more complete view of the γ-ray sky at TeV energies. The Chapter 3 will describe in detail one such ASPD array called the High-Altitude Water Cherenkov (HAWC) Observatory. Analysis of data collected with the HAWC Observatory is the main focus of this thesis.

There are other wide field of view observatories which use detection techniques other than the Water Cherenkov technique, for example the ARGO-YBJ [5] (Astrophysical Radiation with Ground-based Observatory at Yangbajing) experiment located at an altitude of 4300 m in Yangbajing, China. The experiment started taking data in November 2003 and stopped in January 2013 with a total observation time of 1670 days. The γ-ray instrument consisted of a single layer of resistive plate chambers equipped with the "pads" for triggering and covered an area of 6700m^2. The trigger rate was 3.5 KHz. The detector had an average duty cycle of $> 86\%$ and the angular resolution varied from 1.7° to 0.2°. The energy threshold for the detector was ~ 300

[5] http://argo.na.infn.it/

GeV and it was sensitive up to γ-ray energies of 100 TeV.

In my analysis, I have provided a detailed comparison of the data collected by the three γ-ray instruments: Fermi-LAT, ARGO-YBJ, and the HAWC γ-ray instruments.

Chapter 3

The HAWC Observatory

The High Altitude Water Cherenkov (HAWC)[1] observatory is a wide field ground based γ-ray observatory. As its name implies, it uses the water Cherenkov technique to detect gamma ray. It is located at geographical coordinates (18°59'41" N 97°18'30.6" W), Sierra Negra, Mexico at an altitude of 4100m above sea level. This altitude is suited for TeV γ-ray study, since shower maximum occurs for the TeV showers typically at an altitude of $\sim$ 5000 m. The observatory is sensitive to a few hundreds GeV to beyond 100 TeV γ-rays [34].

The HAWC γ-ray instrument is comprised of 300 water cherenkov detectors (WCD) array spread in 2200 m^2. Each tank is 7.3 m in diameter and 4.5 m in height and holds about 20,000 litre is ultra-purified water. Each WCD has four photomultipliers

[1] https://www.hawc-observatory.org

Figure 3.1: The HAWC Observatory (https://www.hawc-observatory.org/).

tubes (PMT) at the bottom which detect the Cherenkov light produced via charged particles from the air showers travelling in the WCD. Out of the four PMTs, three are 8-inch Hamamatsu R5912 which surround the central high-quantum efficiency 10-inch Hamamatsu R7081-MOD PMT as shown in Fig. 3.3.

3.1 Shower Reconstruction

Air shower events recorded by the detector are reconstructed to extract shower properties and after reconstruction process, event and background maps are generated [4].

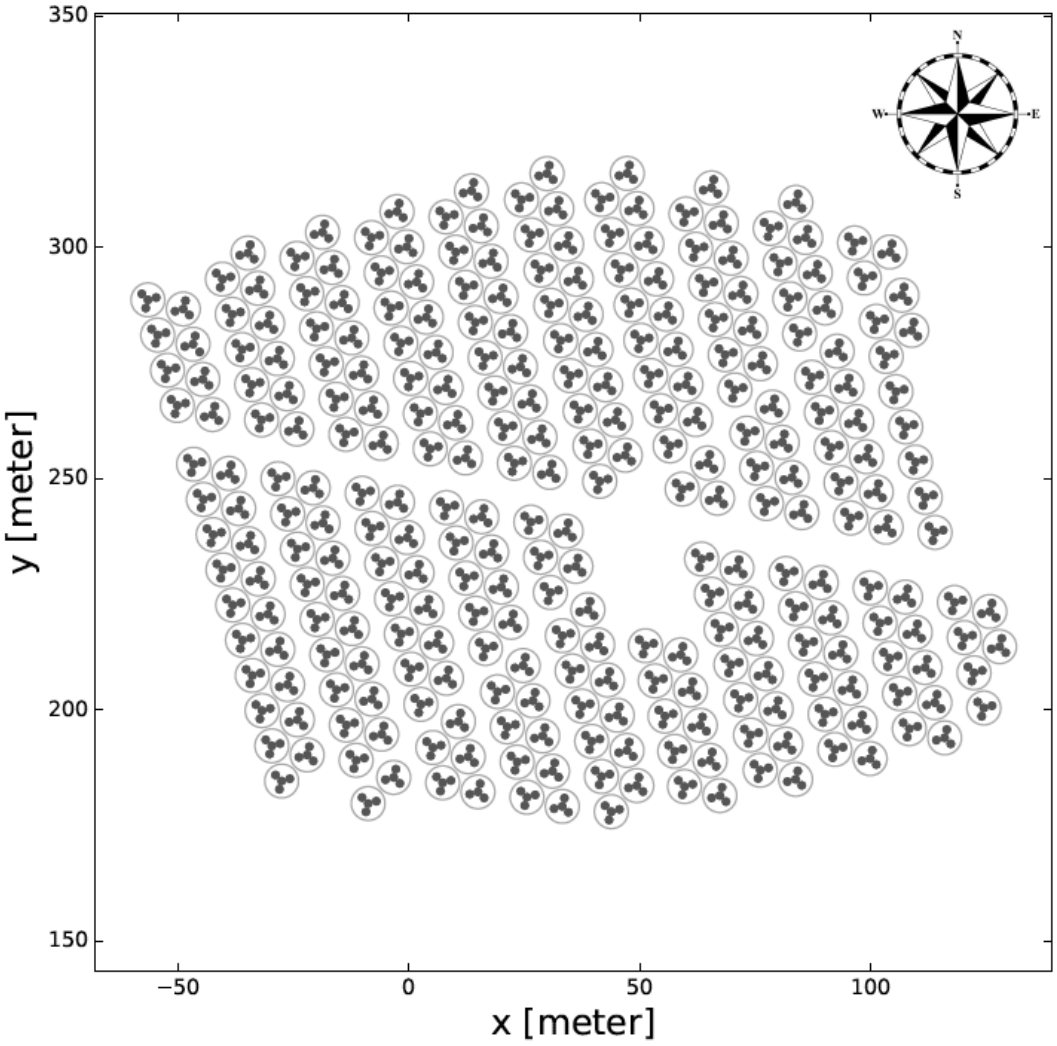

Figure 3.2: Layout of the HAWC WCDs from [3]. The central gap is the counting house.

The central gap in Fig. 3.2 is where the "counting house" is located. The counting house hosts the DAQ system. The DAQ system can be divided into two types: the main DAQ of HAWC and a scaler DAQ. The scaler DAQ counts the PMT signal rate within a 10 ms window. The data collected by the scaler DAQ is utilized in the study of transient events such as γ-ray bursts. The analysis presented here is based on the

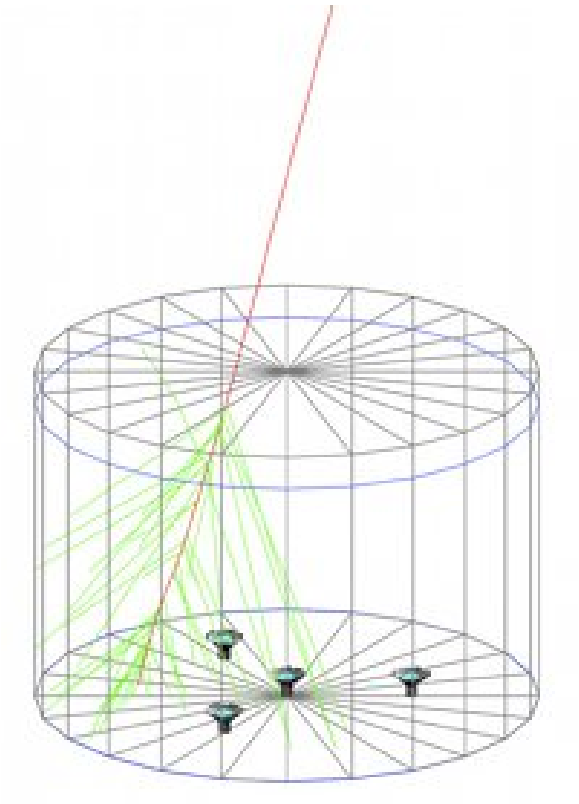

Figure 3.3: Schematic of one WCD with four PMTs at the bottom (https://www.hawc-observatory.org/).

data collected by the main DAQ.

The Cherenkov light produced by the secondary particles entering the WCD is captured on the PMT surface and converted to photoelectrons (PEs) on the photocathode of the PMTs via the photoelectric effect. This PE signal is then accelerated and amplified through the successive dynode chain of the PMT resulting in a charge gain of 10^7. The PMT voltages are selected based on the gain of the PMT and vary from 1.4-1.8 kV. Each PMT is coANNected to the DAQ in the counting house via RG59 coaxial cables which transfer the PMT signals to Front End Boards of the DAQ.

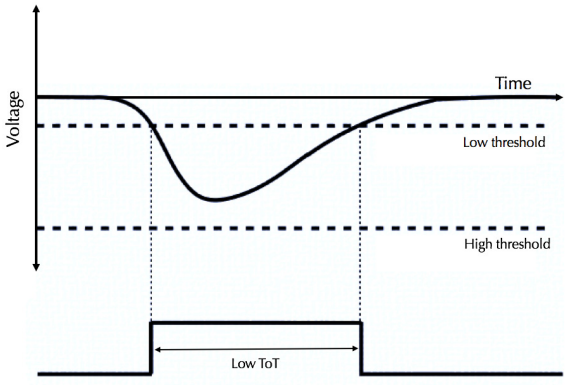

Figure 3.4: Schematic of a low charge signal with two edges.

These boards discriminate the PMT signals by applying two thresholds: a low threshold equivalent to about 0.25 PEs and a high threshold equivalent to about 5 PEs. The times at which the signal crosses each threshold are digitized and recorded by CAEN VX1190A time-to-digital-converters (TDCs). The time-stamp at which the signal crosses either of the two thresholds is called an "edge." These time stamps are utilised to calculate the charge of the signal (the number of PEs) via a "Time over Threshold" (ToT) estimation which subtracts the beginning edge from the ending edge of a signal. In general a signal with a low charge will have two edges and a signal with high charge will have 4 edges corresponding to the low and the high thresholds shown in Fig. 3.4 and Fig. 3.5 [2].

After the signals are time-stamped, the DAQ system uses an additional filter, a multiplicity trigger of 28 PMT hits within a 150 ns long trigger window. An "air shower event" that is recorded is the data within the window. The time and charge

[2]More complicated structures such as 6 and 8 edge events are flagged as "AMBIGUOUS" [35]

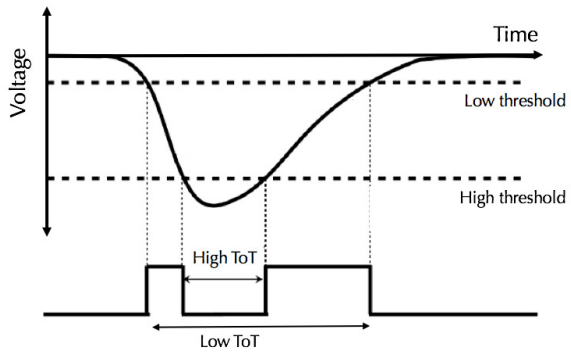

Figure 3.5: Schematic of a high charge signal with four edges

information of these events are then transferred to an on-site computing cluster for the reconstruction of the main properties of the primary gamma rays and cosmic rays. Each day $\sim$ 2TB of data is collected by the HAWC instruments.

The events are then reconstructed to extract the shower properties. The reconstruction algorithm converts the physical location and timing information from the PMT signals, also known as "hits", in an air shower to the location and arrival direction of the primary particle. Currently, the reconstruction process can be divided into two types: online reconstruction and offline reconstruction. Online reconstruction is performed on-site in real time as a rudimentary analysis for the time critical results of transient observations. The offline reconstruction is a more refined step and is performed on the computer clusters located at University of Maryland and National Autonomous University of Mexico. The results presented here are based on the data with the offline reconstruction.

3.2 Core Reconstruction

The shower core is the location of the maximum energy of the shower and it occurs at the location, where the main axis of the shower as shown in the figure, crosses the ground. The accurate location of the shower core is essential to determine the direction of primary gamma rays. We use the charges measured by the PMTs to identify the shower core position using an algorithm, called "Super Fast Core Fit" (SFCF). The SFCF lateral distribution function used for the shower core fit to estimate the core position is a modified form of the Nishimura-Kamata-Greisen (NKG) function: a combination of a Gaussian function and the tail of the NKG function. The initial values of the fit parameters in the χ^2 minimization is given by a Center of Mass estimate based on weighted average of PMT positions and measured charges in each PMT.

The charge in the ith PMT, $S(A, \vec{x_c}, \vec{x_i})$, is given by

$$S(A, \vec{x_c}, \vec{x_i}) = A\left(\frac{1}{2\pi\sigma^2} exp(-\frac{|\vec{x_i} - \vec{x_c}|^2}{2\sigma^2}) + \frac{N}{(0.5 + |\vec{x_i} - \vec{x_c}|/R_m)^3}\right) \tag{3.1}$$

where, A is the amplitude, $\vec{x_c}$ is position of the shower core, $\vec{x_i}$ is the position of the ith PMT. R_m is Moliere radius ($\sim$ 124 m). σ is the Gaussian width (= 10 m) and N is normalization of the tail. $\vec{x_c}$ and A are free parameters in the SFCF while the

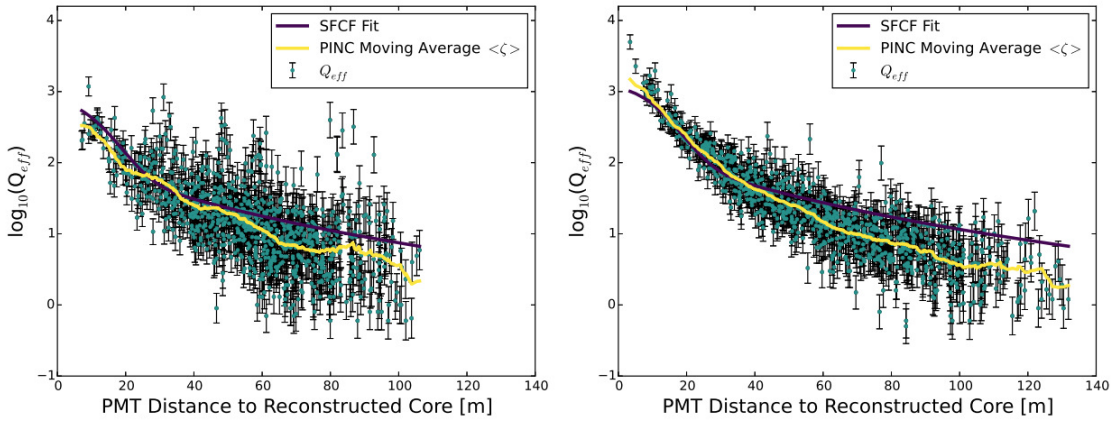

Figure 3.6: Effective charge vs the distance from the shower core for the hadron shower (left) and a likely gamma-like shower for the crab Nebula direction (right) from [4]. The black line is SFCF fit and the yellow line is the moving average used for calculating PINCness, discussed in the section 3.7.2.

rest of parameters are fixed at the optimized values obtained from the simulations of HAWC detector's response to air showers.

3.3 Direction Reconstruction

After estimating the shower core, the next step of the shower reconstruction process is estimating the direction of the incident particle using the timing information along with the charge measured by the PMTs. The shower particles spread laterally from the direction of the primary particle. Since, all the shower particles travel at $\approx$ the speed of light, the shower front, the lateral profile of the shower, has a conical shape (perpendicular to the direction of the incident particle) as shown in Fig. 3.7. We use

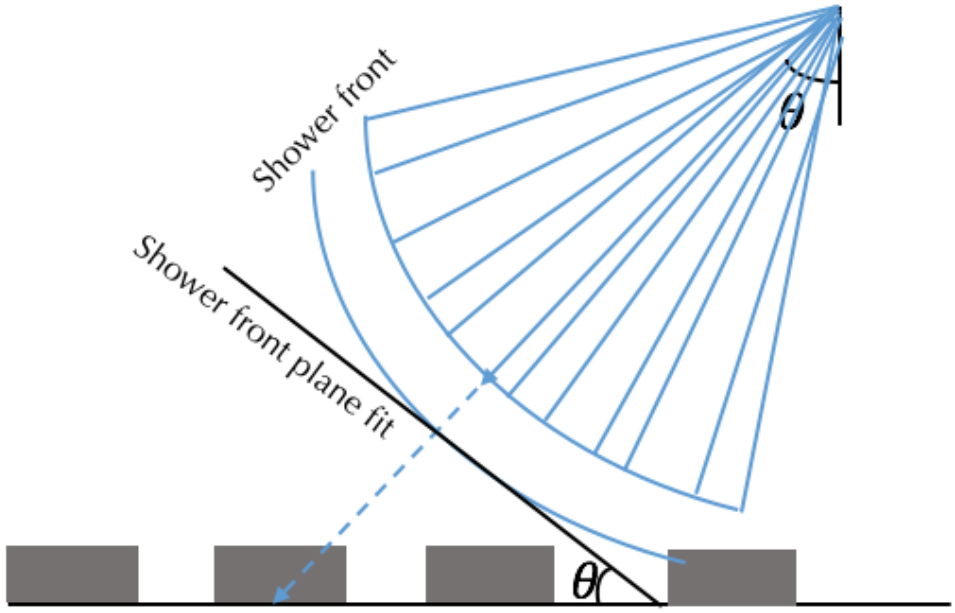

Figure 3.7: Schematic diagram of the shower front. The grey boxes are the WCDs. θ is the zenith angle of the shower front.

a plane fit for the shower front fit, i.e the arrival time of the shower plane is fitted to a flat plane (corrected for two timing effects) rather than a cone. The shower particles further from the shower core arrive late compared to if the shower front was a truly planar. Hence a curvature correction is applied to account for delay in the PMT hit times.

The second correction applied is called sampling correction to account for the decrease in the particle density further from the core. On average, a higher number of secondary particles near the core results in a higher number of hits and thus an earlier detection. This results in a sampling bias. The curvature and sampling correction is a few ns per 100 m distance from the core. After applying these two corrections, the

shower plane can be approximately described by a flat function. A weighted χ^2 fit to an arrival plane is performed to estimate the zenith and azimuthal direction (θ as shown in 3.7 and ϕ) of the shower fronts.

3.4 Calibration

A good reconstruction of the shower properties requires proper assignment of the timing and charge information provided by the PMT signal. Hence, PMTs are calibrated periodically and the calibration can be divided into two catagories: time calibration and charge calibration. The arrival time of the signal, the first time when it crosses the low threshold depends on the signal size. A larger signal will cross the threshold earlier and thus results in a relatively shorter "slewing" or response time of the PMT. For the calibration of the ToT values in units of PE and to provide corrections for the slew time an on-site laser calibration system is used. The laser sends out light through a combination of filter wheels to deliver a range of intensities to each PMT. To correct for the relative timing offset between the PMTs, a time residual method is applied [36].

Bin	f_{hit}%	$\psi_{68}{}^{\circ}$
1	0.07-0.11	1.03
2	0.11-0.16	0.69
3	0.16-0.25	0.50
4	0.25-0.37	0.39
5	0.37-0.51	0.30
6	0.51-0.66	0.28
7	0.66-0.78	0.22
8	0.78-0.88	0.20
9	0.88-1.00	0.17

Table 3.1
9 EAS size bins based on the fraction f_{hit} and angular resolution (68% containment) of each bin.

3.5 EAS Footprint Size in the HAWC Array

The data is divided into 9 bins of detected shower sizes as shown in the Table 3.1 based on the fraction f_{hit} operational or "live" PMTs triggered to the total number of available PMTs at the time.

The EAS size expressed in f_{hit} roughly depends on the energy of the initial particle, be it a gamma or cosmic ray. The most energetic events will trigger a maximum number of PMTs, f_{hit} bin 9 contains gamma rays of 10 TeV and above. A 10 TeV photon will trigger nearly all the PMTs in the array. This is one of the reasons why a more sophisticated algorithm is needed to determine the energies of the particle that initiate the EAS.

3.6 Energy Estimator

The f_{hit} parameter is a measure oof the original particle energy, but the correlation is poor. It only has limited energy information because it does not include additional parameters affecting the energy estimation, for example, zenith angle and the total light level in the WCDs. Additionally, as above mentioned f_{hit} has no dynamic range above 10 TeV. To improve the energy resolution, currently there are two energy estimation algorithms applied to the HAWC observatory data.

3.6.1 Ground Parameter (ρ_{40})

The ground parameter energy estimator is based on the techniques described in [37]. It utilises the charge density at 40 m from the EAS axis. This distance of 40 m is the optimal radius, at which the fluctuation in the signal from shower to shower is minimized. The optimal radius is determined by fitting the lateral distribution of the charge to a modified NKG function,

$$\begin{aligned} \log_{10}(\mathrm{NKG}) = \log(\mathrm{A}) + \mathrm{s}\cdot\left[\log_{10}\left(\frac{\mathrm{r}}{124.21}\right) + \log_{10}\left(1+\frac{\mathrm{r}}{124.21}\right)\right] \\ -3\log_{10}\left(\frac{\mathrm{r}}{124.21}\right) - 4.5\log_{10}\left(1+\frac{\mathrm{r}}{124.21}\right) \end{aligned} \tag{3.2}$$

where A is the amplitude, s is the parameter proportional to the shower age and r is the distance in m from the PMT sensor to the shower axis. The global optimal radius is estimated to be 40 m, representing the mean of optimal radii in each f_{hit}. During the reconstruction process, each event is fit to Eq. 3.2 to determine the charge density at the optimal radius of 40 m. The charge density varies with the zenith angle of the primary gamma rays. To relate γ-ray energy and charge density at 40 m, the following formula is used:

$$\log_{10}\mathrm{E} = \mathrm{m}(\theta)\log_{10}\rho_{40} + \mathrm{c}(\theta) \tag{3.3}$$

Here, E is the γ-ray energy, $m(\theta)$ and $\mathrm{c}(\theta)$ are the piecewise linear and quadratic functions of the zenith angle, which are calculated from the simulated γ-ray events and ρ_{40} is the charge density at 40 m. Finally, the EAS events are binned in γ-ray energy log space with a bin width of a quarter decade.

Rather than binning solely in energy bins, 2D binning scheme of f_{hit} and energy estimate provide a better description of the point spread function [38]. Also, using 2D binning improves the test statistics by up to a factor of three [38]. In 2D binning, 9 f_{hit} bins are further subdivided into 12 energy bins, resulting in a total of 108 bins. The analysis presented in this thesis was performed with the 2D ground parameter bins. Out of the 108 bins, the bins used in the analysis are selected based on the

Bin number	Energy Range (TeV)
a	0.316 - 0.562
b	0.562 - 1.00
c	1.00 - 1.78
d	1.78 - 3.16
e	3.16 - 5.62
f	5.62 - 10.0
g	10.0 - 17.8
h	17.8 - 31.6
i	31.6 - 56.2
j	56.2 - 100
k	100 - 177
l	177 - 316

Table 3.2
The ground parameters bins and their energy range

declination of the sources studied.

The study presented here is done with the ground parameter energy estimator. However, the results were cross-checked via another energy estimation, which is using an artificial neural network (ANN).

3.6.2 Artificial Neural Network

The neural network energy estimator utilises the Toolkit for Multivariate Analysis (TMVA) [39] ANN implementation. During the training process, it takes several parameters from the event reconstruction as input variables to describe the main characteristics of the shower [40]. Then the neural network energy estimation maps these input variable associated with an event to the output variable in terms of

energy E, $\log_{10}$E [40]. The performance of these two energy estimation methods are comparable with each other.

3.7 Gamma-Hadron Separation

The primary background for the γ-ray detection is hadronic CR showers. The trigger rate for the HAWC detectors is about $\sim 25KHz$, however 99% of the triggers are from CR hits. The shower footprints produced by gamma ray and CR have different characteristics. EAS originating from gamma rays have a significantly lower number of muons than those originating from the CRs. Muons hit the WCDs further from the shower core. Thus, γ-ray initiated EAS are smoother, more compact and more uniformly distributed around the shower core in comparison to the CRs initiated EAS. This can be see by comparing the PMT signal intensity map for a γ-ray shower (Fig. 3.9) with that of a CR shower (Fig. 3.8). Gamma-hadron quality cuts are applied to separate gamma events from hadron events. There are two gamma-hadron variables which distinguish if the air shower particles are produced by a gamma ray or a CR.

3.7.1 Compactness

Compactness is a measure of how compact the distribution of the charge is in the detector array. It is defined as

$$C = \frac{\mathrm{N_{hit}}}{\mathrm{CxPE_{40}}} \tag{3.4}$$

where N_{hit} is the number of PMTs triggered by the EAS event and used in the shower core reconstruction and $CxPE_{40}$ is the largest charge measured by a PMT outside a radius of 40 m from the center of the shower core. A higher value of $\mathrm{CxPE_{40}}$ indicates a larger probability that an EAS was initiated by a gamma ray.

3.7.2 Smoothness

The Parameter for Identifying Nuclear CRs (PINCness) is a measure of "smoothness" of the lateral distribution function of the charge. It is defined as:

$$P = \frac{1}{\mathrm{N}} \sum_{\mathrm{i=0}}^{\mathrm{N}} \frac{(\log(\mathrm{q_i}) - \langle \log(\mathrm{q_i}) \rangle)^2}{\sigma^2_{\log(\mathrm{q_i})}} \tag{3.5}$$

where N is total number of hits, $\mathrm{q_i}$ is the effective charge[3] in the ith PMT and σ is

[3]In order to normalize the difference between two different PMTs used in the WCDs, the charge

the charge uncertainty determined using the γ-ray events from the direction of the Crab Nebula. A smaller value of P denotes a smoother lateral distribution of the charge and hence indicates a larger probability of a shower event. Fig. 3.6 displays a moving average $< log(q_i) >$ for [hadron and gamma-like event scenarios]. Depending on the f_{hit} analysis bins, a P cut of 1.6-3.0 is applied.

After applying gamma/hadron cuts, in the lowest f_{hit} bin about 10% CR events are kept, whereas for the highest f_{hit} bin only about 0.1% CR events remain. Even after applying the smoothness cut, the lowest f_{hit} bin is still dominated by CR events.

3.8 [Point Spread Function (PSF)]

The point spread function (PSF) gives the uncertainty in arrival direction of the primary gamma ray. For the HAWC detector, it is approximated by a linear combination of two Gaussian functions.

$$\mathrm{PSF}\delta = \alpha \mathrm{G}_1(\delta) + (1-\alpha)\mathrm{G}_2(\delta) \tag{3.6}$$

where δ is the difference between the true arrival direction and the reconstructed

detected by a 10-inch PMT is scaled by 0.4554, called effective charge.

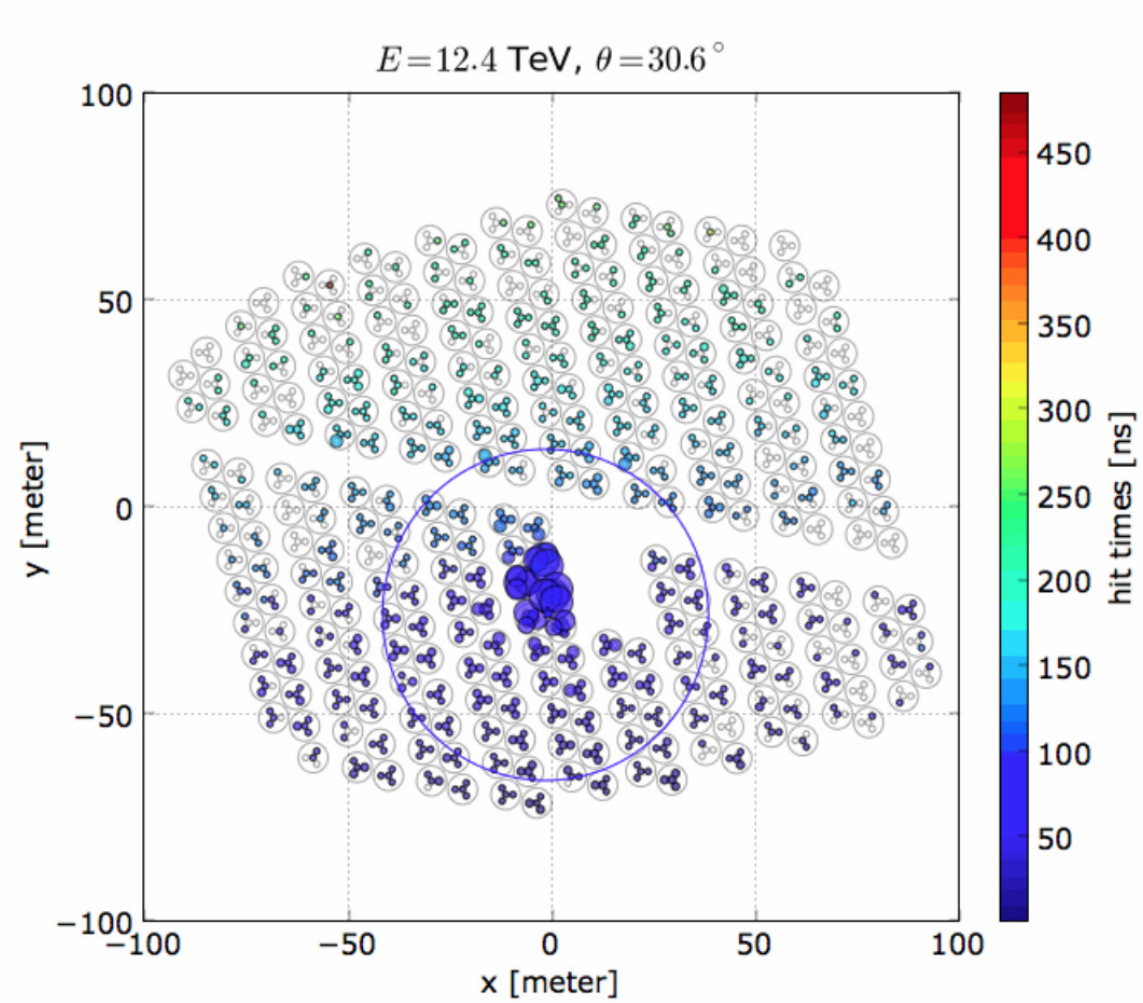

Figure 3.8: Shower footprint of a simulated γ-ray event. The color scale indicates the relative timing of the hits and the size of the marker denotes the number of PEs in each channel. Large markers represent larger signal and thus higher number of photons hitting the PMT. The blue circle denotes a 40-meter radius around the shower core. There are some isolated hits outside of the 40-m circle and the shower is uniformly distributed around the shower core indicating that this is a gamma event.

direction of the primary particle and α is the contribution from the two Gaussian functions G_1 and G_2. The PSF of the HAWC detector in higher f_{hit} bins is better in comparison to lower f_{hit} bins. In general, 68% containment value (ψ_{68}) is reported as listed in the Table 3.1 for the 9 f_{hit} bins.

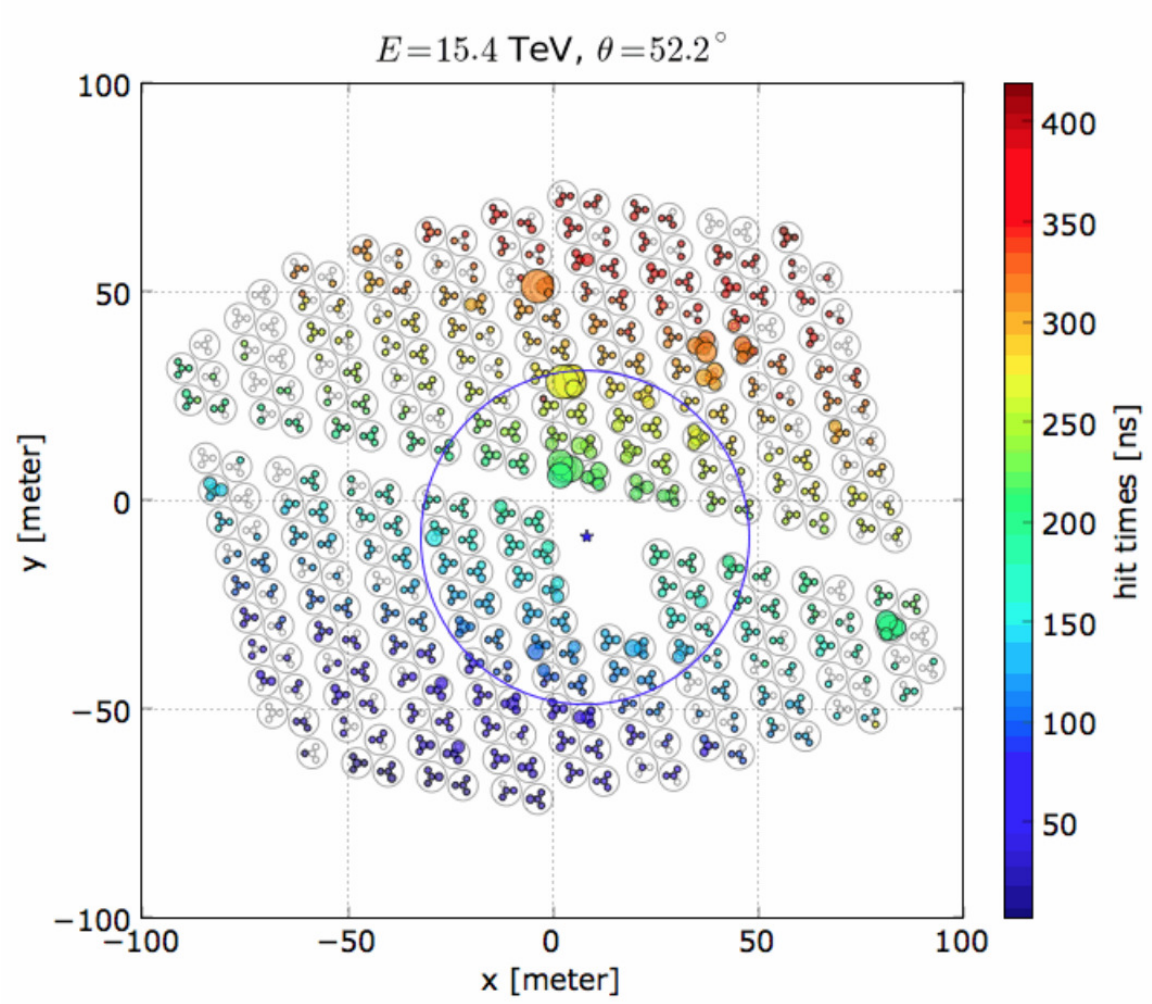

Figure 3.9: Shower footprint of a simulated hadron event. The color scale indicates the relative timing of the hits and the size of the marker denotes the number of PEs in each channel. The blue circle denotes a 40-meter radius around the shower core. The isolated hits outside of the circle are characteristic of hadron events. They indicate the presence of penetrating particles in the EAS, that deeply penetrate the water, such as muons.

3.9 Background Estimation

The hadronic CRs that pass gamma/hadron separation cuts during reconstruction form the main background in the analysis of γ-ray sources. For the statistically

significant lower energy bins, the background for each bin is estimated using a direct integration method outlined in [4]. For the low statistics bins (counts below 5×10^5) the background is estimated for each analysis bin using a "background randomization" method [34], which averages over the entire data set instead of integrating 2 hours data set as in the "direct integration" method. In the "background randomization" method, first for each bin, a two dimensional histogram distribution of the local coordinates, θ and ϕ is created, out of which a random pair is used to determine R.A and Dec. and added to the background map [34]. For each event, the distribution is sampled $\sim 10,000$ times. The background map is then normalized to the total number of events in the map and smoothed by 0.5°.

Chapter 4

The Cygnus-X Region

The Cygnus-X region located in the "heart" of the swan shown in Fig. 4.1, also known as the Cygnus constellation, is one of the brightest regions of our Galaxy at all wavelengths [41]. Multi-wavelength observation of the regions have confirmed the complex nature of the region with a wealth of various astrophysical objects. Observations in the optical band reveal 9 OB associations so far along with the one of most massive OB associations in our Galaxy, the OB2 association. The majority of the OB associations lie at the distance of ∼1.4-1.5 kpc [42]. The region is one of the richest and most active site of star formation as evident by 40 massive proto-stars [43], which will in the future evolve into OB stars. Along with a number of OB associations, observations in the radio band reveal more than 20 HII regions [44] and molecular clouds in connected groups [5]. It hosts one of the most massive molecular

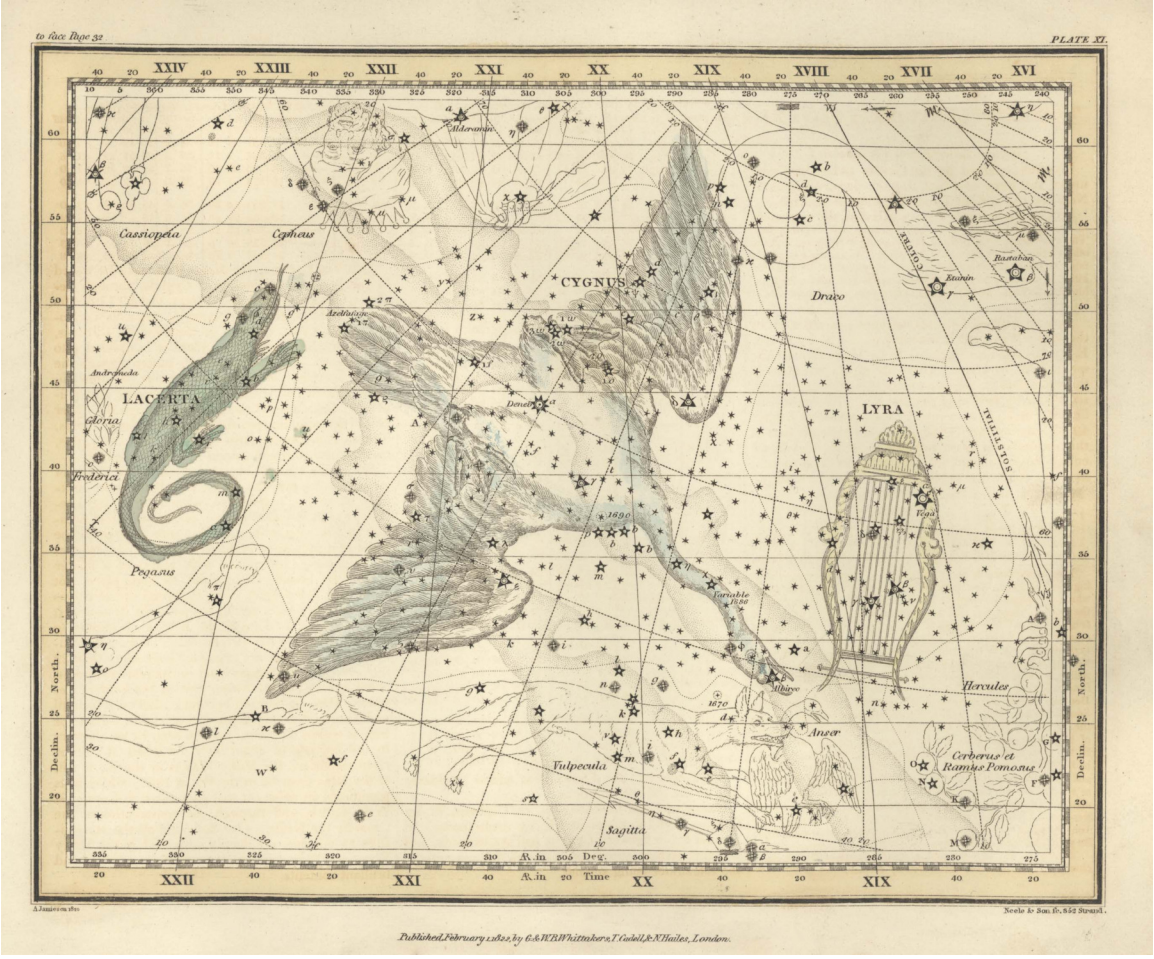

Figure 4.1: Cygnus constellation image as shown in stellar atlas of 1822 by Alexander Jamieson, downloaded from the United States Naval Observatory Library https://www.usno.navy.mil/USNO/library/historical/images-of-historical-objects-artwork-in-library/rare-books/images/jamieson?b_start:int=12.

complexes in our Galaxy with a mass of $3 \times 10^6 M_\odot$ [5]. This mass is much larger than the nearby molecular complexes with OB associations. For example, massive Orion A and Carina molecular clouds have masses of $\sim 10^5 M_\odot$ [45] and $\sim 2 \times 10^5 M_\odot$ [46] respectively. A large superbubble structure was first detected in the observations in the x-ray wavelength. γ-ray observation of the region confirms that the region hosts a number of γ-ray source types such as SNRs, pulsars, PWNs etc. GeV observation

by the Fermi-LAT study detected more than 60 sources in the region [10] and more than 5 sources in the region have been detected by the TeV observatories. Because of the active star formation in the region and a host of different astrophysical sources along with the massive OB associations, the region is a favourable site for the study of particle acceleration. Among the 9 OB associations, the OB2 association has been extensively studied and confirmed to be a site of particle acceleration.

4.1 The OB2 Association

The Cygnus OB2 near the center of Cygnus-X region contains 2600±400 OB stars, a number of binary stars, three Wolf-Rayet stars and 120 type O-stars. It consist of one of the brightest stars of our Galaxy, OB2-12, which is 2 million times more luminous than the sun. The total mass of the OB2 association has been cited as $(4-10)\times10^4$ $M_\odot$ [47] and most recently as $(2-4)\times10^4$ $M_\odot$ [48]. The mass is the largest OB association within 2 kpc and the wind mechanical luminosity of $10^{39}\mathrm{erg\,s^{-1}}$ has been maintained for at least 2 yrs [47]. The OB association is embedded in its molecular complex. Since it is hidden behind the massive dust cloud of the Cygnus Rift, it is not visible via the naked eye. The Orion nebula is 10 times less massive than the OB2 association [45] and yet visible via naked eye. The age of the massive stars in the association ranges from 1 - 7 Myr [49]. The center of the OB2 association is estimated to be (308.3, 41.3)°and is spherically symmetric with a diameter of $\sim 2°$

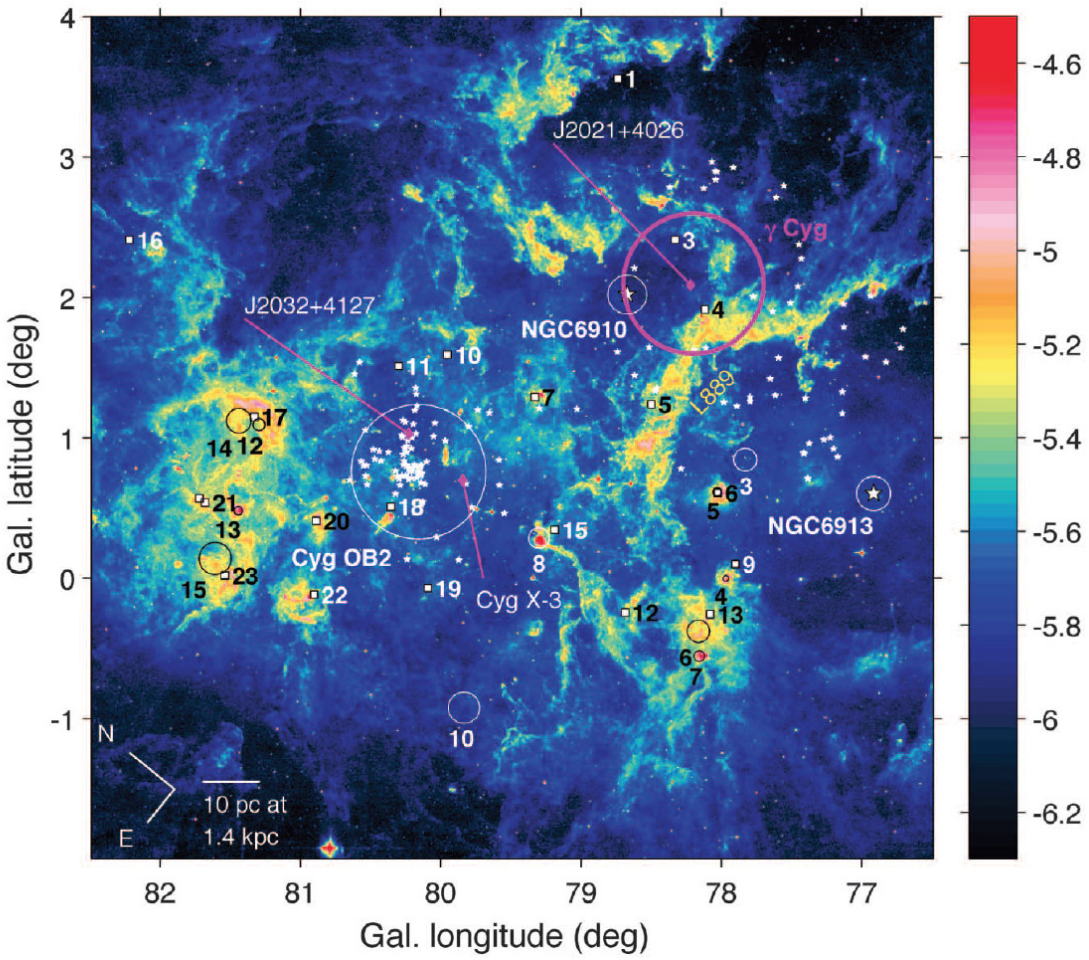

Figure 4.2: The Cygnus X region depicted in Galactic coordinates at a wavelength of 8µm by the Midcourse Space Experiment showing the photon dominated regions [5, 6]. Asterisks denote the most massive members of the Cyg OB2 cluster and the dashed circle its extent. The white circle characterize the extent of the OB2 association. Small squares with numbers beside them indicate the H II regions DR4 to DR23. The magenta circle characterize the extent of the SNR 78.2+2.1 (γ Cygni) and the cross its center.

[47].

4.2 Fermi-LAT Observation of the Cygnus Cocoon

The Fermi-LAT detected a 50 pc wide extended excess of γ-ray emission as shown in Fig. 4.3 centered at $(307.17, 41.17)^\circ$ in the Cygnus region after subtraction of the interstellar background and known sources in the region [6]. This excess emission is detected with 10.1σ significance above 1 GeV and is attributed to energetic particles inside the interstellar cavities created as a result of stellar activities [6]. The hard spectrum ($E^{-2.1}$) observed for this GeV emission indicates the source of the emission to be freshly-accelerated CRs [6]. The emission region is surrounded by infrared (IR) radiation, similar to a cocoon; a cavity surrounded by a bright IR bubble. Hence, it is called a Cocoon of freshly CRs and in short, Cygnus Cocoon. Co-located with the OB2 association in the region, there is another OB association called NGC 6910, however, the OB2 association is estimated to be 200 times more powerful than NGC 6910 [6]

The Cocoon lies in the bright Cygnus X region between the OB2 stellar association and the γ Cygni SNR. The Fermi-LAT study explored the possibility of the 7000 year old γ Cygni SNR as a possible source of the particles in the Cocoon. However, the morphology of this SNR and the lack of evidence of a shockwave from γ Cygni toward the direction of the Cocoon seem to rule out γ Cygni as a possible accelerator for the

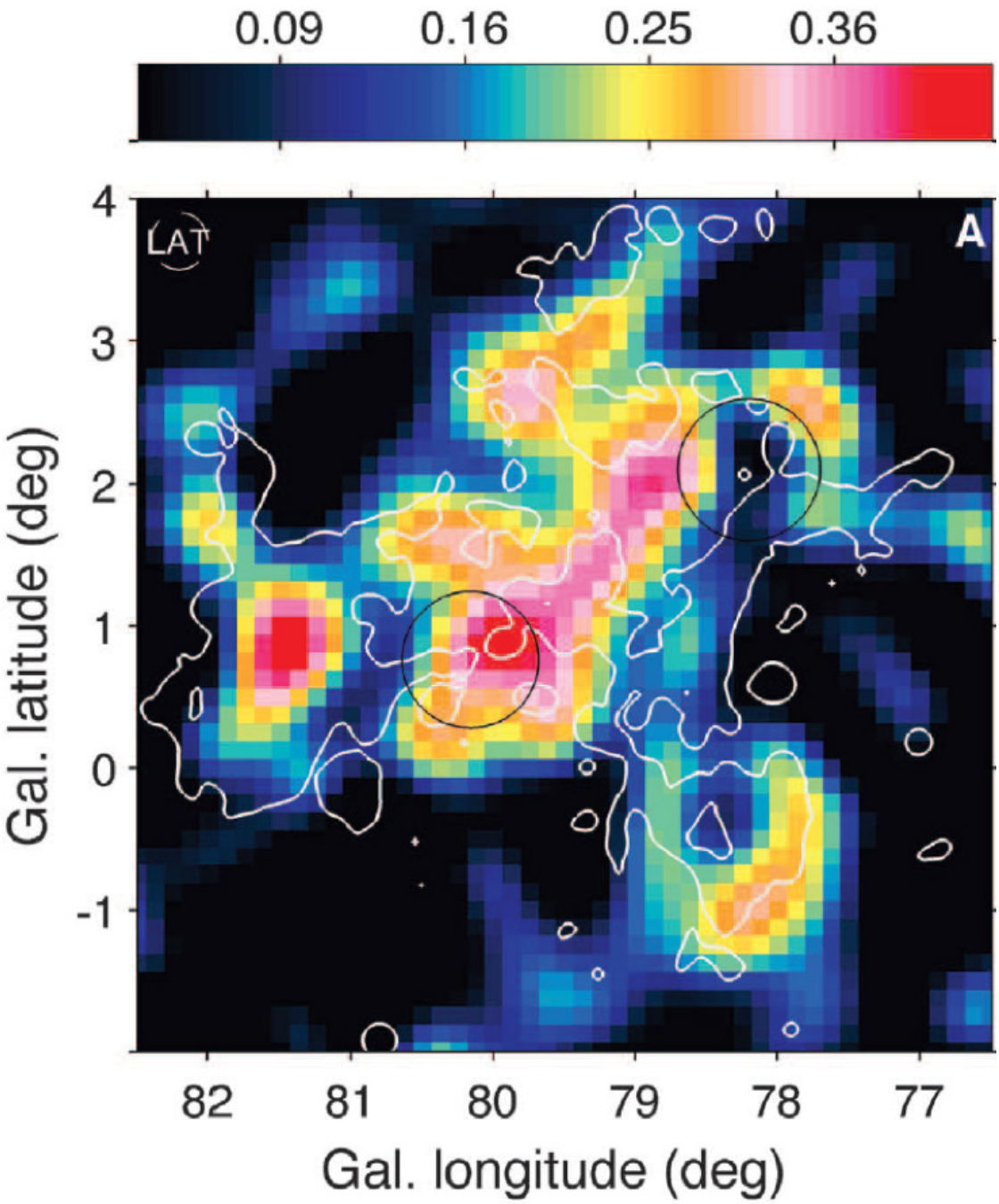

Figure 4.3: Residual photon count map from Fermi-LAT smoothed with a Gaussian kernel $\sigma = 0.25^\circ$ in the energy band of 10-100 GeV showing the extended region of Cocoon emission [6]. The white contours are the $10^{-5.6}\mathrm{Wm}^{-2}\mathrm{sr}^{-1}$ contours from Fig. 4.2. The small circle with LAT written inside in the upper left corner indicates the typical LAT angular resolution. The black circles denote the extent of OB2 association and γ Cygni SNR.

particles in the Cocoon [6]. The OB2 association is also a possible source for CRs in the Cocoon. Collective effects of stellar wind interactions of massive type O stars in the OB2 association could have accelerated the CRs that make up the Cocoon. The winds of the massive stars can sweep up the surrounding dust forming a ionized cavity with low density gas which is then illuminated by heating the dust. Thus the Cocoon is a rare opportunity to study production and acceleration mechanisms of CRs in our Galaxy within a SFR. Assuming that the accelerated particles in the Cocoon originated from the OB2 association, the Fermi-LAT collaboration calculated that the energetic protons can remain confined for over 100,000 years in the Cocoon. This result matches the time scale given by isotopic abundances [6]. Thus, the Fermi-LAT Cocoon is possibly an active CR superbubble [6]. Protons trapped in this superbubble interact with the surrounding molecular cloud nuclei and via pion decay processes, result in γ-ray emission detected by the Fermi-LAT instrument.

The Cocoon has no counterpart at lower energies. Observations in the (2–10) keV range by Suzaku observatory concluded that extended emission detected at the location after subtraction of known sources from X-ray images and Cosmic X-ray background is related to Galactic ridge X-ray emission rather than the Cocoon [13]. Observations at VHE energies by the other observatories have revealed a possible TeV counterpart [8, 50].

4.3 VERITAS Observations

As discussed in Section **??**, the VERITAS Observatory is less sensitive to extended sources and hence has not detected the large extended Cocoon. VERITAS Observation of the Cygnus Cocoon region detected a bright emission region as shown in Fig. 4.4 at the Cocoon and TeV 2032+4130 location, centered at $(307.99, 41.49)^\circ$. TeV 2032+4130 was first detected by the IACT detectors of the HEGRA observatory and was the first unidentified (with no counterparts at other wavelength) and first extended source in VHE [51]. The emission was bright and was described by a Gaussian radius much smaller (by more than a factor of 10) region than compared to the Cygnus Cocoon. Other IACTs such as the Whipple, MAGIC and VERITAS observatories have also reported a small extended emission co-located with TeV 2032+4130. In VERITAS data, the co-located emission of VER J2031+415 (centered at $(307.89, 41.58)^\circ$ was detected above 10σ and is concluded to be a possible PWN powered by the binary pulsar PSR J2032 + 4127 whose properties are shown in Table 4.1 [52]. GeV pulsar J2031+4127 has been identified as a binary pulsar with with a $15 M_\odot$ Be star [53] which reached its periastron in November 2017.

Studies by the MAGIC and VERITAS observatories during the periastron period detected co-related X-ray and γ-ray emission from the direction of the pulsar, providing

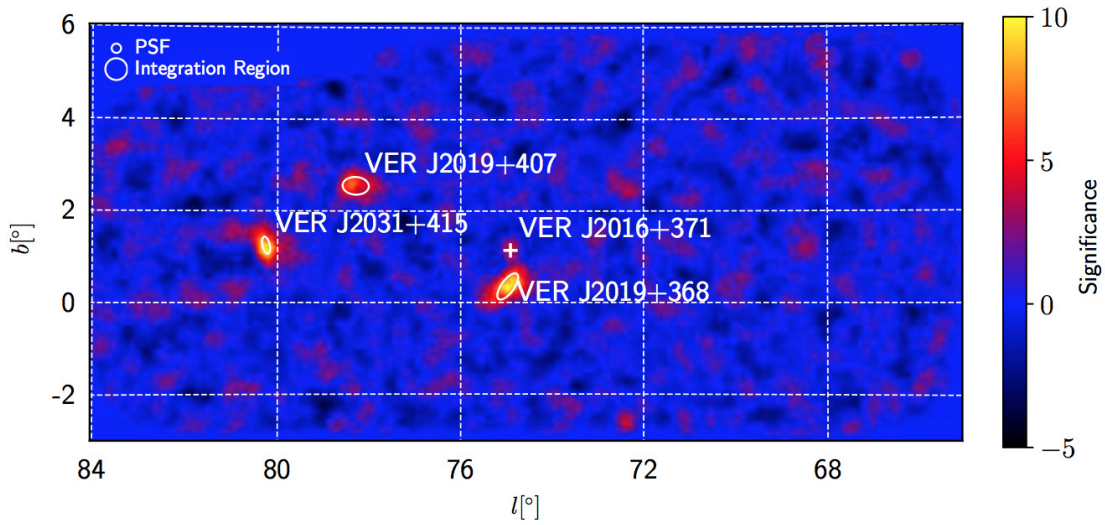

Figure 4.4: Significance map of the Cygnus region as observed by the VERITAS observatory above 400 GeV with extended 0.23° integration radius [7]. The white contour indicate 1σ ellipses for the source extent assuming an asymmetric Gaussian function for the three extended VERITAS sources (VER J2019+407, VER J2031+415, VER J2019+368). The white cross symbol mark the position for VER J2016+371.

Table 4.1
PSR J2032+4157

Name	**Age** [Kyr]	**Distance** [pc]	**Ė** [erg/s]	**PWN**
PSR J2032+4157	181	1700	1.7e35	TeV J2032+41

conclusive evidence for the binary nature of the pulsar system [54]. It is best described by an asymmetric Gaussian morphology with width of -0.19°±0.02° by 0.08°±0.01° and a power law spectrum with a normalization of $9.5 \pm 1.6_{\text{stat}}$ TeV^{-1}cm^{2}s and index of $-2.10 \pm 0.14_{\text{stat}}$ [7, 52]. In the 2014 study, VERITAS predicted that because of the hard index obtained for this source up to 10 TeV energy, a cutoff around tens of TeV must be observed due to the Klein-Nishina effect to support the PWN hypothesis [52]. A cutoff has not been detected in the new 2018 study up to 30 TeV, however, it identified a potential counterpart as FGL J2032.2+4128e [7].

Currently, the observatory is working towards analysis techniques to increase the sensitivity for extended sources which will allow the observations of large extended source such as the Cygnus Cocoon. With the improved sensitivity and future studies to determine the relation between the two extended objects (VER J2031+415 and the Cygnus Cocoon) detected at the region will provide definite conclusions regarding the nature of the VER J2031+415.

4.4 ARGO-YBJ Observations

The ARGO-YBJ experiment detected a region of γ-ray emission as shown in Fig. 4.5 centered at $(307.8, 42.5)^\circ$ co-located with the Cygnus Cocoon. The emission was described by a Gaussian width of $1.8^\circ \pm 0.5^\circ$. The spectral energy distribution of the emission in the energy range of 0.2-10 TeV is in agreement with the simple extrapolation of the Cygnus Cocoon spectrum to TeV energies. Because of its extended morphology and possible spectral connection, the ARGO J2031+4157 was suggested as a possible TeV counterpart of the Cocoon. [8].

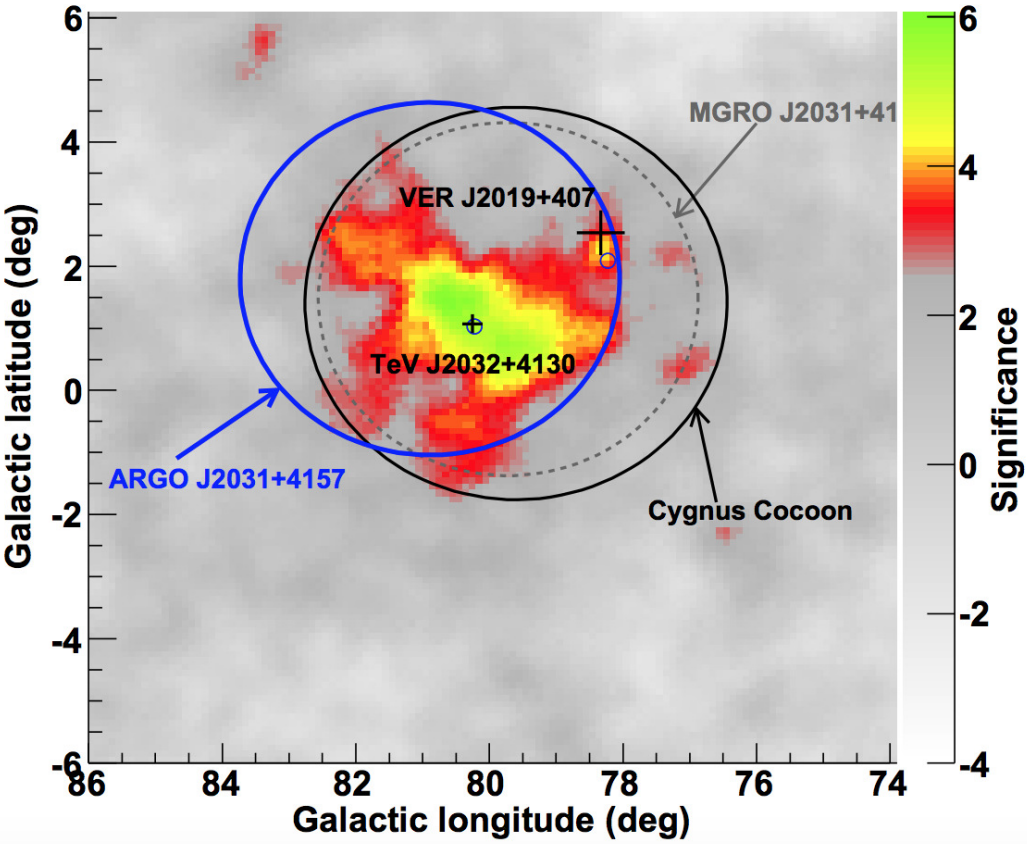

Figure 4.5: Significance map of the ARGO J2031+4157 region by the ARGO-YBJ experiment [8]. The large blue, dotted grey and black circles mark the extent (68% containment radius) and positions of ARGO J2031+4157, MGRO J2031+41 and the Cygnus Cocoon respectively. Black crosses indicate the position and extension of TeV 2032+4130 and VER J2019+407. The small black circles denote the positions of PSR 2021+4026 and PSR 2032+4127.

4.5 HAWC Observation of the Cygnus Region

In its 17 months data set, HAWC detected γ-ray emission above 100 GeV from the five sources within the Cygnus region ($70^\circ < l < 85^\circ, -4^\circ < b < 4^\circ$) using a "2 sigma dip" method [3]. Three HAWC sources lie in the vicinity of the Cygnus Cocoon

Table 4.2
HAWC Sources in the Cocoon Region

Name	**RA** [deg]	**Dec** [deg]	**Nearest TeVCat Source**
2HWC J2020+403	305.16	40.37	VER J2019+407
2HWC J2024+417	306.04	41.76	MGRO J2031+41
2HWC J2031+415	307.93	41.51	TeV J2032+4130

region ($78^\circ < l < 81^\circ, 1^\circ < b < 3^\circ$) as listed in Table 4.2 [3]. The fourth HAWC source 2HWC J2019+367 lies about $\sim 3^\circ$ from the center of the Cygnus Cocoon position.

Fig. 4.6 shows the significance map of the Cygnus region with the location of the five sources detected by the second HAWC catalog source. In the color scale, 5σ (corresponds to about 1 in a 3.5 million probability that the detected event is not a source) is the threshold of detection of a γ-ray source. Contrary to the 17 months map in the second HAWC catalog using f_{hit} bins, the map in Fig. 4.6 is made with 1038 days of data and made with the ρ_{40} energy estimator.

Among the three sources in the vicinity of the Cygnus Cocoon, the HAWC observatory detects the strongest emission at the **2HWC J2031+415** location which lies 0.08° from the PWN TeV J2032 + 4130. The flux measured for 2HWC J2031+415 is closer to the fluxes reported by the ARGO experiment, which is larger in angular size and higher than the fluxes measured by VERITAS and other IACTs [4, 8, 50]. The discrepancies seen by the wide-field TeV observatory suggest additional large-scale emission. To understand the relation between the Cocoon and TeV 2032+4130 source overlapping the region, multi-source component fits are performed, which will

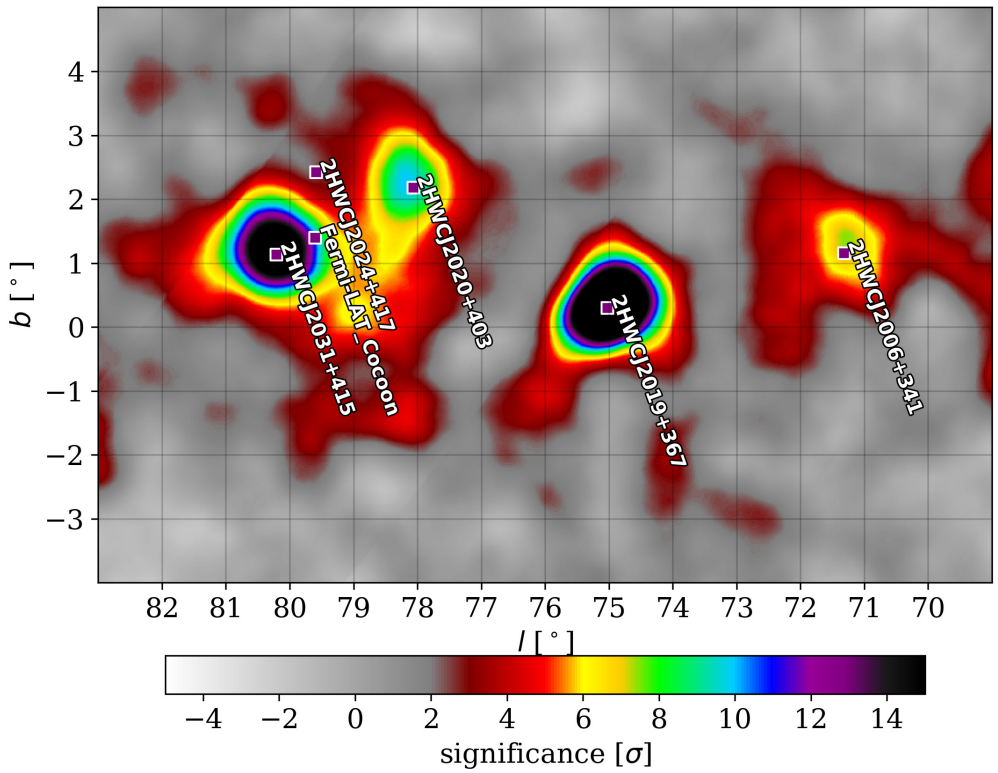

Figure 4.6: Map of significance over background with 1038 days of HAWC data. The map has been smoothed with a Gaussian radius of 0.5°. The location of the five Cygnus Region sources along with the Fermi-LAT Cocoon location is shown.

be presented in the Chapter **??**.

Chapter 5

Statistical Models

5.1 Maximum Likelihood Method

For the analysis of the HAWC data set, a maximum likelihood framework is used as outlined in [16]. A likelihood function is the probability for a collection of data points $x_1, x_2, \ldots\ldots\ldots x_n$, given the probability density $P(x_1, x_2, \ldots., x_n; \vec{\theta})$ where $\vec{\theta}$ is an unknown parameter vector:

$$L(\vec{\theta}|x_1, x_2, \ldots., x_n) = P(x_1, x_2, \ldots., x_n; \vec{\theta}) = \prod_{i=1}^{n} P(x_i; \vec{\theta}) \tag{5.1}$$

The maximum likelihood method then finds the parameter values for the model that

maximizes the probability or likelihood of explaining the data. In our case, the data points are the event counts. After the reconstruction steps discussed in the Chapter 3, event and background maps are generated. For the analysis of the γ-ray sources, the next step after obtaining the maps is to calculate the statistical significance of the excess and the detailed study of spectral and morphological study of the excess.

5.1.1 Building a source model

The first step in the analysis is to build a source model for the observed γ-ray emission in a region of interest (ROI). The model includes a spatial and a spectral description of the source. On the basis on the source morphology, the source can be characterized as a point source or an extended source. A point source is a γ-ray emission excess which can not be resolved further by the angular resolution of the HAWC γ-ray instruments and hence does not have a detailed spatial morphology. An extended source is a γ-ray emission excess which has larger angular size than the angular resolution of the HAWC detector and hence can be described by various morphological shapes such as a disk, a Gaussian or an asymmetric Gaussian shape.

For a point source model, the parameters are position and spectrum of the source. In case of an extended source model, apart from these two parameters, there are one or more additional parameters depending on the morphology of the model - for example,

Gaussian widths, or parameters of a physics model that predicts a particular source extent in HAWC data etc.

The spectral energy distribution of the source can be described by different functions which contain the information about the γ-ray flux. One assumption is a power law, which is described by

$$\frac{dN}{dE} = N_0 \frac{E}{E_0}^{-\Gamma} \tag{5.2}$$

where N_0 is the differential flux normalization, Γ is the spectral index, and E_0 is the pivot energy, at which co-relation between Γ and N_0 is minimized and approaching zero.

A second commonly used assumption is a power law with an exponential cutoff which is described by

$$\frac{dN}{dE} = N_0 \frac{E}{E_0}^{-\Gamma} \cdot \exp\left(\frac{E}{E_c}\right) \tag{5.3}$$

where N_0 is the differential flux normalization, Γ is the spectral index, E_0 is the pivot energy and E_c is the exponential cutoff energy.

In the ROI, there may be multiple sources. The next step in the analysis is to decide which parameters should be treated as variable ("free") or fixed by the fit, e.g. the location of the source (RA, DEC), spectral and other spacial parameters. Free parameters are being fit to maximize the likelihood of the function describing the source.

5.1.2 Fitting the Source Model

Given the model, the expected γ-ray events and background events are calculated by forward folding using detector response functions obtained from Monte Carlo simulations. The observed number of events in each pixel of each bin is characterized by the Poisson distribution.

$$p_i = \frac{\theta_i^{n_i} e^{-\theta_i}}{n_i!} \tag{5.4}$$

where n_i is the number of observed events in pixel i and θ_i is the number of expected events in pixel i. Then, L is the product of the probabilities of observing the detected number of events in each bin,

$$L = \prod_{i=1} p_i \tag{5.5}$$

Taking the logarithm, we get,

$$logL = \sum n_i \cdot \log(\theta_i) - \sum \theta_i - \sum log(n_i!) \tag{5.6}$$

where the last term can be ignored as it does not depend on the model. The log likelihood is maximized (or -log(Likelihood) is minimized) in the source model with respect to θ.

5.2 Bayesian Statistics

For the studies presented here, the results obtained from the maximum likelihood method were cross-checked in the preliminary analysis with a Bayesian approach to test the strength of a model. Suppose we have a set of probability distribution parameters, $\vec{\theta}$, to describe the data set , a collection of data points $x_1, x_2, \ldots\ldots\ldots x_n$. Then, given a prior function $P(\vec{\theta})$, Bayes' Rule gives the posterior distribution function $P(\vec{\theta}|x_1, x_2, \ldots\ldots\ldots x_n)$. Bayes' Rule is given by,

$$P(\vec{\theta}|x_1, x_2, \ldots\ldots\ldots x_n) = \frac{P(x_1, x_2, \ldots\ldots\ldots x_n|\vec{\theta}) \cdot P(\vec{\theta})}{P(x_1, x_2, \ldots\ldots\ldots x_n)} \tag{5.7}$$

where, $P(x_1, x_2, \ldots\ldots\ldots x_n|\vec{\theta})$ is likelihood function and $P(x_1, x_2, \ldots\ldots\ldots x_n)$ is evidence given by $P(x_1, x_2, \ldots\ldots\ldots x_n) = \int_\theta P((x_1, x_2, \ldots\ldots\ldots x_n)|\theta \cdot P(\theta) d\theta$.

In case of Bayesian inference, likelihood function is multiplied by prior distribution. Bayesian estimate treats θ as a random variable and calculates the posterior distribution. We get the probability density function for the θ values. In case of the maximum likelihood method in 5.1, the θ values are estimated as the point values. The posterior distribution of θ variable obtained in Bayesian inference fit can be utilised in different ways to estimate the parameters θ; for example: taking the mean of the distribution, the median of the distribution, the mode of the distribution etc. The mode of the

distribution i.e the parameter estimate which maximizes the posterior function is also called the maximum a posteriori estimate (MAP). For a uniform prior, the mode is same as the parameter estimate given by maximum likelihood method.

5.3 Model Comparison

Once we have the results of fitting different models, the next step is to decide on the model that best describe the data in the given ROI. Test statistics (TS) is defined by a likelihood ratio test [16]. Therefore,

$$TS = 2ln(L_{alt} - L_{null}) \tag{5.8}$$

where, L_{alt} is the maximum likelihood of model used for γ-ray source emission (alternate hypothesis) and L_{null} is the likelihood of the background-only model (null hypothesis).

According to Wilk's theorem for the nested models, the TS follows a χ^2 distribution with the Degree of Freedom (DoF) equal to the number of the free parameters [55]. For one free parameter, the significance can be written as

$$\sigma = \sqrt{TS} \tag{5.9}$$

5.3.1 ΔTS comparison

Eq. 5.2 and Eq. 5.3 represent nested models. Suppose we are trying to figure out which is a better spectral description of the source. We have one model described by a power law spectrum with N_0 and Γ as free parameters and another model with N_0, Γ and E_c as free parameters. The ΔTS between the two best fit models is calculated and since, the difference of free parameters between the two models is one, $\sigma = \sqrt{\Delta TS}$. σ is the significance with which one model is preferred over the other. If there is no significant preference of one model over the other ($\sigma \leq 3$), the simpler model is chosen ("Occam's Razor" principle).

5.3.2 BIC

What if the models are not nested? For example, a spectral function can be described a broken power law,

$$\frac{dN}{dt} = \begin{cases} N_0 \left(\frac{E}{E_0}\right)^{-\Gamma_1} : E < E_{break} \\ \\ N_0 \left(\frac{E}{E_0}\right)^{\Gamma_2-\Gamma_1} \left(\frac{E}{E_0}\right)^{-\Gamma_2} : E > E_{break} \end{cases} \tag{5.10}$$

ΔBIC	**Evidence against higher BIC model**
0 to 2	Not worth more than a bare mention
2 to 6	Positive
6 to 10	Strong
>10	Very Strong

Table 5.1
Δ BIC interpretation [17].

where, $-\Gamma_1$ is index before the break, $-\Gamma_2$ is index after the break and E_{break} is the break energy. Eq. 5.10 and 5.3 are non-nested models. To decide which spectral function is a better description of the source emission, the Bayesian information criterion (BIC) [56] is used. It is defined as

$$BIC = -log(L) - klog(n) \tag{5.11}$$

where k is the number of free parameters, n is the sample size (number of events) and $klog(n)$ is a "penalty" term depending on the number of free parameters. While comparing two models, the model with lower BIC is favored. The value of the parameter ΔBIC between two models can be translated into statements of confidence listed in Table 5.1 from [17].

Chapter 6

HAWC Observations of the Cygnus Cocoon Region

6.1 Sources in the Region of the interest

This chapter will focus on the spectral and the morphological studies of the Cocoon region and physics interpretation of the results. The studies were performed using over 1038 days of data in GP energy estimator bins. The bins used are: 1c, 1d, 1e, 1f, 2c, 2d, 2e, 2f, 3c, 3d, 3e, 3f, 4c, 4d, 4e, 4f, 4g, 5e, 5f, 5g, 5h, 6e, 6f, 6g, 6h, 7f, 7g, 7h, 7i, 8g, 8h, 8i, 8j, 9g, 9h, 9i, 9j, 9k and 9l. These bins correspond to the reconstructed energy above 1 TeV and have been selected for the declination of the sources in the

ROI.

In this study, the Cocoon region refers to a 6° radius circle centered at the Fermi-LAT Cocoon location (307.17, 41.17)°. This region includes the bright HAWC source 2HWC J2019+367. This source is removed from the ROI with mask in the shape of a disk of radiua 2° mask at (305.7, 36.8)°. The ROI is represented by the green contour in Fig. 6.1.

2HWC J2031+415 is one of the bright Cygnus region sources listed in the second HAWC catalog [3]. It was detected with significance of 14.69 σ using a point source analysis at the location (RA =307.93°, Dec=41.51°). The source is co-located with VER J2031+415, which is likely associated with a PWN. Both, VER J2031+415 and 2HWC J2031+415 are situated well within an extended region of γ-ray emission detected at GeV energies by Fermi-LAT as shown in Fig. 6.1. A second HAWC source 2HWC J2020+403, possibly associated with γ Cygni, lies 2.36° away from the center of the 2HWC J2031+415 location. In addition to these two HAWC sources, another HAWC source in the cocoon region is listed in the catalog paper as 2HWC J2024+417 using a method that identifies separate sources by requiring that the significance falls by at least 2 sigma to a local minimum between two local maxima [3].

Source	**Location (RA, Dec)°**	**Detected by**	**Energy Range**
VER J2031+415	(307.89, 41.51)	VERITAS	(0.7 - 16) TeV
Fermi-LAT Cocoon	(307.17, 41.17)	Fermi-LAT	(1-100) GeV

Table 6.1
Overlapping sources at the 2HWC J2031+415 region

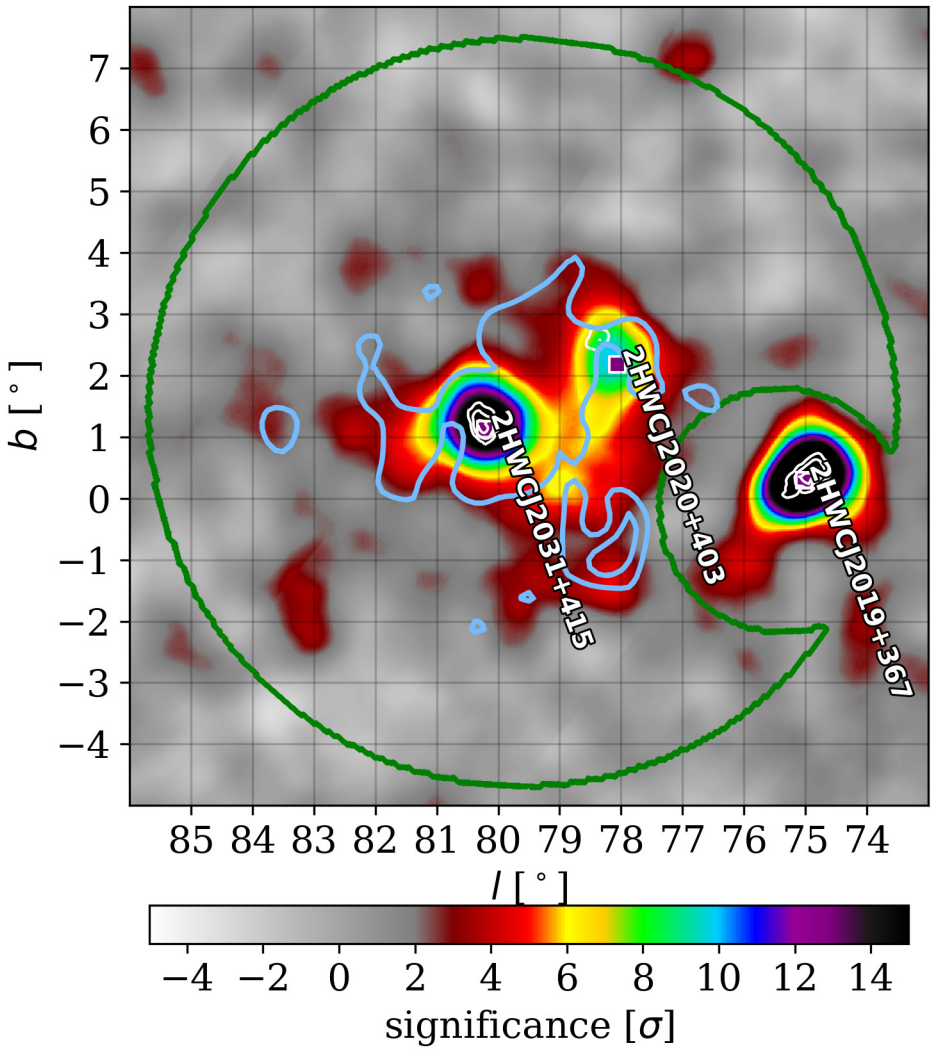

Figure 6.1: Significant map of the Cocoon region with 1038 days of HAWC data produced using the ρ_{40} energy parameter. The green contour is the region of interest. The white contours are VERITAS 5, 7 and 9 σ significance contours for VER J2031+415 [7]. The sky blue contours are the (RA, DeC) for 0.16 photons/(0.1°by 0.1°spatial bin).

A multi source model is developed to comprehensively describe the Cocoon region and then fitted using the maximum likelihood code of threeML [16]. The region of 2HWC J2031+415 is co-located with the two sources listed in the Table 6.1. In HAWC data, it is modeled by two sources: a slightly extended 2D Gaussian source associated with the PWN and a TeV counterpart of the cocoon modeled as a 2D Gaussian with a 2° extent (this document refers to it also as the HAWC cocoon). 2HWC J2020+403 (γ Cygni) is simultaneously fit as an extended disk with 0.63° radius.

Before successfully disentangling the 2HWC J3031+415 region, we tested various models, a few of which are listed the Table 6.2. We started with fitting one extended source at the 2HWC J2031+415 region and one source at the 2HWC J2020+403 region. After subtracting the best fit model, there is residual γ-ray emission at the 2HWC J2031+415 region not accounted for by the 2-source model. Then we tested a three-source model which includes two components at the J2031+415 region and checked if the TS value is significantly improved after the adding another source. We can see from the Table 6.2 that fitting two components at 2HWC J2031+415 (Model 2 to Model 5) in comparison to only one extended component (Model 1) significantly increases the overall likelihood (or decreases -log(Likelihood)) of the entire model. The γ-ray excess at 2HWC J2031+415 is best described by two components; HAWC J2031+415 (HAWC PWN), a slightly extended source associated with the

PWN [52] and HAWC J2030+409 (HAWC Cocoon), a TeV counterpart of the Cocoon.

Various models were then explored to find the best fit spectral and morphological description of the HAWC PWN and the HAWC Cocoon. They are listed in the Table 6.2. For easy references, the models are named as Model 1, Model 2, Model 3 etc. based on the spatial and spectral models used to describe the γ-ray emission at the Cocoon region. In all of these compared models, the multi-source component 2HWC J2020+403 is modeled in the same way. According to both, Δ TS and Δ BIC, Model 5 is the best description of the region.

For the spectral shape, the free parameters were N_0 and Γ for the power law spectrum as in Equation 5.2 and N_0, Γ and E_c for the power law spectrum with an exponential cutoff as in Equation 5.3. The pivot energies (E_0) are 4.9 TeV for the PWN and 4.2 TeV for the Cocoon. They were determined by calculating the co-variance between flux norm and index for various energies and choosing the energy where the co-relation between these two parameters approaches zero. This is shown in Fig. 6.2 and Fig. 6.3. As for the third source HAWC J2020+403, the spectrum is fit using the power law assumption of Equation 5.2 deriving the best fit values for the free parameters, N_0 and Γ. E_0 is fixed at 1.1 TeV.

Model Descrption	**Spectral Models** PL - Powerlaw PLC - PL with cutoff	**Δ TS w.r.t. model 1**	**Δ BIC w.r.t. model 1**
Model 1 One extended source	PLC	0	0
Model 2 One extended source and VERITAS PWN (fixed)	HAWC PWN PL HAWC cocoon PL	58	-88
Model 3 One extended source (Cocoon) and one point source (PWN)	HAWC PWN PLC HAWC Cocoon PL	72	-60
Model 4 Two extended sources	HAWC PWN PL HAWC Cocoon PL	124	-124
Model 5 Two extended sources	HAWC PWN PLC HAWC Cocoon PL	140	-126

Table 6.2
A comparison of the various models tested in the 2HWC J2031+415 region.

Equations 5.2 and 5.3 constitute nested models, and can be compared using Wilk's theorem. The delta TS for the nested models between Model 4 and Model 5 is 15 and the delta TS for the nested models Model 2 and Model 4 is 12.4. Using Wilk' theorem this corresponds to the power law spectrum with cutoff being preferred by roughly 4 σ for the PWN. The cutoff energy obtained is (31 - 10 + 20) TeV. In case of the Cocoon spectrum, there is no significant preference of spectral curvature in comparison to a simple power law spectrum. When comparing the Δ TS for the Cocoon spectrum described by Eq. 5.3 vs 5.2, the TS of the model does not change. Hence, a simpler model or a simple power law spectrum is used to describe the HAWC Cocoon source.

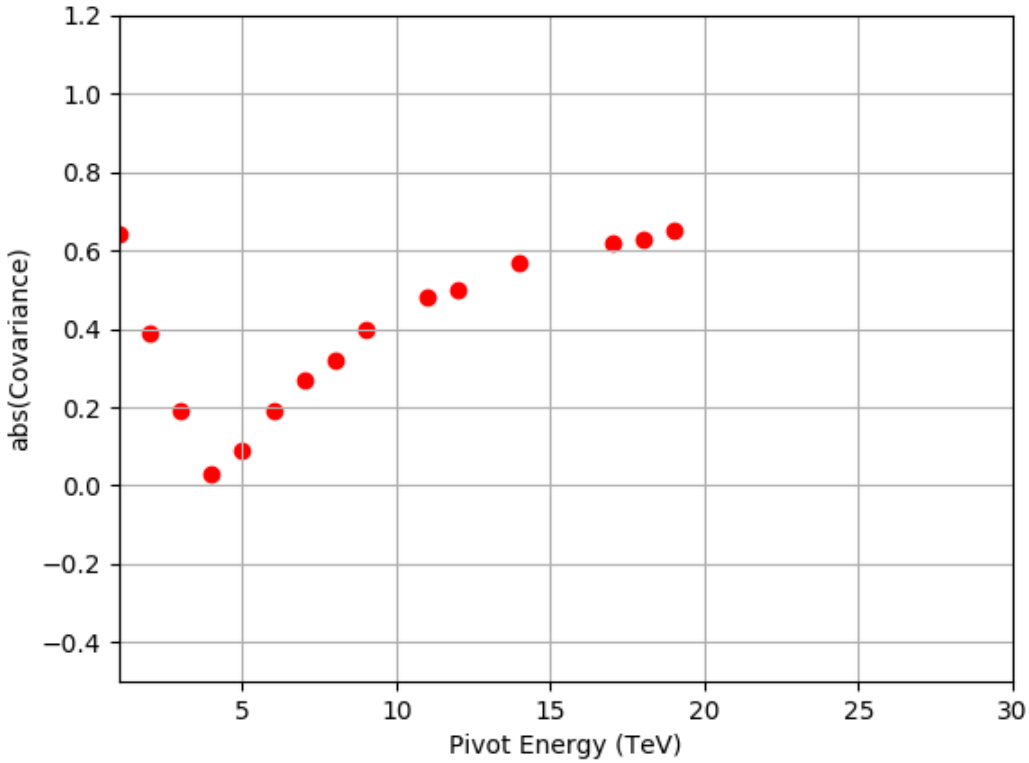

Figure 6.2: Co-variance between flux norm N_0 and index Γ vs energies for the HAWC Cocoon.

Ihe free parameter of the spatial model is the Gaussian radius, σ. Different spatial shapes were explored for the PWN and the Cocoon: a point source, an extended disk source, and an asymmetric Gaussian morphology. Both, the HAWC PWN and HAWC Cocoon are best described by 2D Gaussian function $f(\vec{x})$ as

$$f(\vec{x}) = \left(\frac{180^\circ}{\pi}\right)^2 \frac{1}{2\pi\sqrt{\det \Sigma}} \exp\left(-\frac{1}{2}(\vec{x}-\vec{x}_0)^\intercal \cdot \Sigma^{-1} \cdot (\vec{x}-\vec{x}_0)\right) \tag{6.1}$$

where $\vec{x}_0$ refers to $(\mathrm{RA}_0, \mathrm{Dec}_0)$ and Σ is covariance matrix such that,

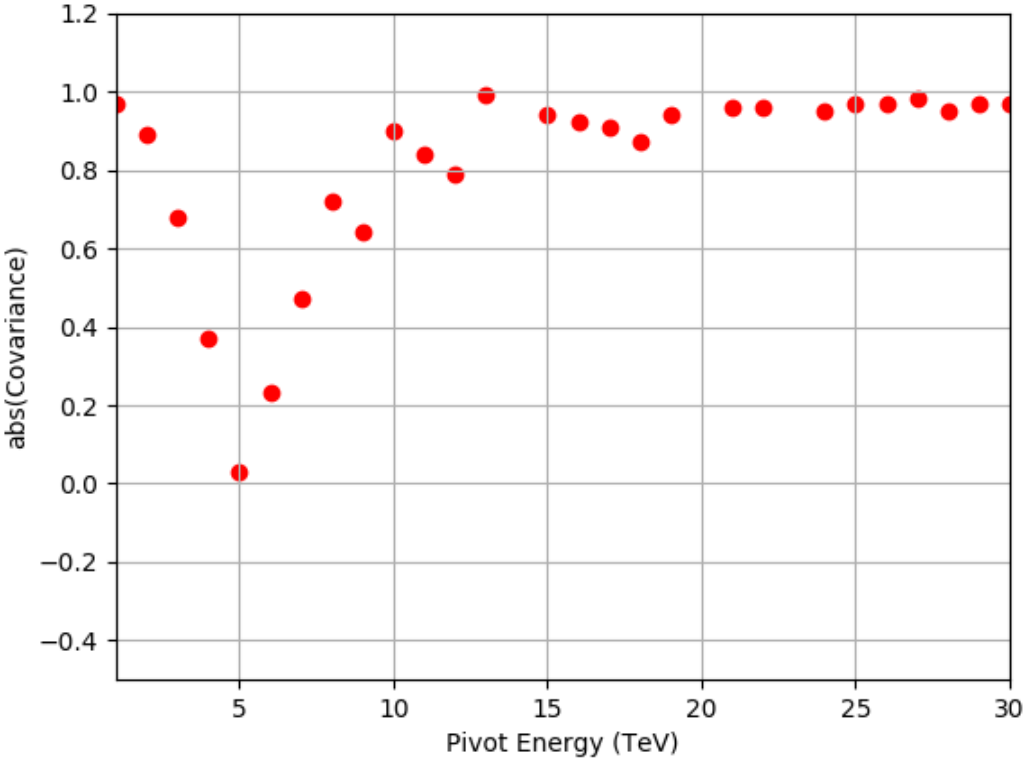

Figure 6.3: Co-variance between flux norm N_0 and index Γ vs energies for the HAWC PWN.

$$\text{for } \Lambda = \begin{pmatrix} \sigma^2 & 0 \\ 0 & \sigma^2(1-e^2) \end{pmatrix} \text{ and } U = \begin{pmatrix} \cos\theta & -\sin\theta \\ \sin\theta & cos\theta \end{pmatrix}, \Sigma = U\Lambda U^{\intercal}$$

Here, σ refers to the standard deviation of the Gaussian distribution.

Sources	**Source Name** at Pivot Energy (TeV)	**Source Association**	**TS**
1	HAWC J2031+415 at 4.9 TeV	VER J2031+415 PWN	214.4
2	HAWC J2030+409 at 4.2 TeV	Fermi-LAT Cocoon	148.2
3	2HWC J2020+403 at 1.1 TeV	γ Cygni SNR	48.0

Table 6.3
Source association and TS of the sources in the ROI

Sources	**Morphology**	**Flux Norm** (N_0)$\times 10^{-13}$ ($\mathrm{TeV}^{-1}\mathrm{cm}^{-2}\mathrm{s}^{-1}$)	**Index** (Γ)	**Cutoff** (E_{cut}) (TeV)
1	Gaussian radius of $(0.27\pm0.03)^\circ$	$1.37^{+0.23}_{-0.19}$	$-1.89^{+0.23}_{-0.19}$	31^{+20}_{-10}
2	Gaussian radius of $(2.12\pm0.03)^\circ$	9.5 ± 1.0	-2.65 ± 0.05	
3	Disk radius of $(0.63)^\circ$	4.3 ± 0.7	$-3.00^{+0.13}_{-0.14}$	

Table 6.4
Morphological and Spectral fit results for the sources in the ROI

6.2 Residual of the fit

This section will explore the residual maps and significance distributions to check for the analysis biases and any unaccounted remaining excesses.

6.2.1 Model and Residual Maps

Fig. 6.4 shows the model map of the source located at VER J2031+415. Fig. 6.5 shows the HAWC cocoon model located at the Fermi-LAT Cocoon location. Fig. 6.6 shows the disk model with 0.63° radius [57] for 2HWC J2020+403 (γ Cygni). Fig. 6.7 is the model map with all three sources.

The residual map in the Fig. 6.8 obtained after subtracting the best fit model (Model 5 in Table 6.2 with three sources in the region) shows that the model is a good description of TeV γ-ray emission in this region. The remaining $< 3.5\ \sigma$ spots in the residual map are most probably statistical fluctuations. Further studies of residual emission after subtracting different fitted models are discussed in Section 6.2.3. The residual map in Fig. 6.8 and the binned count residuals in Fig. 6.9 do not show significant additional TeV emission in the ROI not described by the best fit model. This supports the case that the other HAWC catalog source 2HWC J2024+417 [3] detected in the region with TS < 40 is likely is an extended morphology of the HAWC Cocoon.

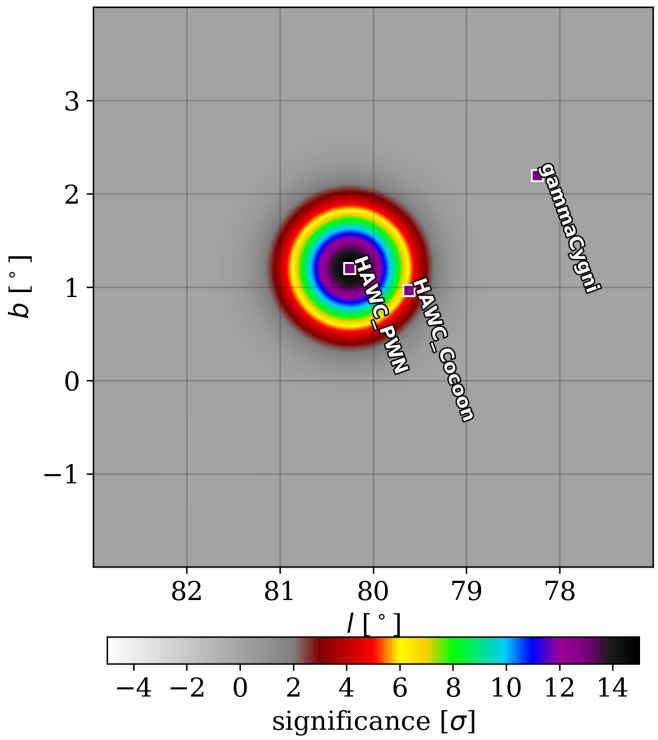

Figure 6.4: Significance map of the model used for the HAWC PWN. The spatial distribution is described with a Gaussian radius of 0.27 °. The spectral energy distribution is best fit by a simple power law spectrum with an exponential cutoff. The map has been smoothed with a Gaussian radius of 0.5°.

6.2.2 Radial Distribution

Fig. 6.10 shows the total event excess per steradian averaged over rings of 0.067°width, centered at the 2HWC J2031+415 location, out to a distance of 2°from the center. The blue line represents the shape for the HAWC PWN used in model 5 in Table 6.2. We can see that while the model explains the central peak emission at the

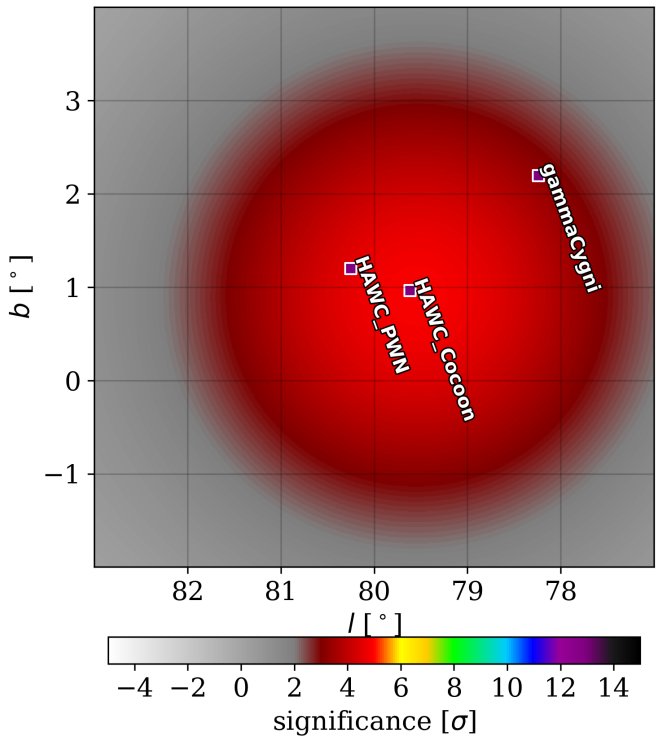

Figure 6.5: Significance map of the model used for the HAWC Cocoon. The spatial distribution is described with a Gaussian radius of ~ 2 °. The spectral energy distribution is best fit by a simple power law spectrum. The map has been smoothed with a Gaussian radius of 0.5°.

2HWC J2031+415 location, the Gaussian does not fit the tails well (excess emission of more than $\sim 0.5°$ away from the 2HWC J2031+415 location. This excess emission is contributed by the HAWC Cocoon emission. γ Cygni is located at a distance of 2.36° from the center of the HAWC PWN and 1.72° from the center of the HAWC Cocoon. Hence, this radial distribution does not include most of the γ-ray emission from the γ Cygni SNR.

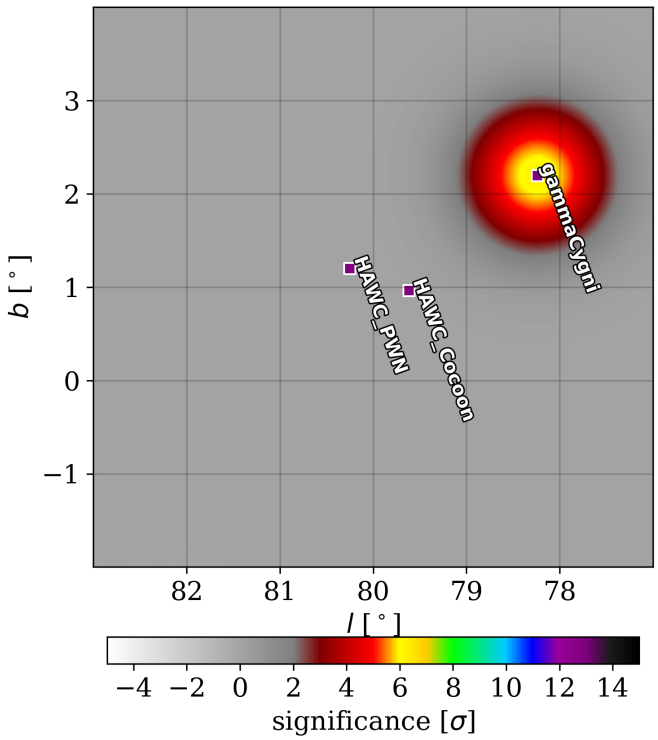

Figure 6.6: Significance map of the model used for the HAWC Cocoon. The spatial distribution is described with a disk of 0.63°. The spectral energy distribution is best fit by a simple power law spectrum. The map has been smoothed with a Gaussian radius of 0.5°.

6.2.3 Significance Distribution

Shown in Fig. 6.1 is the HAWC data map before the maximum likelihood fit with the ROI circled in green. The distribution of pixel significance in the ROI is shown in Fig. 6.11. The significance values are shown in units of Gaussian σ. If the residual map obtained after subtracting the model contains only background fluctuations,

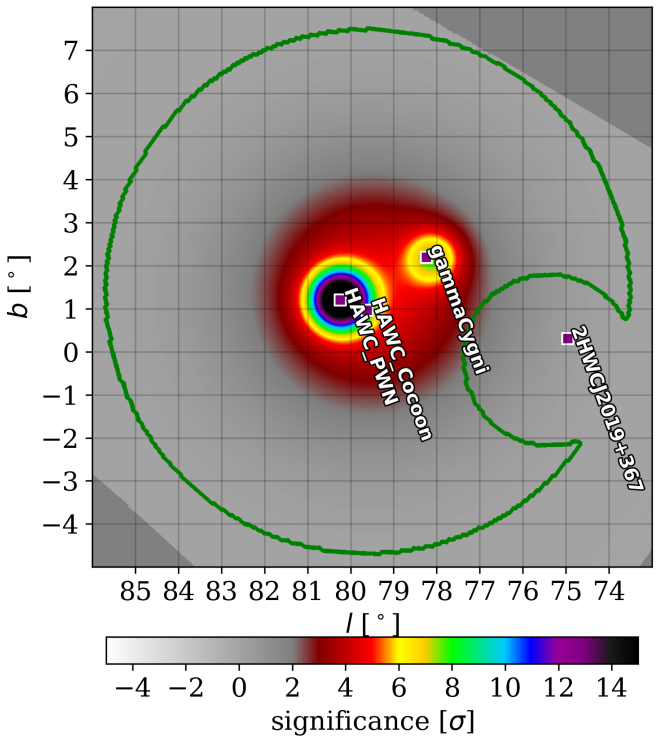

Figure 6.7: Significance map of the best fit combined model (model 5 in Table 6.2. The map has been smoothed with a Gaussian radius of 0.5°.

then the significance histogram should follow a normal distribution. In that case the mean of the distribution should be close to zero and the width should be about 1 σ. The dotted lines in the plots are the expected and the obtained distribution. The significance distribution in Fig. 6.11 is skewed towards positive values due to the presence of different γ-ray sources. Because of these sources, we see excess counts above background fluctuations.

After subtraction of the PWN and the γ Cygni SNR, Fig. 6.12 shows considerably

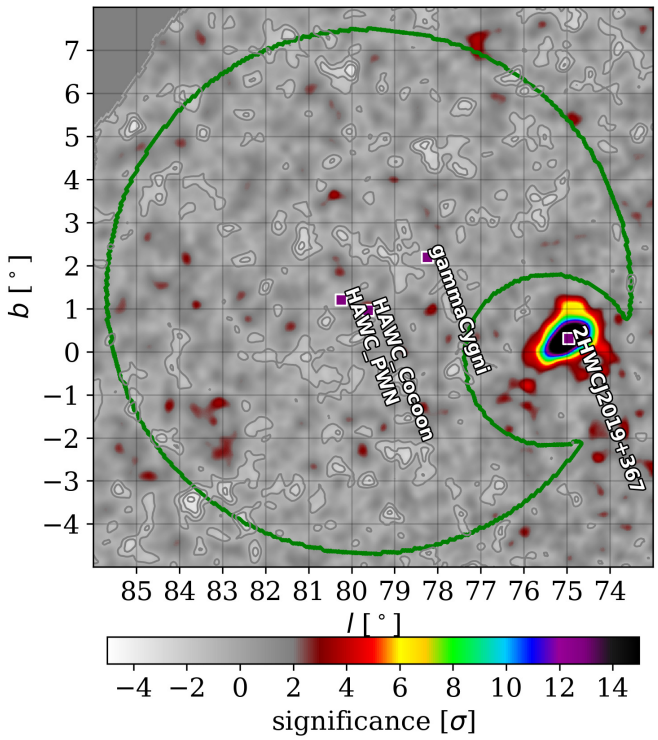

Figure 6.8: Residual map after subtracting the best fit model. The grey contours are -1, -2, -3 and -4 contours to check for over subtraction of excess.

reduced skew. The excess counts from the Cocoon source contribute to this skew. Finally, in Fig. 6.13 in which the Cocoon source in addition to the PWN and γ Cygni are subtracted, there is no longer significant excess counts over background fluctuations.

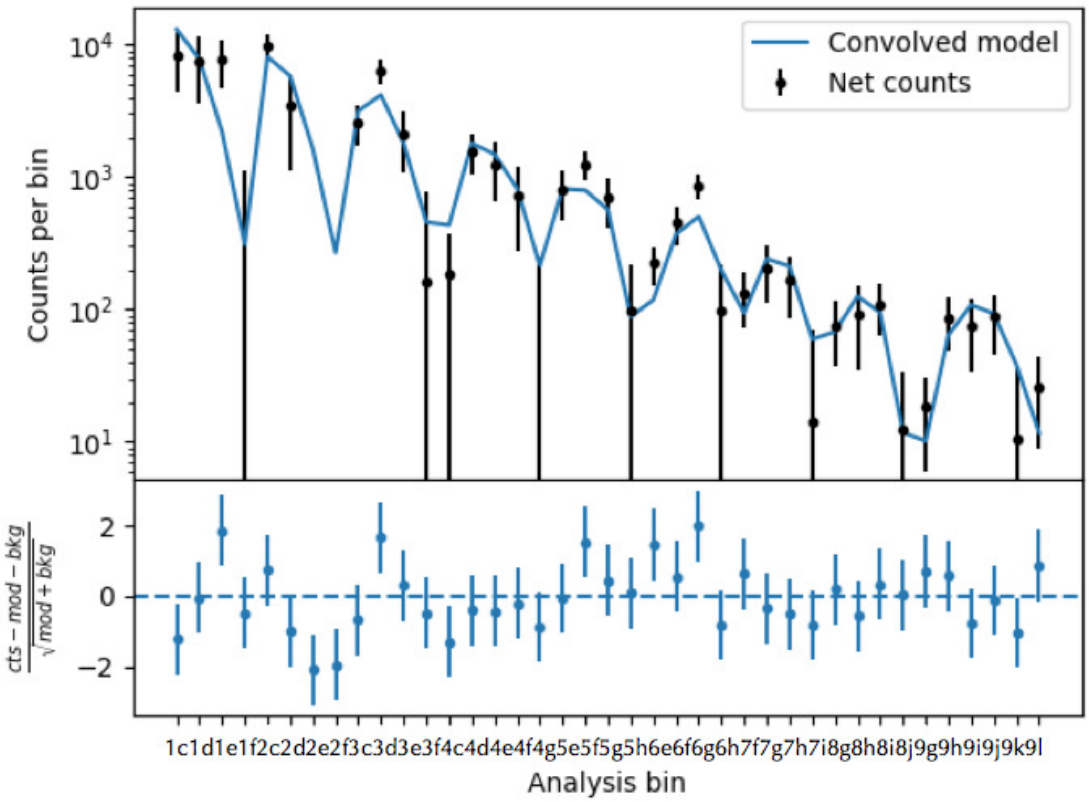

Figure 6.9: Net residual counts in each bin used for the analysis.

6.2.4 Energy Range

A study similar to the energy range method presented in [58] was performed to determine the lower limit of the maximum energy and upper limit of the minimum energy for the detection of γ-ray emission from the HAWC cocoon. As a power law spectrum is favored for the HAWC cocoon, the Equation 5.2 is multiplied by a step function to estimate a strict energy cutoff by fitting the product to the data. The free parameters of this fit are the strict upper or lower cutoff for the energy. All the

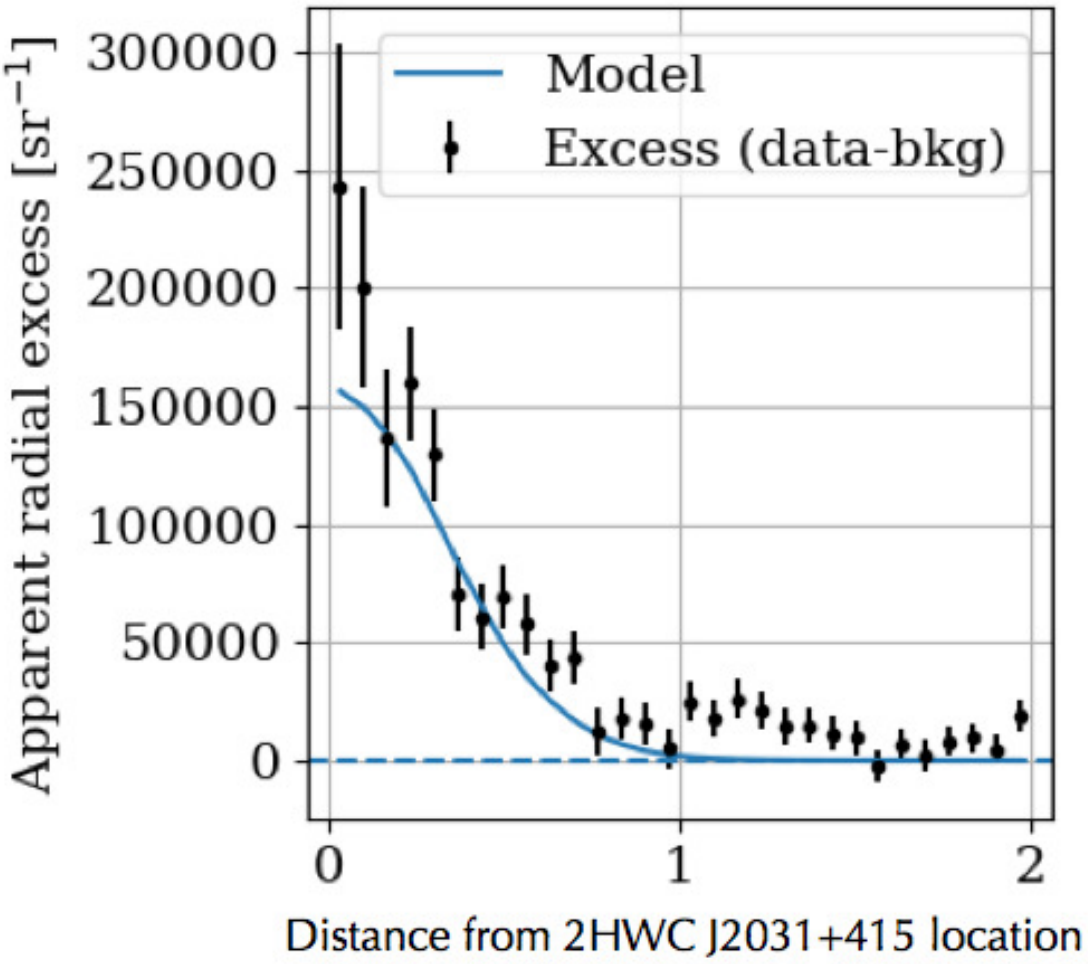

Figure 6.10: Radial profile centered on the cocoon location. **Blue line** is the VER J2031+415 model. **(b)**: Profile centered on the HAWC cocoon location after subtraction of VER J2031+415. **Blue line** is the model used for the HAWC cocoon and γ Cygni emission.

other parameters are fixed to the best fit values previously listed in Table 6.4 and Table 6.3. The energy value where the log(likelihood) crosses the 1 σ threshold for the upper energy range fit is quoted as the lower limit to the maximum γ-ray energy. Similarly, the energy value where the log(likelihood) crosses the 1 σ threshold for the lower energy range fit is quoted as the upper limit to the minimum γ-ray energy.

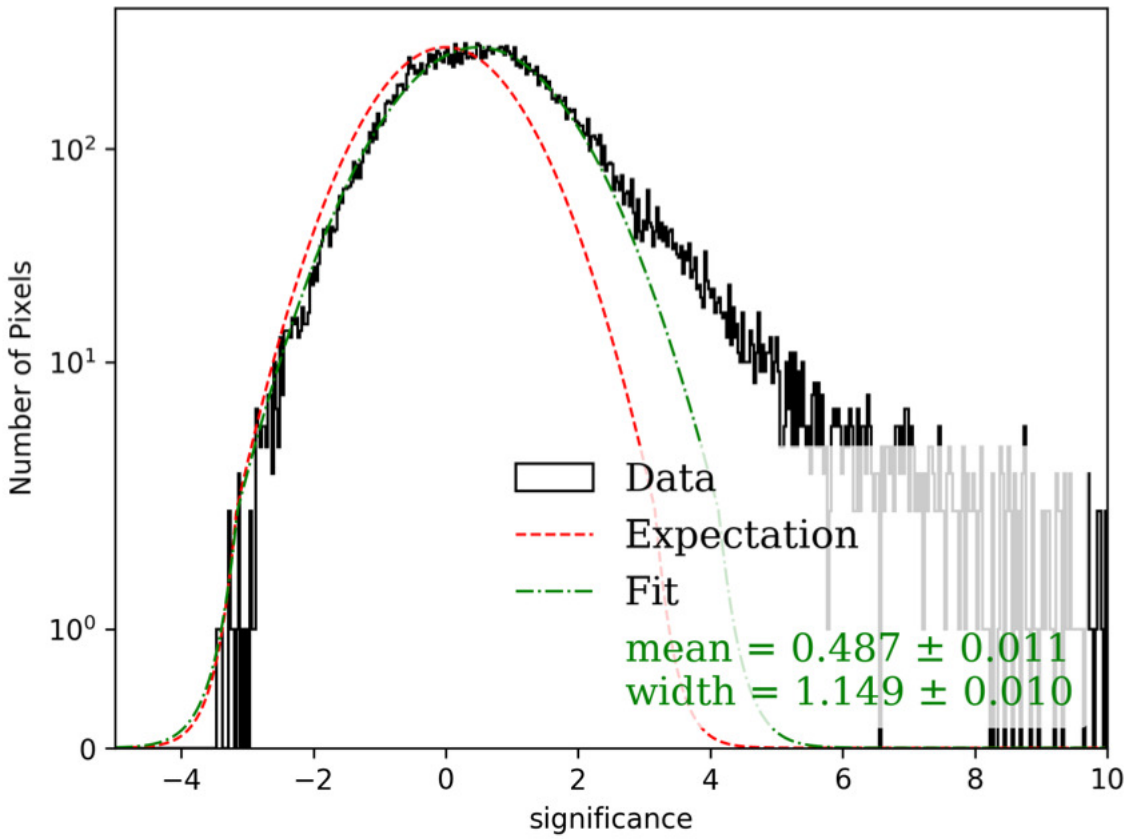

Figure 6.11: Distribution of excess significance before any source subtraction in the given ROI overlaid with the best fit Gaussian distribution expectation of a Gaussian of mean zero and width 1.

The likelihood profiles used in this study are shown in Figures 6.15 and 6.14 for the HAWC Cocoon and in Figures 6.17 and 6.16 for the HAWC PWN.

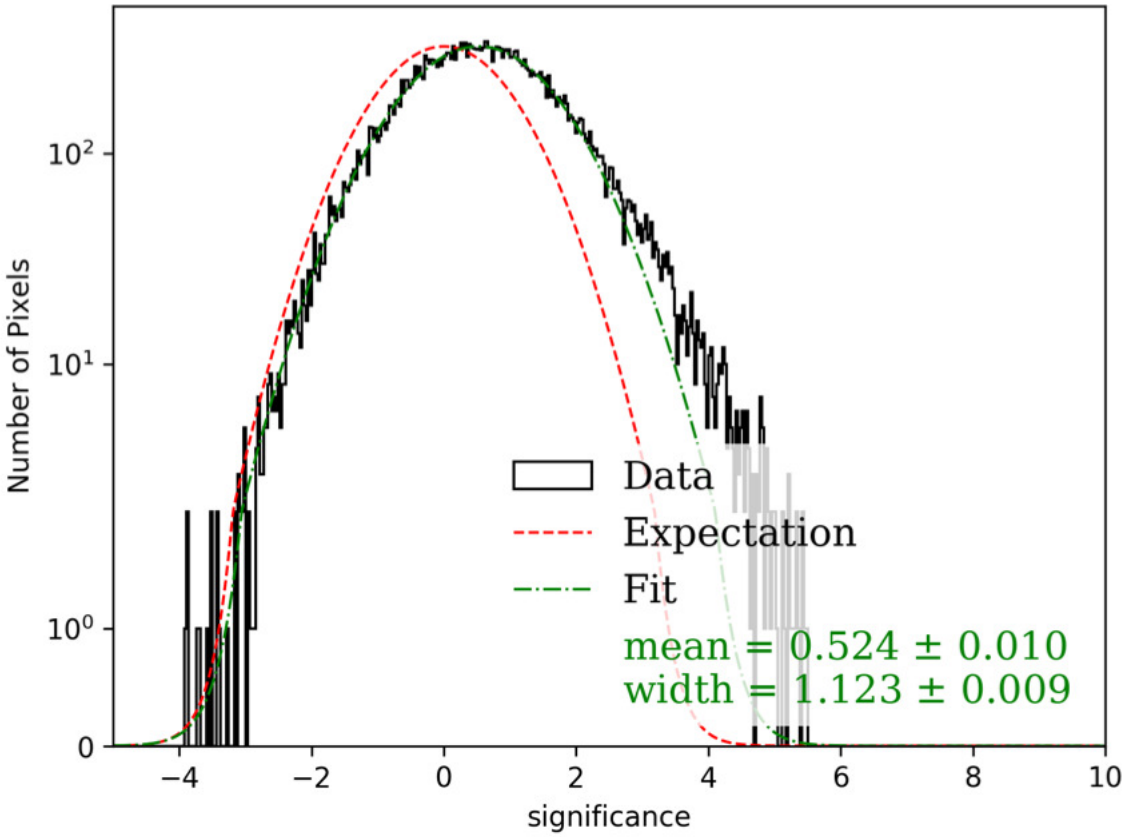

Figure 6.12: Distribution of excess significance after subtracting the HAWC PWN & γ Cygni overlaid with the best fit Gaussian distribution expectation of a Gaussian of mean zero and width 1.

6.3 Morphology and Spectral Energy Distribution of the HAWC Cocoon

The significance map of the HAWC Cocoon after subtracting the HAWC PWN and γ Cygni is shown in Fig. 6.18. The best fit position for the HAWC Cocoon using HAWC data is (RA, Dec = 307.65 ± 0.03, 40.93 ± 0.03) °. The Gaussian width obtained is (2.12± 0.16)°. This width agrees with the Gaussian width obtained for

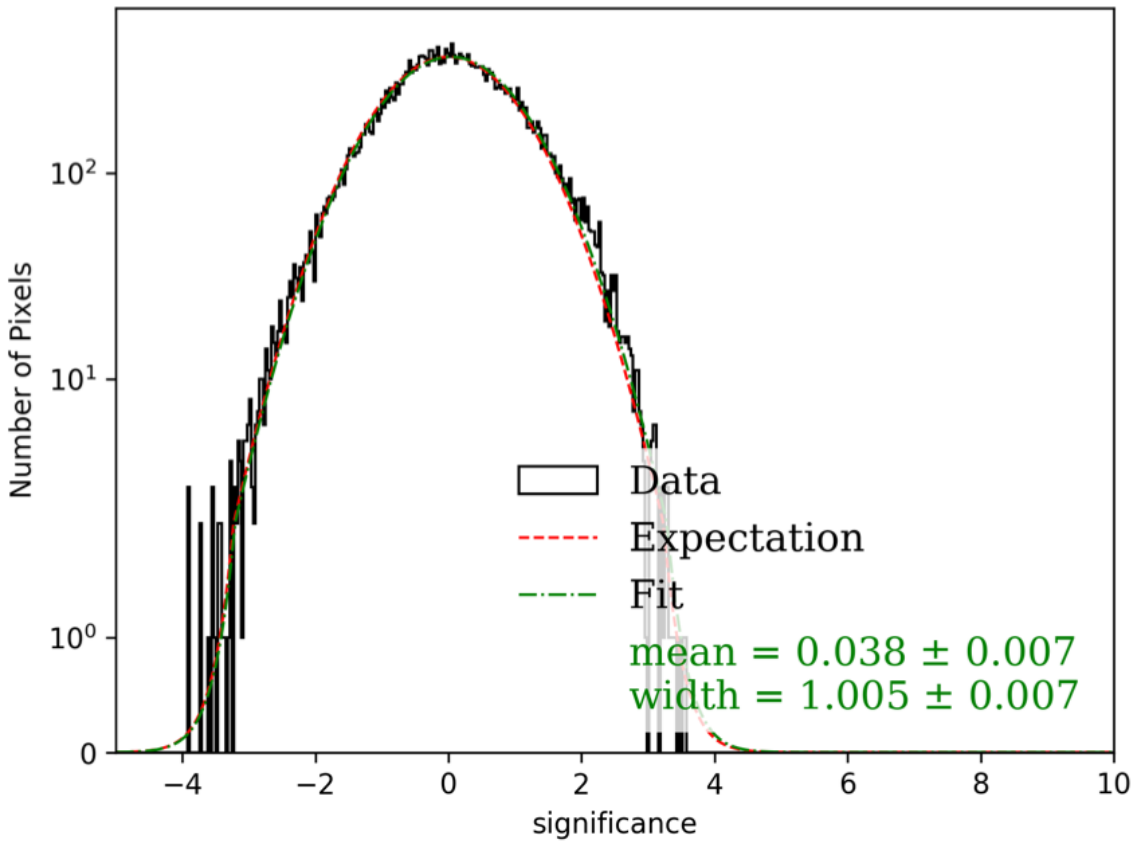

Figure 6.13: Distribution of excess significance after subtracting the complete model 5 overlaid with the best fit Gaussian distribution expectation of a Gaussian of mean zero and width 1.

the GeV Fermi-LAT Cocoon within statistical uncertainties [**?**].

This large extended source contributes $\sim 90\%$ to the total flux detected in the 2HWC J2031+415 region. Fig. 6.19 shows the spectral energy distribution of the HAWC Cocoon and the TS values in each energy bin (c, d, e, f, g, h, i, j, k and l). Each bin represents a quarter decade in energy. For the following studies and discussion, the highest-energy four bins (i, j, k and l), where the statistics is low, are combined into half decade bins. That means, bins i and j are combined into one half decade bin and

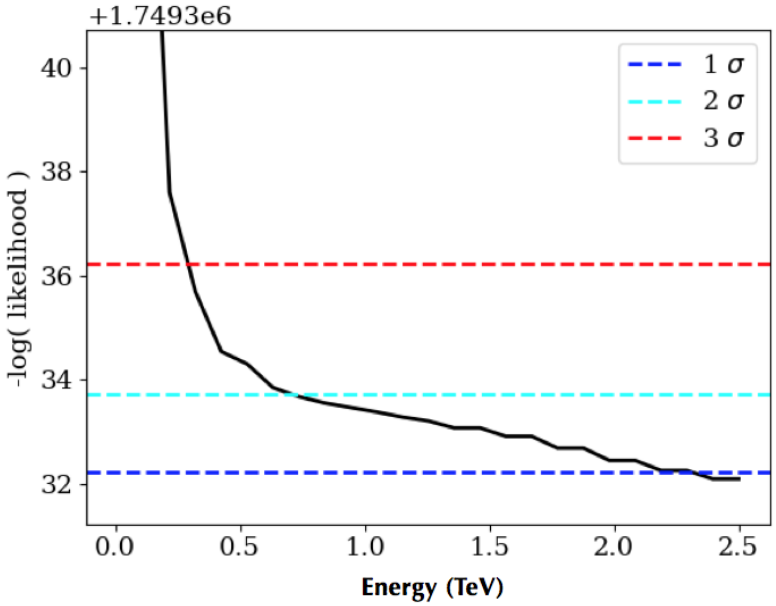

Figure 6.14: Negative log(likelihood) profile vs energy to determine minimum maximum energy for the HAWC Cocoon. The dashed lines represent the 1, 2 and 3 σ thresholds of the fit.

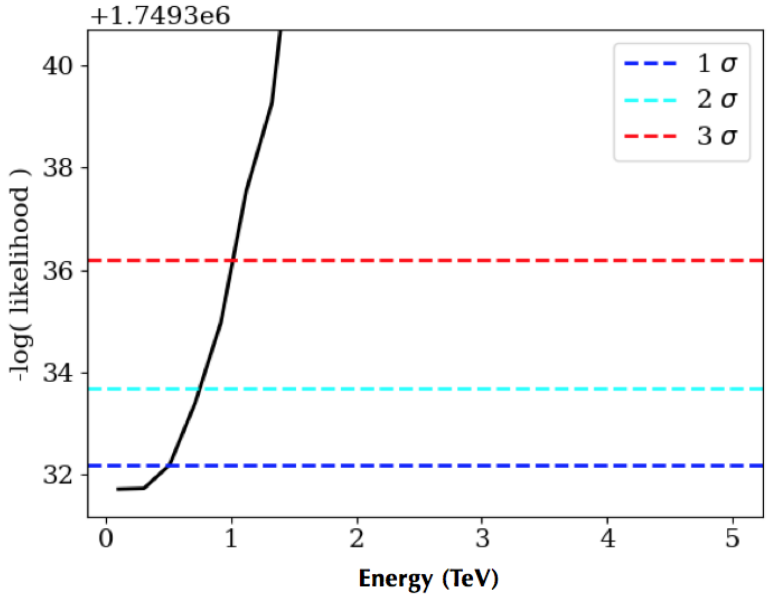

Figure 6.15: Negative log(likelihood) profile vs energy to determine maximum minimum energy for the HAWC Cocoon. The dashed lines represent the 1, 2 and 3 σ thresholds of the fit.

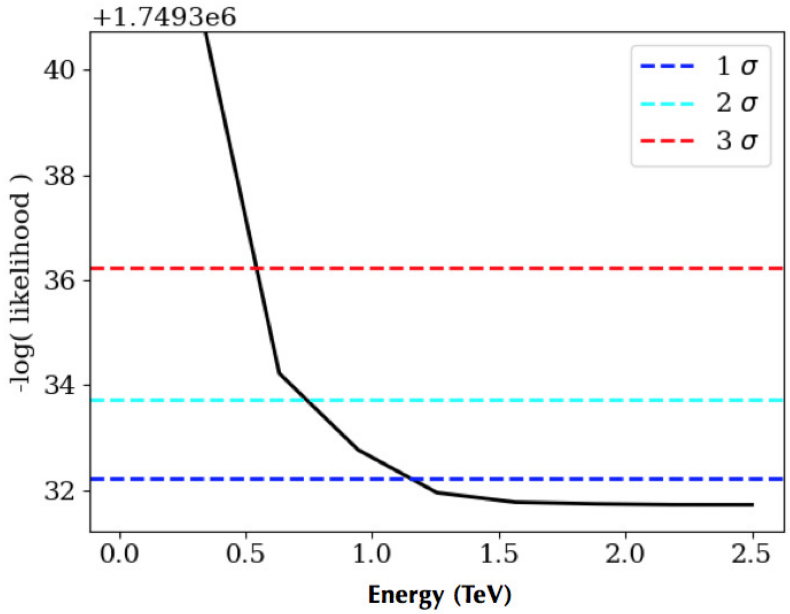

Figure 6.16: Negative log(likelihood) profile vs energy to determine minimum maximum energy for the HAWC PWN. The dashed lines represent the 1, 2 and 3 σ thresholds of the fit.

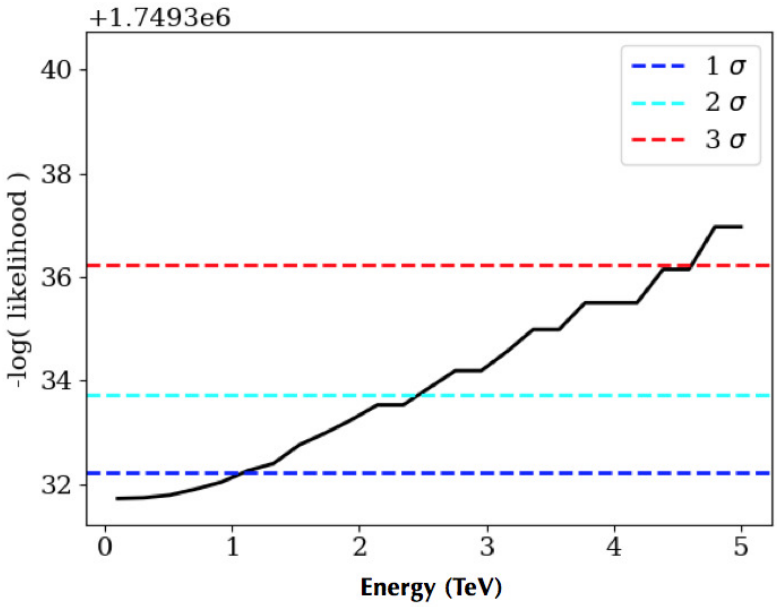

Figure 6.17: negative log(likelihood) profile vs energy to determine maximum minimum energy for the HAWC PWN. The dashed lines represent the 1, 2 and 3 σ thresholds of the fit.

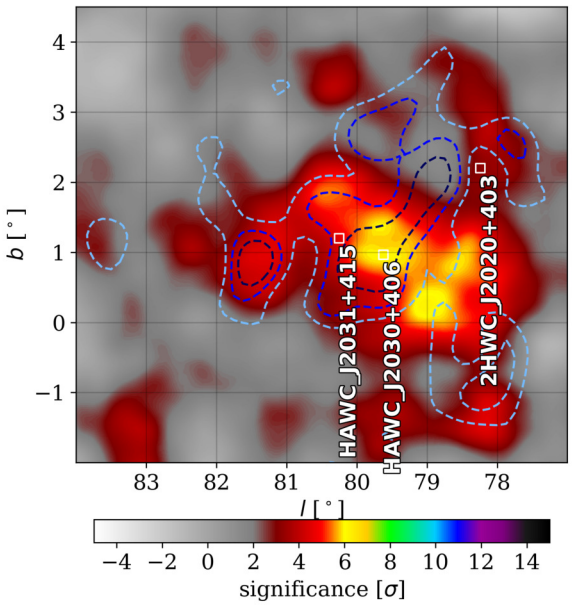

Figure 6.18: Significance map of the cocoon region after subtracting known TeV sources with 0.5°extended Gaussian source assumption and 1038 days of HAWC data. The lighter and darker blue dashed lines are 0.16, 0.24 and 0.32 photons/(0.1°by 0.1 °spatial bin) contours from FERMI-LAT Cocoon.

k and l into the other half decade bin.

6.3.1 GeV-TeV Spectrum

The spectral index of the TeV Cocoon emission measured by HAWC is -2.64±0.06, which is softer in comparison to the GeV spectrum. The same is true for low TeV energy spectrum reported by the ARGO Collaboration for ARGO J2031+4175, which is located at (RA, DeC) = (307.8°± 0.8°, 42.5°± 0.6°). The ARGO Collaboration quotes a spectral index of -2.6 and has been suggested as a counterpart of the Cocoon

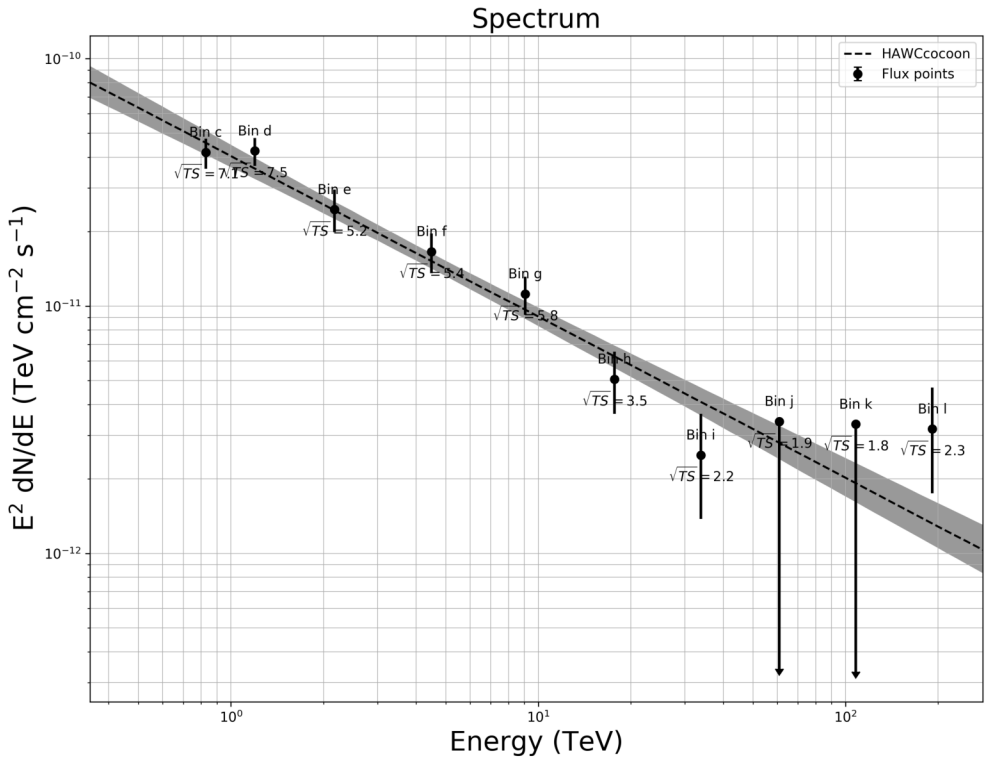

Figure 6.19: Spectral energy distribution of the HAWC Cocoon [9].

at TeV energies [8]. The spectral energy distributions measured by HAWC and ARGO agree within their uncertainties in the overlapping energy range.

A combined GeV-TeV spectrum is obtained by simultaneously fitting Fermi-LAT and HAWC data points. After the initial publication of the Fermi-LAT Cocoon spectrum in 2011, the 3FGL, 3FHL and 4FGL catalog have reported the spectrum with additional years of data. All of these spectra reported a 10-15% higher flux than the 2011 paper [10, 80**?**]. The latest spectrum published in 2018 is the 4FGL spectrum. The combined spectral fit from GeV to TeV using 4FGL and HAWC data

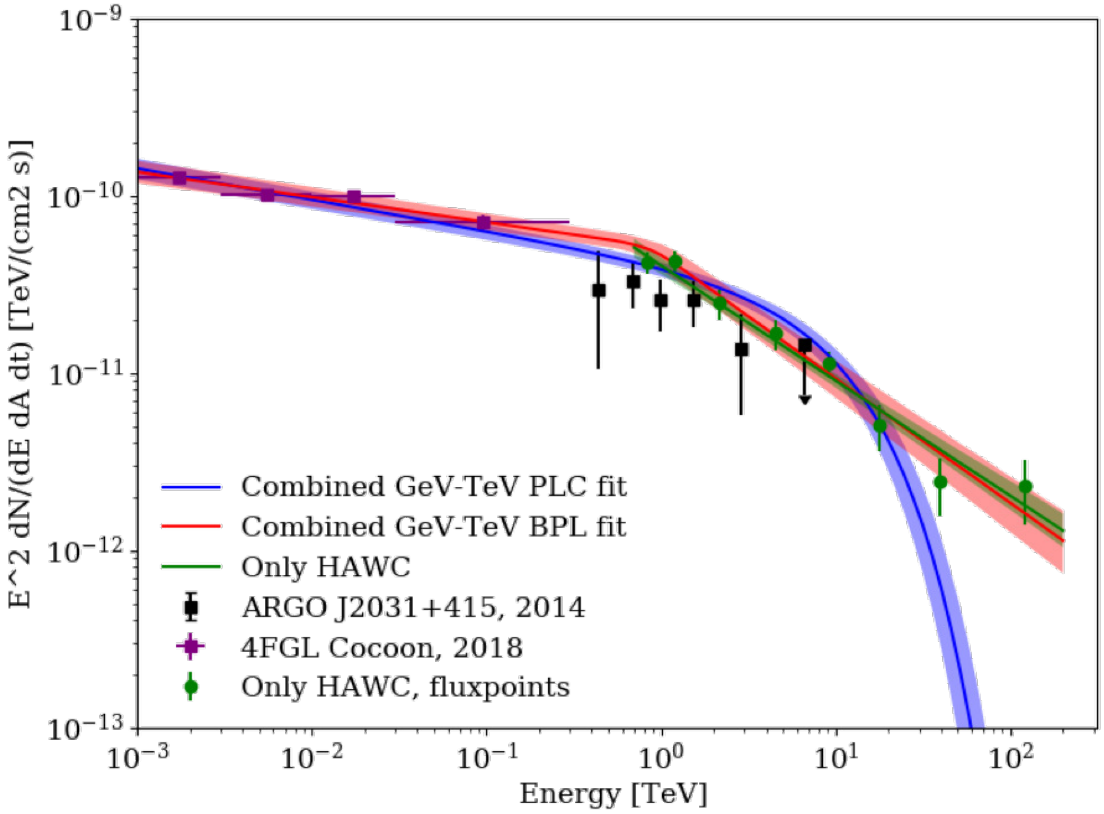

Figure 6.20: Spectral energy distribution of the Cocoon from GeV to TeV range. **Red and Blue**:GeV-TeV Cocoon spectrum with 4FGL data points and HAWC data assuming a broken power law spectrum as shown in equation 5.10 and a power law spectrum with an exponential cutoff as shown in equation 5.3 respectively. **Green**: HAWC cocoon spectrum and flux points obtained from the best fit model. **Purple**: Fermi-LAT cocoon spectrum [**?**]. **Black**: ARGO J2031+415 flux points [8].

points is [10] and HAWC data is shown in Fig. 6.20.

Assuming a broken power law (BPL) spectrum as described in equation 5.10, the best fit flux norm at 4.2 TeV is $2.38^{+0.4}_{-0.34}$ (stat.) $\times 10^{-12}$ TeV^{-1}cm^{-1}s^{-1}. The break occurs at $0.79^{+0.40}_{-0.27}$ (stat). TeV. Index before the break is -2.14 ± 0.02 (stat). and

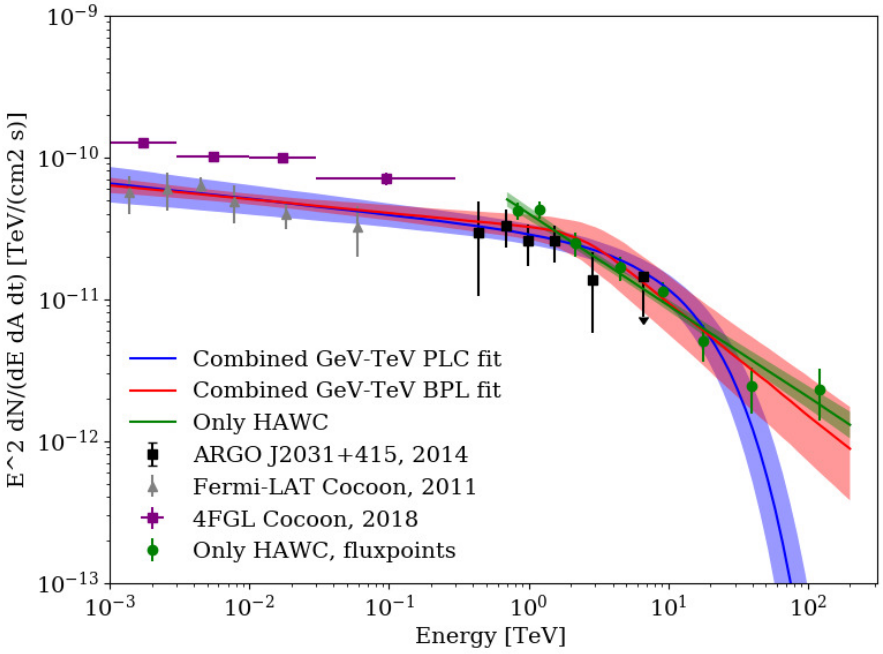

Figure 6.21: Spectral energy distribution of the Cocoon from GeV to TeV range. **Red and Blue**: GeV-TeV Cocoon spectrum with Fermi-LAT Cocoon (2011) data points and HAWC data assuming a broken power law spectrum as shown in equation 5.10 and a power law spectrum with an exponential cutoff as shown in equation 5.3 respectively. **Green**: HAWC cocoon spectrum and flux points obtained from the best fit model. **Purple and Grey**: Fermi-LAT cocoon spectrum, 2018 and 2011 respectively [10**?**]. **Black**: ARGO J2031+415 flux points [8].

after the break is $-2.7^{+0.07}_{-0.08}$ (stat). Assuming a power law spectrum with an exponential cutoff (PLC) as described in equation 5.3, the best fit flux norm at 4.2 GeV is $1.84^{+0.17}_{-0.16}$ (stat.) $\times 10^{-12}\mathrm{TeV}^{-1}\mathrm{cm}^{-1}\mathrm{s}^{-1}$. The cutoff energy is 111^{+23}_{-19} (stat). TeV and the index is -2.18 ± 0.01 (stat).. The difference in BIC between the two assumptions is only 2.5 with the PLC yielding a lower BIC value. Hence, it is not possible to distinguish which is preferred with the current statistics. However, both of these assumptions are significantly preferred in comparison to a power law spectrum. The Cocoon spectrum from GeV to TeV regime can be best described by a spectral shape

that has a curvature.

I also studied the GeV to TeV spectrum using the 2011 spectrum in [**?**] and HAWC data, shown in Fig. 6.21. The results do not change significantly. In this case also, there was no clear preference between a BPL and a PLC spectrum. Assuming a BPL spectrum in equation 5.10, the best fit flux norm is $2.38^{+0.4}_{-0.34}$ (stat.) $\times 10^{-12}\text{TeV}^{-1}\text{cm}^{-1}\text{s}^{-1}$. The break occurs at $0.79^{+0.40}_{-0.27}$ (stat) TeV. The index before the break is -2.14 ± 0.02 (stat) and after the break is $-2.7^{+0.07}_{-0.08}$ (stat). Assuming the PLC spectrum in equation 5.3, the cutoff energy is 142^{+50}_{-32} (stat) TeV and assuming a BPL spectrum, the break is at $2.4^{+1.8}_{-1.0}$ (stat) TeV. The indexes for both assumptions agree with the study done with the 4FGL data points. Including ARGO J2031+415 data points in the fit also only affected the spectrum by less than 3%.

6.4 Systematic Studies

This section will present a set of studies which result in maximum and minimum deviation from the best fit values for the fit parameters to calculate the net systematic uncertainties.

6.4.1 Detector Systematic Effects

Table 6.5 lists of the results of the studies done for various detector systematic effects. The effects considered are briefly discussed here. In all of these studies different detector response files are created for various scenario and the fits of multi-source Model 5 in Table 6.2 are repeated for each response file. The PMT threshold i.e. the minimum charge which can be detected by the PMT used in the simulation of Monte Carlo (MC) is 0.2 PE. The effects of varying this by $\pm 1\sigma$ or ± 0.05 are considered [34]. PMT efficiency refers to how efficiently the PMT can detect the PE signal. Simulated data sets are produced varying the absolute PMT efficiency by $\pm 10\%$ [4]. The wider arrival time distribution of PE (broad pulse) is investigated to study its effect on the different fit parameters. Additionally, the charge uncertainty which accounts for the difference in PMT measurements for a fixed amount of light and its effect on the fit parameters are explored. Finally, the effects of angular resolution by enlarging the PSF by 0.5°are also investigated. The total systematic uncertainties from the detector effects contributed to $\pm 7\%$ towards the flux norm as shown in the Table 6.7. The uncertainties in the index and Gaussian width due to the detector effects were negligible ($< 2\%$).

Detector **Systematic**	**Flux Norm** $\times 10^{-13}$ ($\mathrm{TeV}^{-1}\mathrm{cm}^{-2}\mathrm{s}^{-1}$)	**Index**	**Gaussian Width** (degree)
Threshold	-0.3 +0.2	-0.01 +0.02	-0.01 +0.01
PMT efficiency	-0.1 +0.4	+0.04	-0.03
Broad pulse	-0.3	-0.02	+0.01
Charge uncertainty	-0.4 +0.4	+0.02	0
Angular resolution	0	0	+0.01

Table 6.5
Contribution to systematic uncertainties from various detector effects for the Cocoon parameters.

6.4.2 Alternate Analysis Approach - Neural Networks

Using the neural network instead of the parameter ρ_{40} to reconstruct γ-ray energies, I estimated the systematic difference measurements arising from different analysis approaches. The largest systematic uncertainty of (+14%) was found for the Gaussian source width.

6.4.3 ROI Size Effect

I also studied how the ROI size affects the HAWC Cocoon fit results. For this, the ROI size centered at (307.17°, 41.17°) is increased by including the masked region. At the same time, an extended asymmetric Gaussian source to model the emission from 2HWC J2019+367 [59]. The effect on the HAWC Cocoon fit parameters using this larger ROI is shown in Table 6.7. Deviations are smaller than 6%.

6.4.4 Extended and Diffuse Emission Effects

To test how unresolved point or extended source, or undetected Galactic diffuse emission (GDE) from the sea of old CRs, a large scale background source is added to Model 5 in Table 6.2. This is a dominant uncertainty on the flux norm. Two different spatial descriptions for the large scale background source are explored. In the first case, a Gaussian distribution symmetrically distributed about galactic latitude of b=0 degree and infinitely extended along galactic longitude is added. The model was originally intended to be an extremely simplified representation of galactic diffuse emission. The spectral energy distribution is assumed to be a power law. The latitudinal width of the Gaussian is fixed to be 2°, while the flux norm and spectral index are fit. The TS value did not improve significantly after addition of this background source. In

Systematic	Flux Norm $\times 10^{-13}$ ($\mathrm{TeV}^{-1}\mathrm{cm}^{-2}\mathrm{s}^{-1}$)	Index	Gaussian Width (degree)
Using NN bins	+0.5	+0.06	+0.30
Using larger ROI	+0.3	-0.01	+0.02
Using large uniform disk background	-0.4	-0.01	-0.02
Using large Gaussian background	-1.0	-0.01	-0.01

Table 6.6
Differences in the Flux Norm, Index and the Gaussian Width from the various systematic effects for the HAWC Cocoon.

the second case, a uniform background is added. The spectral energy distribution is described by a power law. Again, the free parameters in the fit are the flux norm and spectral index. The TS value changed by less than 2σ after the addition of a uniform background. Because these models for Galactic diffuse emission and Unresolved sources do not significantly improve the fit quality they are not included in the final model description of the HAWC Cocoon region. Their inclusion decreased the HAWC Cocoon flux by up to about 11%. However, this value is taken into account in the systematic error estimate (see Table 6.7).

6.4.5 Total Systematic Uncertainties

The total systematic uncertainties on the flux norm, index and the Gaussian width are calculated by adding all contribution in quadrature and are also listed in Table 6.7.

Contribution	Flux Norm	Index	Gaussian Width
	%	%	%
Detector effects	±7%	+1.9%	+0.8%
		-0.8%	-1.5
Using NN bins	+5.3%	+2.3%	+14.2%
Larger ROI	+3.2%	-0.4%	+0.9%
Large background source	-11.3%	-0.4%	-1%

Table 6.7
% difference in the Flux Norm, Index and Gaussian Width due to various systematic uncertainties.

6.5 Particle Modelling for the Cocoon

GeV γ-rays observed by Fermi-LAT can be produced either by high-energy protons interacting with gas or by high-energy electrons up scattering stellar radiation and dust emission [**?**]. In the following, I will provide more details about the leptonic and hadronic modelling.

6.5.1 Leptonic Modelling

According to the model presented in Figure 6.22, it is unlikely that a single electron population produces γ-rays from GeV to the highest energy by inverse-Compton emission without the corresponding synchrotron radiation violating the flux constraints imposed by radio [12] and X-ray [13] observations. The solid lines in Fig. 6.22 show the spectral energy distribution assuming a leptonic origin. Radio constraints are

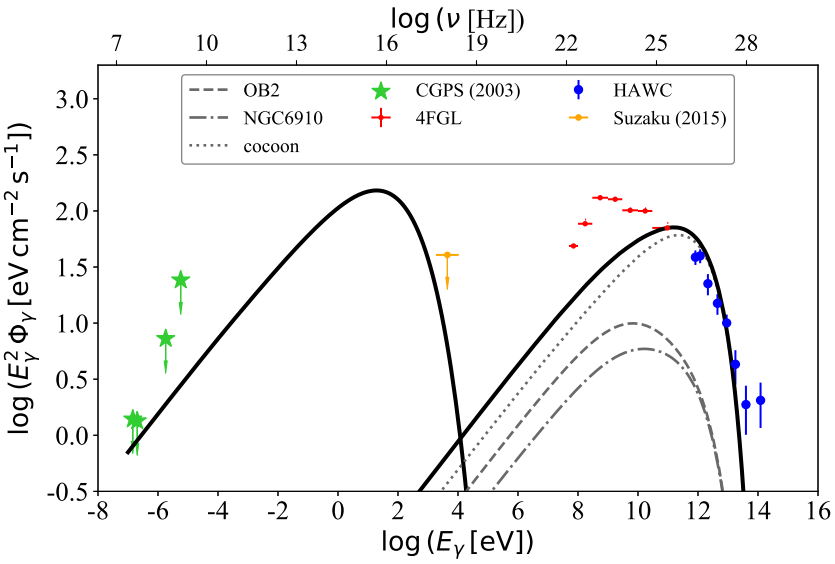

Figure 6.22: GeV-TeV γ-ray spectral energy distribution assuming leptonic origin [9, 11]. Green and Orange data constrain the the radio [12] and X-ray [13] emission due to Synchrotron emission by HE electrons. The black curves correspond to the Synchroton and inverse-Compton emission by an electron population that follows a power-law energy spectrum $dN/dE \propto E^{-2}$ in a magnetic field with $B = 20\,\mu$G [**?**]. Modelling and the plot by Ke Fang [11].

provided by the CGPS survey [12]. An upper limit to the synchrotron emission by relativistic electrons is provided by the Suzaku observations [13]. The second bump in the GeV-TeV regime in the Fig. 6.22 corresponds to inverse-Compton emission at TeV, which is largely suppressed by Klein-Nishina effects. An electron population whose synchroton emission satisfies constraints from the radio and the X-ray observations simultaneously cannot satisfy the GeV and TeV data due to the inverse Compton scattering of the dust radiation. Thus the leptonic origin of the γ-ray radiation by the Cygnus cocoon is disfavored.

6.5.2 Hadronic Modelling

The observed γ-rays are more plausibly produced by hadrons. The break in the γ-ray spectrum around TeV can be either due to leakage of CRs from the cocoon or a cutoff in the CR spectrum. The diffusive propagation of cosmic rays from a source at the center of the Cygnus cocoon can be described by a transport equation [24, 60]:

$$\frac{\partial n(E,r)}{\partial t} = \nabla[D(E,r,t)\,\nabla n(E,r)] + \frac{\partial}{\partial E}[b(E)\,n(E,r)] + Q(E,t)\,\delta(r) \qquad (6.2)$$

Here, the particle distribution function of protons with energy E, with respect to the distance r from the source and at instant t is described by three terms. The first term $\nabla[D(E,r,t)\,\nabla n(E,r)]$ is for the diffusion of the cosmic rays. It occurs in the case when a spatial gradient in the density of particles N(E, r) is different from zero. The total number of particles with energy E at distance r from the the source and at time t is then given by $\nabla[D(E,r,t)\,\nabla n(E,r)]$, where the term $D(E,r,t)$ is the diffusion coefficient. The second term accounts for the energy loss by the protons. The dominant cooling mechanism for the protons above 1 Gev is nuclear interactions. A CR proton may undergo a nuclear interaction with an interstellar H or He nucleus. This encounter can result in a inelastic scattering of the protons. The energy losing rate by this cooling mechanism is described by $b(E) = dE/dt$. The third term $Q(E,t)$ is the particle injection rate which gives the rate at which particles are produced.

6.5.2.1 Transient Source

Consider a starburst event at t_0 that injects particles with a rate of $Q(E,t) = S(E)\,\delta(t-t_0)$, where a CR spectrum, $S(E) \equiv Q_0 E^{-\alpha}\exp\left(-E/E_{\rm cut}\right)$ depends only on energy. When the three terms D, Q and b depend only on energy, the exact solution for equation 6.2 for a δ function type injection rate is provided by Syrovat-skii in [61]. From [61], the solution for the equation $\frac{\partial n(E,r)}{\partial t} - \nabla[D(E,r,t)\,\nabla n(E,r)] - \frac{\partial}{\partial E}[b(E)\,n(E,r)] = Q(E,t)\delta(r)$ can be expressed as

$$n(E,r) = \frac{1}{b(E)}\int_E^\infty dE_i Q(E_i)\frac{\exp[-\mathrm{r}^2/[4\lambda^2(\mathrm{E},\mathrm{E_i})]]}{4\pi\lambda^2(E,E_i)]^{3/2}} \tag{6.3}$$

where,

$$\lambda(E,E_i) = \left[\int_E^{E_i} d\epsilon\,\frac{D(\epsilon)}{b(\epsilon)}\right]^{1/2} \tag{6.4}$$

is the distance traversed by a proton while its energy decreases from E_i to E.

For the injected spectrum $Q(E,t) = Q_0 E^{-\alpha}\exp\left(-E/E_{\rm cut}\right)\delta(t-t_0)$, equation 6.3 can

be written as [11]

$$
\begin{aligned}
n(E, r, t - t_0) &= \frac{1}{b(E)} \int_{t_{cc}}^{t} dt_i b(E_i) Q(E_i) \frac{\exp\left[-r^2/[4\lambda^2(E, E_i)]\right]}{\left(4\pi\lambda^2(E, E_i)\right)^{3/2}} \\
&= \frac{b(E_0)}{b(E)} Q_0 E^{-\alpha} \exp\left(-E/E_{\rm cut}\right) \frac{\exp\left[-r^2/(4\lambda_0^2)\right]}{\left(4\pi\lambda_0^2\right)^{3/2}}
\end{aligned}
\tag{6.5}
$$

to represent the particle distribution at time t due to an episode of emission at t_0. Here, E_0 is the initial energy of a proton at t_0 that has an energy of E after $(t-t_0)$. λ_0 is $\lambda(E, E_0)$ to indicate the distance the particle has traveled when its energy decreases from E_0 to E, or equivalently, from time t_0 to time t.

The OB2 association and its massive O stars are distributed close to the center of the Cygnus cocoon. Summing over the proton density inside the cocoon, assuming that they all come from a source at the center, the total number of cosmic rays from a burst at t_0 is given by [11]

$$
\frac{dN}{dE}(t - t_0) = \frac{b(E_0)}{b(E)} Q(E_0)\, F_{\rm cc}(E, t_0) \tag{6.6}
$$

$$
= \frac{E_0}{E} Q_0 E^{-\alpha} \exp\left(-\mathrm{E}/\mathrm{E_{cut}}\right)\, \mathrm{F_{cc}}(\mathrm{E}, \mathrm{t_0}) \tag{6.7}
$$

where $F_{\rm cc}$ is a function with respect to the radius of the cocoon ($R_{\rm cc} = 50$ pc) and

the time of the burst,

$$F_{\rm cc} = \int_0^{R_{cc}} 4\pi r_s^2 dr_s \frac{\exp\left[-r_s^2/(4\lambda_0^2)\right]}{\left(4\pi\lambda_0^2\right)^{3/2}} \tag{6.8}$$

$$= \mathrm{erf}(\tfrac{R_{\rm cc}}{2\lambda_0}) - \tfrac{1}{\pi^{1/2}} \tfrac{R_{\rm cc}}{\lambda_0} \exp\left[-R_{\rm cc}^2/(4\lambda_0^2)\right] \tag{6.9}$$

Here, r_s is the distance from the source $\leq R_{cc}$. In equation 6.9, the energy loss rate b(E) for the proton-proton interaction is given by

$$bE \equiv \frac{-dE}{dt} \sim \frac{-E}{t_{pp}} = -E n_p \sigma_{pp} c \tag{6.10}$$

where t_{pp} is the interaction time, n_p is the proton density in the Cocoon, and $\sigma_{pp} \sim$ 70 mb is the inelastic scattering cross section of pp interaction between a PeV proton and a rest-mass proton [62]. Therefore, the initial energy can be written as $E_0 = Ee^{b(t-t_0)}$. The distance the proton has travelled, λ_0, can be obtained from equation 6.4, where $\lambda_0 = \left[\int_E^{E_0} d\epsilon \frac{D(\epsilon)}{b(\epsilon)}\right]^{1/2}$ for the parameterization of $D(E) = D_0 E^\delta$ gives $\lambda_0 = \left(\frac{D_0 E^\delta}{b\delta}(e^{\delta b(t-t_0)} - 1)\right)^{1/2}$

Assuming that the turbulent magnetic field and gas density inside the cocoon are roughly constant over time, D and b depend only on energy. Because of strong magnetic turbulence (magnetic field (B) of 20 μG) in the cocoon region, the diffusion

length of particles can be shorter by a factor of 100 than in the standard interstellar medium [**?**]. Hence, $D(E) = 10^{25}(E/1GeV)^{0.55}\mathrm{cm}^2\mathrm{s}^{-1}$ is adopted. The gas density of the Cocoon region is roughly 30 nucleons/cm^3 [63].

The function given by equation 6.7 is fit with the 4FGL Cocoon flux points and HAWC data. The free parameters are index (α) in equation 6.7 and normalization (N) such that Q_0 in equation 6.7 is given by $Q_{arbitrary} \times N$. $Q_{arbitrary}$, an initial guess for the injected power is chosen as 10^{39} erg/s. The best fit value for the N is 0.024 ± 0.005 and for the α is 2.12 ± 0.01. The maximum energy E_{cut} is fixed at $\sim$ 1 PeV. The initial injection rate Q_0 for $t_0 = 0.1$ Myr obtained is $\sim 7 \times 10^{36}$ erg s^{-1}. The best fit proton spectrum is presented in Fig. 6.26 in black.

For the injected spectrum $Q_0 E^{-\alpha}\exp(-\mathrm{E}/\mathrm{E_{cut}})$, the luminosity L_p is then calculated as

$$L_p = \int_{E_{min}}^{E_{max}} Q_0 E^{-\alpha}\exp(-\mathrm{E}/\mathrm{E_{cut}})\mathrm{EdE}. \tag{6.11}$$

For $E_{min} = 1$ GeV and $E_{max} = 1$ PeV and assuming a burst happens at 0.5 Myr with duration of 0.1 Myr, and for a gas density of 30 cm^{-3} calculated from the HI (Fig. 6.23) and HII (Fig. 6.24) observations by [63], the proton injection luminosity

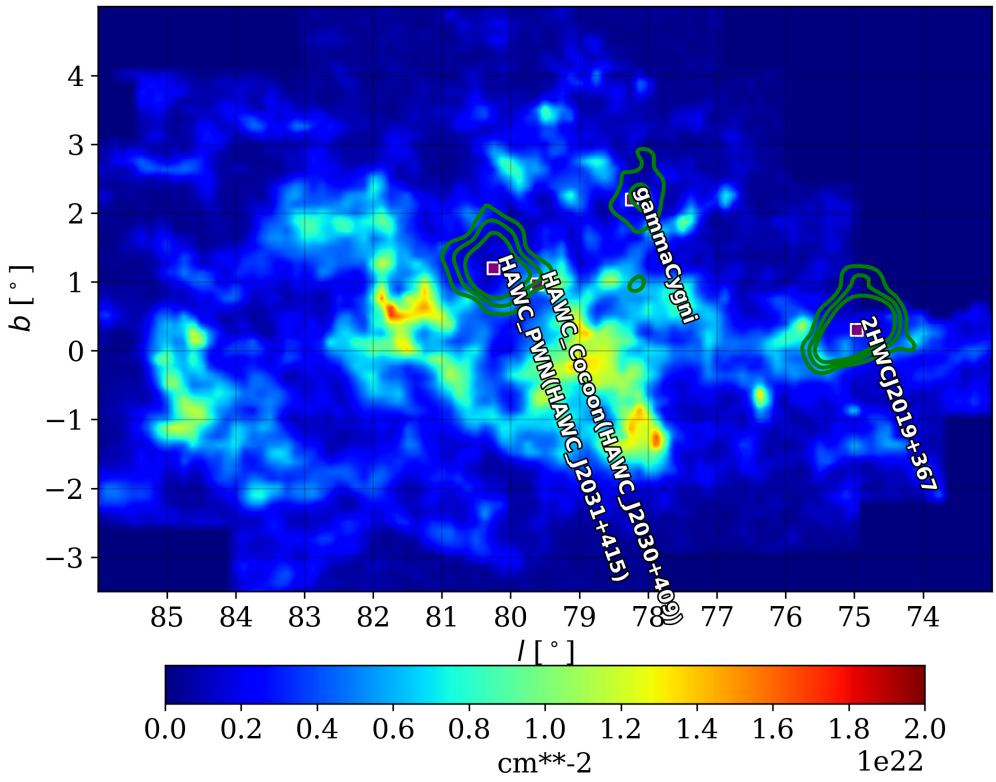

Figure 6.23: HII column density as reported in the DAME survey [14] integrated from -10 km/s to 20 km/s gas velocities. The overlaid green contours are 5, 7, 9 sigma contours from the 1038 days of HAWC data used in this study.

is found to be $L_p \sim 1 \times 10^{37}\,\mathrm{erg\,s^{-1}}$ above 1 GeV.

The protons interact with the ambient gas cloud and produce π^0 which decays into γ rays. The γ-ray flux produced by protons injected at t_0 is

$$\Phi_\gamma(E_\gamma, t) = \frac{c\, n_H}{4\,\pi\, D_{\mathrm{cc}}^2} \int_{E_\gamma}^{\infty} dE_p \sigma_{\mathrm{pp}}(E_p) \left[F_\gamma(\frac{E_p}{E_\gamma}, E_p)\, \frac{1}{E_p} \right] \frac{dN_p}{dE_p}(t - t_0) \tag{6.12}$$

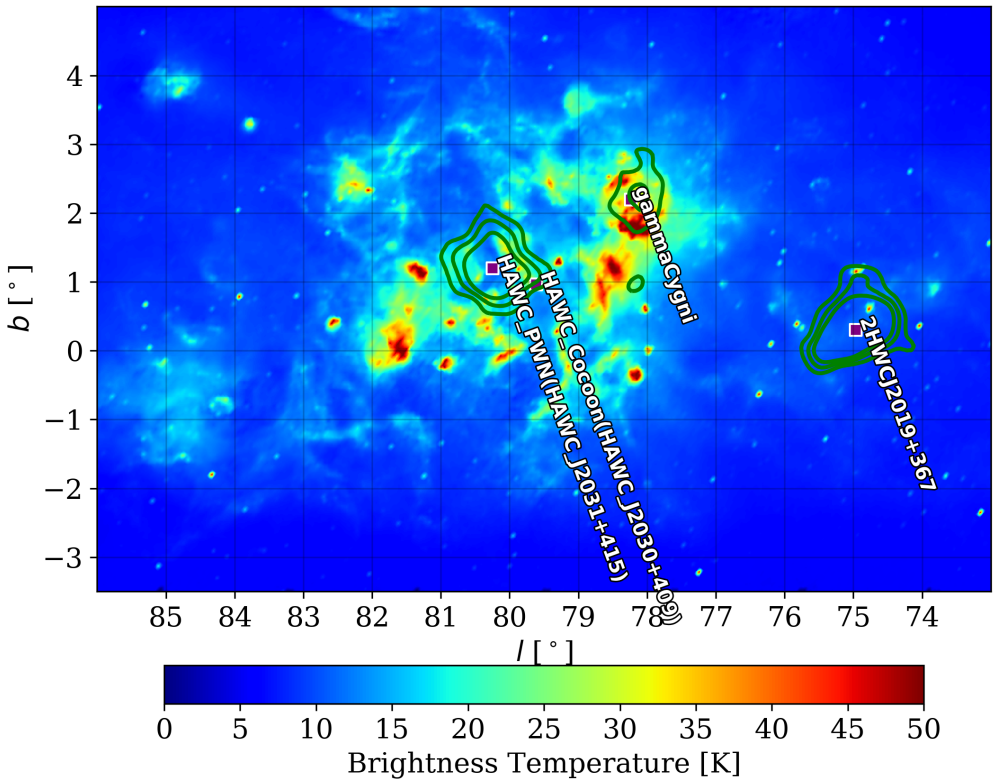

Figure 6.24: Atomic Hydrogen distribution map as reported in the CGPS survey [15] for HI observation. The overlaid green contours are 5, 7, 9 sigma contours from the 1038 days of HAWC data.

where $F_\gamma(E_p/E_\gamma, E_p)$ is the spectrum (dN/dE_γ) produced by one proton with energy E_p through decay of π^0 and η mesons. An analytical form of F_γ is presented in equation 58 of [62].

Fig. 6.25 shows the γ-ray flux from the parent proton flux using the best fit value for the proton injection spectrum in the Cocoon using burst or transient source assumption in grey dashed line.

6.5.2.2 Steady Source

The second case scenario is the continuous injection, $Q(E,t) = Q(E)$. If the source injects particles continuously in time, the cosmic ray flux sums the contribution from different injection episodes.

$$\frac{dN}{dE}(t) = \int_0^{\tau_{cc}} dt_0 \, \frac{E_0}{E} Q_0 E^{-\alpha} \exp\left(-\mathrm{E}/\mathrm{E}_{\mathrm{cut}}\right) \, \mathrm{F}_{\mathrm{cc}}(\mathrm{E}, \mathrm{t}_0) \tag{6.13}$$

where τ_{cc} is the source age and the other variables are as described for the equation 6.7. The equation 6.13 is fit with the 4FGL flux points and HAWC data. Again, the free parameters are normalization (N) where $Q_0 = Q_{arbitrary} \times N$. $Q_{arbitrary}$ is chosen as 10^{39} erg/s, and the index α in equation 6.13. Using $\tau_{\mathrm{cc}} = 3$ Myr, the initial injection rate Q_0 obtained is $\sim 10^{36}$ erg s^{-1}. The best fit α is 1.85 $\pm$ 0.02 and the cutoff is fixed at $\sim$ 60 TeV. The best fit proton spectrum is presented in Fig. 6.26 in purple.

For the steady source, an ISM-like diffusion coefficient, i.e, $D(E) = 10^{28}(E/1GeV)^{0.33}\mathrm{cm}^2\mathrm{s}^{-1}$ is adopted. Using $E_{min} = 1$ GeV and $E_{max} = 60$ TeV, the proton luminosity is calculated to be $L_p = 2.5 \times 10^{38}$ erg s^{-1}. Fig. 6.25 shows the γ-ray flux from the parent proton flux using the best fit value for the proton injection spectrum in the Cocoon using burst or transient source assumption in grey line.

6.5.2.3 Summary of the two models

In the first scenario of a transient CR origin, the γ-ray emission is dominated by very recent starburst activities less than 1 Myr ago. A spectral break is formed when lower-energy CRs are confined by the magnetic field of the cocoon while higher-energy CRs escape from the region. An injection index $\alpha \sim 2.1$ is needed to explain the Fermi-LAT observation. Such a spectrum can be achieved by for example through shock acceleration. This scenario requires that the diffusion length in the cocoon is 100-1000 times shorter than that in the interstellar medium, which is plausible as starburst activities should drive strong magnetic turbulence [**?**]. An example of the leakage model is shown as the solid line in Fig. 6.25. The HAWC data above 100 TeV suggests that the stellar winds inject protons to above PeV with a hard spectrum.

In the second scenario, the γ-ray emission is produced by continuous starburst activities over the OB2 star lifetime, 3-10 Myr and the source emissivity is constant over time. Due to the long duration, protons below TeV also escape from the cocoon, so a very hard spectrum $\alpha \sim 1.6 - 1.8$, depending on the index of the turbulence, is required to meet the γ-ray spectrum $\Gamma \sim 2.1$ at GeV. As illustrated by the dashed curve in Figure 6.25, a cutoff in the injected proton energy around 60 TeV can explain the change of spectral index from GeV to TeV regime. With an ISM-like diffusion coefficient, the scenario requires proton injection luminosity $L_p = 2.5 \times 10^{38}\,\mathrm{erg\,s^{-1}}$

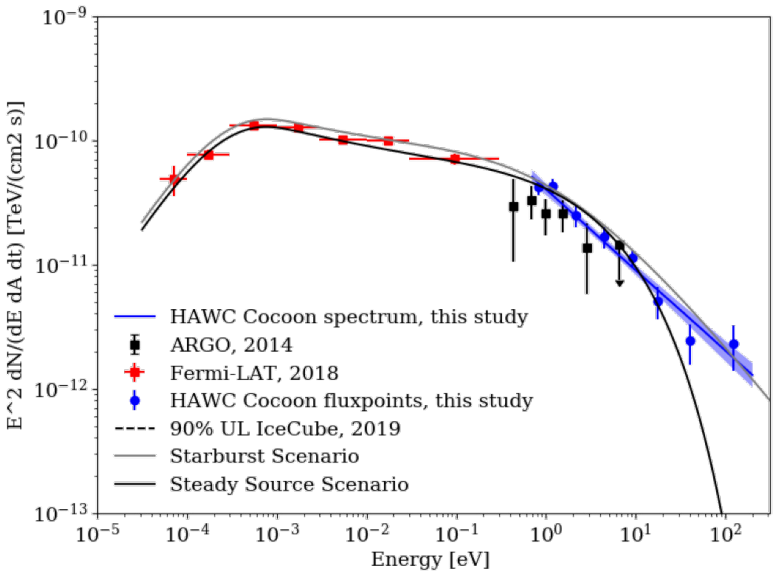

Figure 6.25: Spectral energy distribution of the Cocoon measured by different γ-ray instruments. Blue circles are HAWC spectral measurement for the Cocoon in this study. At lower TeV energies, it agrees with the measurements by the ARGO observatory shown in black squares [8]. The red circles are the latest Fermi-LAT flux points published in the 4FGL catalog [10]. The grey and black lines are γ-ray spectra derived from the hadronic modelling of the region [9]. The grey line represents the burst scenario and the black line represents the steady source scenario.

above 1 GeV. This scenario, however, fails to explain the γ-ray emission above 30 TeV.

For the diffusion parameters used here, the starburst model is preferred by Δ TS of 7 and Δ BIC of 9. However, since the diffusion parameters are estimated and fixed to the given values in the fit, we can not provide conclusive evidence of one model preference over the other with our current statistics. Currently, we are limited by the systematic uncertainties due to the theoretical assumptions.

The HAWC emission from the Cocoon is slightly below the 90% upper limit for γ-ray

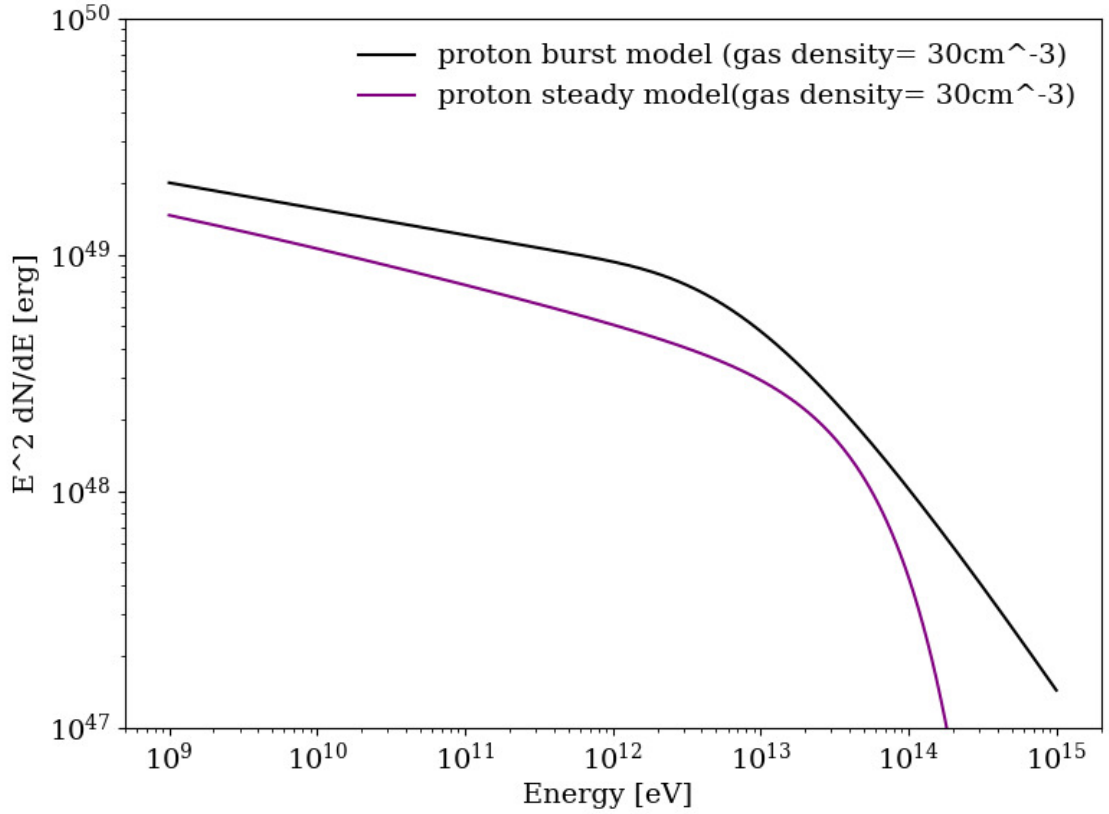

Figure 6.26: Injected proton spectra for the burst (black) and steady state (purple) models.

flux from the IceCube measurement [64]. However, this upper limit was calculated using the IceCube point source analysis. With future extended source analysis, IceCube will be able to provide more information regarding possible sub-dominant contribution to galactic neutrinos from the Cocoon.

6.5.3 CR Density Profile at the Cocoon Region

Similar to the studies done in [65], four rings [0:0.6]°, [0.6:1.2]°, [1.2:1.8]° and [1.8:2.2]° (corresponds to [0:15] pc, [15:29] pc, [29:44] pc and [44:55] pc) centered at the position of the OB2 association (308.3, 41.3)°are chosen as shown in Figure 6.27. The three sources at the Cocoon region are simultaneously fit with the help of the threeML software [16]. From the integral flux (I_{ring}) in each ring from 1 TeV to 200 TeV, the total luminosity of each ring is calculated using

$$L_\gamma = 4\pi I_{ring} * d^2 \tag{6.14}$$

where d is the distance to the OB2 association and assumed to be 1.5 kpc [42]. The gas mass (M) in the region is also used as quoted in [65]. The CR density can then be calculated using

$$w_{CR}(> 10E_\gamma) = 1.8 \times 10^{-2} \left(\frac{\eta}{1.5}\right)^{-1} \frac{L_\gamma(\geq E_\gamma)}{10^{34}\mathrm{erg\,s^{-1}}} \left(\frac{M}{10^6 M_\odot}\right)^{-1} \tag{6.15}$$

where the minimum value for E_γ is 1 TeV. η (a parameter for the heavier than hydrogen nuclei) is assumed to be 1.5. The density values w_{CR} above 10 TeV are given in Table 6.8. Shown in Fig. 6.28 is the projected CR density versus distance from the center of the OB2 association. The CR energy density in all spatial bins

Rings (pc)	$\mathbf{L_\gamma(>0.7TeV)}$erg s^{-1}	$\mathbf{w_{CR}(>7TeV)eV/cm^3}$
$0 < r < 15$	0.7 - 0.5 + 1.6	0.016 - 0.012 + 0.037
$15 < r < 29$	4.5 -0.9 +1.2	0.033 - 0.007 + 0.009
$29 < r < 44$	4.2 - 0.9 +1.4	0.019 - 0.004 + 0.006
$44 < r < 55$	3.0 -1.2 + 2.3	0.017 - 0.006 + 0.012

Table 6.8
Luminosity and Cosmic Ray Density values in the four rings shown with the Eq. 6.14 and Eq. 6.15 respectively [9]. The given uncertainties are statistical uncertainties.

are above the local CR energy density at 10 TeV (black dashed line). Therefore, like GeV γ-rays [**?**], γ-rays above TeV also come from cosmic rays freshly accelerated inside the Cygnus cocoon, rather than from the older Galactic population. The profile does not provide conclusive evidence for a 1/r shape as expected from a continuous injection vs constant profile expected from a burst like injection.

6.5.4 Acceleration efficiency of the OB2

Stars in the mass range of 1 - 20 $M_\odot$ with age $\leq$ 2Myr maintain a wind mechanical luminosity of 2×10^{34} erg s^{-1} continuously [66]. The total mass of the OB2 association is $\sim 3 \times 10^4$ $M_\odot$ [48], and the wind mechanical luminosity is estimated to be $\sim (1-2) \times 10^{39}$ erg s^{-1} [47, 67]. The stellar cluster thus has sufficient power to account for the acceleration of CRs that now make up the Cocoon.

Assuming that 1 - 10 % of the total wind mechanical luminosity is efficiently utilized for particle acceleration power as suggested by our measurement of the Cygnus

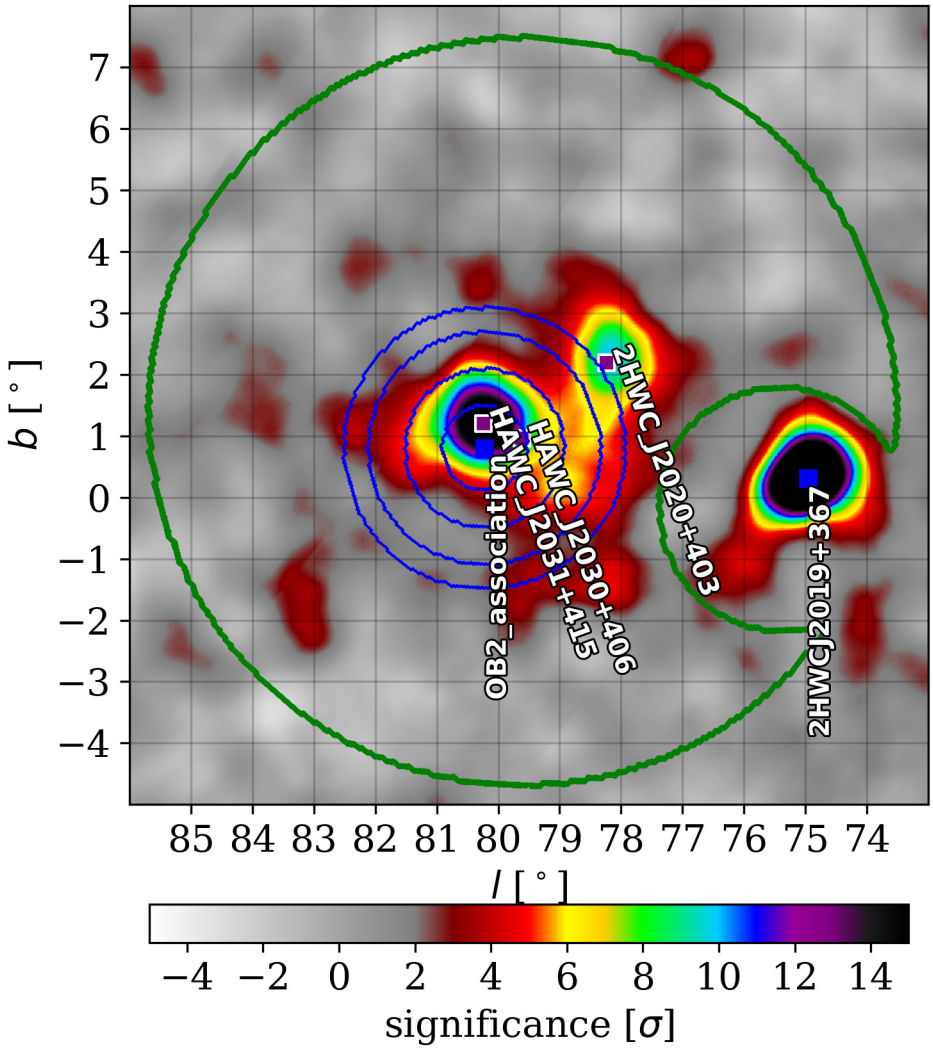

Figure 6.27: Significance map of the cocoon region with a 0.5°extended source assumption and 1038 days of HAWC data. The blue contours are four annuli centered at the OB2 association as listed in Table 6.8. The green line encloses the ROI for this study.

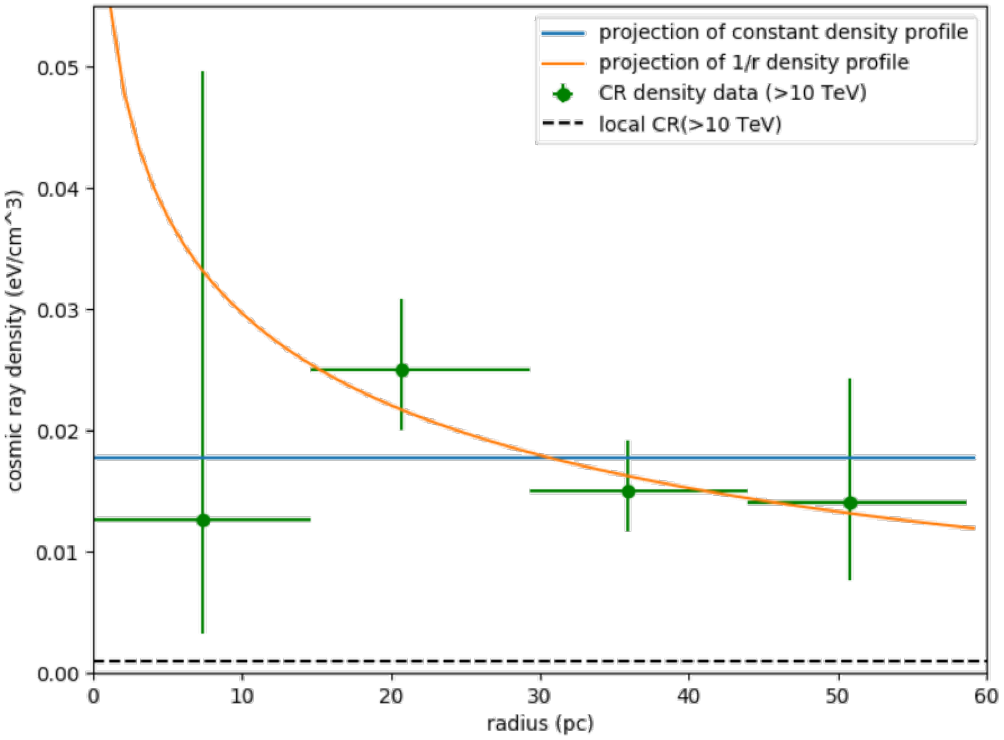

Figure 6.28: CR density $w_{CR} > 10$ TeV is shown as the green points [9]. The orange and blue line are projections of 1/r and constant CR density profiles [9]. The black dashed line is the local CR density above 10 TeV.

cocoon, $10^3 - 10^4$ Cygnus OB2-like stellar associations are needed to generate $(0.3 - 1) \times 10^{41}\,\mathrm{erg\,s^{-1}}$ power to explain the energy density of Galactic CRs [23]. To date, less than 100 OB associations have been identified in the solar neighborhood (up to 3 kpc) of our Galaxy [68, 69], the majority of which are less massive than the Cygnus OB2 association. This challenges the role of massive stellar clusters as dominant contributors to Galactic CRs [65].

6.6 Morphology and Spectral Energy Distribution of the HAWC PWN

The best fit position for the HAWC data is (RA, Dec) = (307.90 ± 0.04, 41.51 ± 0.04)°. The Gaussian width of the source is $(0.276^{+0.026}_{-0.026}\ (\text{stat.})^{+0.002}_{-0.036}\ (\text{syst.}))^{\circ}$. Among the various spectral shapes studies, the spectrum for the HAWC PWN favors a power law spectrum with an exponential cutoff. The best fit flux normalization is $N_0 = 1.35^{+0.21}_{-0.18}\ (\text{stat.})^{+0.14}_{-0.33}\ (\text{syst.}) \times 10^{-13}\ \text{cm}^{-2}\,\text{s}^{-1}\,\text{TeV}^{-1}$. The best fit index is $\Gamma = -1.88^{+0.22}_{-0.22}\ (\text{stat.})^{+0.19}_{-0.26}\ (\text{syst.})$ and the cutoff is obtained at $E_c = 31^{+18}_{-11}\ (\text{stat.})^{+30}_{-6.1}\ (\text{syst.})$ TeV.

A γ-ray source at the HAWC PWN location was first detected by the HEGRA observatory as an unidentified TeV emission and is a possible PWN associated with PSR J2032+4127 according to the VERITAS study [52, 70]. The VERITAS source VER J2031+415 is centered at the same location as 2HWC J2031+415 (within position uncertainties). The emission of VER J2031+415 is best described by asymmetric Gaussian morphology with width of 0.19°±0.02° by 0.08°±0.01°and a power law spectrum with a spectral index of -2 [7, 52]. To support the PWN hypothesis, VERITAS predicted that because of the hard index obtained for this source at VERITAS energies, a cutoff around 10s of TeV must be observed due to Klein-Nishina effects [52].

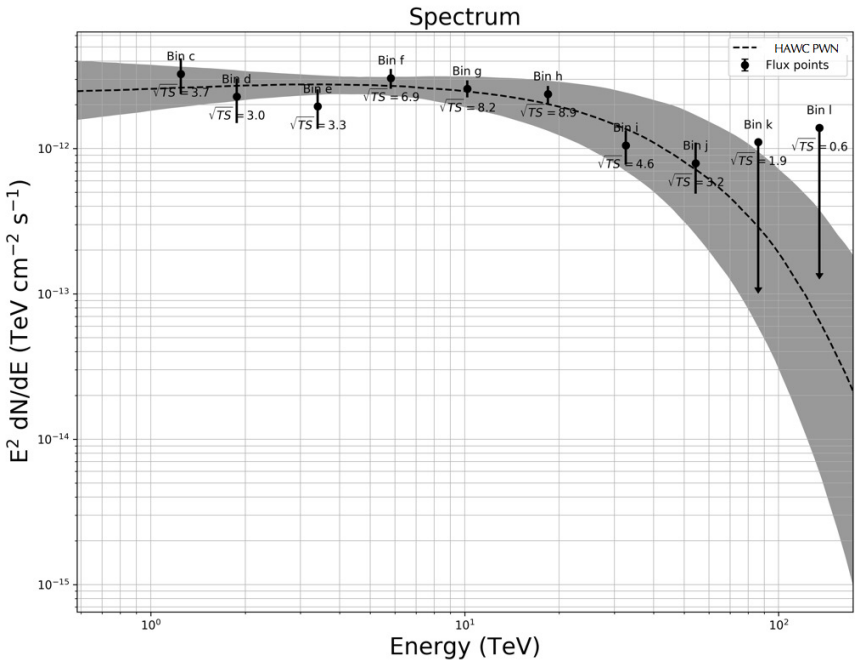

Figure 6.29: Spectral Energy distribution of the HAWC PWN with TS value in each bin.

In HAWC data, the PWN spectral energy distribution is best described by a power law spectrum with an exponential cutoff as shown in Fig. 6.29. Fig. 6.30 shows the HAWC spectrum of the source in comparison with the spectra reported by other observatories. HAWC detects a higher flux in comparison to the fluxes reported by the VERITAS, HEGRA and MAGIC observatories and also fits the cutoff (E_c) at a few tens of TeV favoring the PWN interpretation.

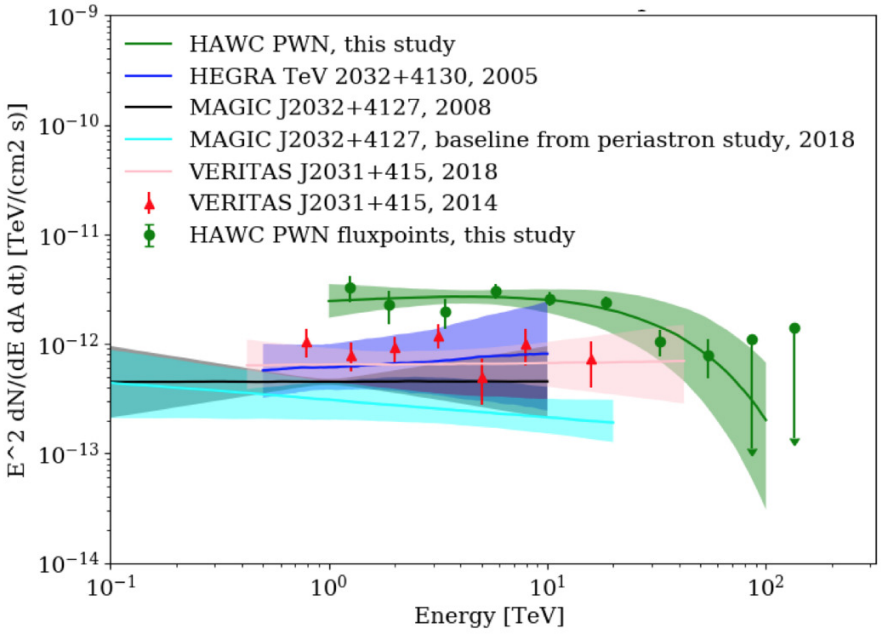

Figure 6.30: PWN spectra measured by various γ-ray instruments.

Detector Systematic	**Flux Norm** $\times 10^{-13}$ ($\mathrm{TeV}^{-1}\mathrm{cm}^{-2}\mathrm{s}^{-1}$)	**Index**	**Gaussian Width** (deg.)	**Cutoff** (TeV)
Threshold	-0.03 +0.01	-0.04 +0.08	-0.01 0	-3 +2
PMT efficiency	0.03	+0.14	-0.08	-3 +1
Broad pulse	-0.14 +0.08	-0.11 +0.05	-0.02	-3 +10
Charge uncertainty	-0.27 +0.11	-0.20 +0.08	-0.02 +0.01	-3 +24
Angular resolution	+0.01	-0.01	-0.04	0

Table 6.9
Contribution to systematic uncertainties from various detector effects for the PWN parameters.

Systematic	Flux Norm $\times 10^{-13}$ ($TeV^{-1}cm^{-2}s^{-1}$)	Index	Gaussian Width (degree)	Cutoff (TeV)
NN bins	-0.11	-0.12	-0.034	+15
Larger ROI	-0.03	+0.02	-0.005	-1
Large uniform disk background	+0.02	-0.01	+0.001	0
Large Gaussian background	+0.02	-0.02	+0.002	+1

Table 6.10
Difference in the values for the PWN spectral and morphological function parameters: Flux Norm, Index, Gaussian Width, and Cutoff for the HAWC PWN.

Contribution	Flux Norm %	Index %	Gaussian Width %	Cutoff %
Detector effects	±10%	+10% -12%	+0.4% -3%	+72% -19%
Using NN bins	-8%	-6%	-12%	+44%
Larger ROI	-2%	+1.1%	-1.8%	-3%
Large background source	+3%	-1.6%	+1.1%	-3%

Table 6.11
% contribution to systematic uncertainties from various detector effects.

6.6.1 Total Systematic Uncertainties

The total systematic uncertainties in the flux norm, the index, the cutoff, and the Gaussian width are calculated by adding all contributions listed in Table 6.9 and Table 6.10 in quadrature and are listed in Table 6.11.

Chapter 7

Conclusions

7.1 Summary

I studied the source confused 2HWC J2031+415 region which has never been fit at TeV energies using a multi-source model approach. Using 1038 days HAWC data and a new energy estimator ρ_{40}, I disentangle the contribution of two gamma ray sources of TeV emission detected in the region. In this thesis, I provided the detailed morphological and spectral description of the two sources: HAWC J2030+406 (HAWC Cocoon) and HAWC J2031+415 (HAWC PWN).

HAWC J2030+406 is the TeV counterpart of the Fermi-LAT Cocoon detected at GeV energies. The spectral energy distribution of the Cocoon has been extended

from the last highest measurement at 3 TeV [8] to now 200 TeV with this study. The HAWC measurement above 0.7 TeV can be best described by a power-law spectrum $dN/dE = N_0 \, (E/E_0)^{\Gamma}$, with $E_0 = 4.2$ TeV as pivot energy. The best fit flux normalization and spectral index are $N_0 = 9.5^{+1.1}_{-0.9}\,(\text{stat.})^{+0.93}_{-1.23}\,(\text{syst.}) \times 10^{-13}$ cm^{-2} s^{-1} TeV^{-1} and $\Gamma = -2.64^{+0.05}_{-0.05}\,(\text{stat.})^{+0.09}_{-0.03}\,(\text{syst.})$, respectively. The flux is consistent with an extension from the Fermi-LAT measurement at 1-100 GeV [10**?**]. Compared to the measurement of $\Gamma \sim 2.1$ in the Fermi-LAT data, a significant softening of the spectral shape is evident at a few TeV in the ARGO-YBJ data [8], and is found to persist beyond 100 TeV in the HAWC data. The leptonic origin has been ruled out and to explain the GeV-TeV spectrum, two hadronic models are presented.

The spectral softening from GeV to TeV range can be explained by either a hadronic scenario with a recent star burst activity or a steady source emission with a cutoff. In the case of the recent starburst, there could be particle acceleration up to PeV energies. In the case of a steady source emission, the source would be no longer a Pevatron and we do not expect a significant flux above 100 TeV. The emission we detect could be a combination of these two origin scenarios. Although my studies statistically prefer the star burst scenario, currently we are unable to conclusively distinguish between the two hadronic scenarios.

The other source HAWC J2031+415 is a PWN associated with the pulsar PSR J2032+4127. In this study, for the first time the cutoff of the PWN is measured

at a few tens of TeV which was predicted by a previous VERITAS study. The cut-off is obtained at $E_c = 31^{+18}_{-11}$ (stat.)$^{+30}_{-6.1}$ (syst.) TeV. The best fit flux normalization and spectral index are $N_0 = 1.35^{+0.21}_{-0.18}$ (stat.)$^{+0.14}_{-0.33}$ (syst.) $\times 10^{-13}$ cm^{-2} s^{-1} TeV^{-1} and $\Gamma = -1.88^{+0.22}_{-0.22}$ (stat.)$^{+0.19}_{-0.26}$ (syst.), respectively. The Gaussian width of the source is $(0.276^{+0.026}_{-0.026}$ (stat.)$^{+0.002}_{-0.036}$ (syst.))$^\circ$. The flux measured is higher than that by IACTs which can be explained by the larger extent of the source. Further study of the systematic between the IACTs and HAWC γ-ray instruments is needed to understand the difference in morphology.

7.2 Future Outlook

In addition to the main array discussed here, the HAWC observatory has added 350 smaller (1.65 m high and 1.55 m wide) WCDs surrounding the main array. They are called outriggers and each of these WCDs contains an 8-inch PMT [71]. The outrigger array is estimated to improve the high-energy sensitivity of HAWC above 10 TeV by up to four times. With the increased sensitivity, we may be able to conclusively distinguish the hadronic models presented here for the HAWC Cocoon and provide additional information about the high energy behaviour of the HAWC PWN.

7.2.1 PWNs

The morphology difference between the various instruments requires a detailed multi-wavelength study of the source to understand the systematic differences between the detectors. Also the detailed study of the particle modelling of the PWN is needed to understand the origin of this PWN and the physics processes in the environment.

7.2.2 OB Associations

This study reveals the emission of the Cygnus cocoon, a representative of one of the most plausible Galactic cosmic-ray source classes, Star Forming Regions, at the highest γ-ray energy. The detection of above 100 TeV γ-rays unambiguously probes hadron acceleration beyond PeV. This measurement also suggest that the Cygnus cocoon can emit high-energy neutrinos and may be identified through an extended source analysis by IceCube and future neutrino experiments.

I recommend the detailed study of the other source possibly associated with the stellar association 2HWC J1847-018. Additionally, SWGO (the Southern Wide field γ-ray Observatory) will be able to able to study sources associated with stellar associations such as Westerlund 1 and Westerlund 2 that are not in HAWC's field of view. The upgraded HAWC, SWGO, LHAASO and other future VHE γ-ray observation will

provide more statistics and additional information about the stellar associations which can resolve the contribution of other stellar clusters to GCRs around the knee.

References

[1] M. S. Longair. 3 edition, 2011.

[2] L. Bergström F. Aharonian and C. Dermer. 2013.

[3] A. U. Abeysekara et al. The 2HWC HAWC Observatory Gamma-Ray Catalog. *ApJ*, 843(40), 2017.

[4] A. U. Abeysekara et al. Observation of the Crab Nebula with the HAWC Gamma-Ray Observatory. *ApJ*, 843(1):39, Jul 2017.

[5] N. Schneider, S. Bontemps, R. Simon, H. Jakob, F. Motte, M. Miller, C. Kramer, and J. Stutzki. A new view of the Cygnus X region. *A&A*, 458(3):855–871, Nov 2006.

[6] M. Ackermann et al. A Cocoon of Freshly Accelerated Cosmic Rays Detected by Fermi in the Cygnus Superbubble. *Science*, 334, 2011.

[7] A. U. Abeysekara et al. A Very High Energy γ-Ray Survey toward the Cygnus Region of the Galaxy. *ApJ*, 861(2):134, Jul 2018.

[8] B. Bartoli et al. Identification of the TeV Gamma-Ray Source ARGO J2031+4157 with the Cygnus Cocoon. *ApJ*, 790(2):152, Aug 2014.

[9] B. Hona and others for the HAWC Collaboration. Particle Acceleration in the Cygnus OB2. *Paper in preparation*, 2020.

[10] The Fermi-LAT collaboration. Fermi Large Area Telescope Fourth Source Catalog. *arXiv e-prints*, page arXiv:1902.10045, Feb 2019.

[11] Ke Fang. Private communication, 2019.

[12] A. R. Taylor et al. The Canadian Galactic Plane Survey. , 125(6):3145–3164, Jun 2003.

[13] T. Mizuno et al. Suzaku Observation of the Fermi Cygnus Cocoon: The Search for a Signature of Young Cosmic-Ray Electrons. *ApJ*, 803(2):74, Apr 2015.

[14] T. M. Dame, Dap Hartmann, and P. Thaddeus. The Milky Way in Molecular Clouds: A New Complete CO Survey. , 547(2):792–813, Feb 2001.

[15] A. R. Taylor, S. J. Gibson, M. Peracaula, P. G. Martin, T. L. Landecker, C. M. Brunt, P. E. Dewdney, S. M. Dougherty, A. D. Gray, L. A. Higgs, C. R. Kerton, L. B. G. Knee, R. Kothes, C. R. Purton, B. Uyaniker, B. J. Wallace, A. G. Willis, and D. Durand. The Canadian Galactic Plane Survey. , 125(6):3145–3164, Jun 2003.

[16] Giacomo Vianello et al. The Multi-Mission Maximum Likelihood framework (3ML). *arXiv e-prints*, page arXiv:1507.08343, Jul 2015.

[17] Adrian E. Raftery and Robert E. Kass. Bayes factors. *Journal of the American Statistical Association*, 90(430):773–795, Jun. 1995.

[18] Victor F. Hess. Uber Beobachtungen der durchdringenden Strahlung bei sieben Freiballonfahrten. *Phys. Z.*, 13:1084–1091, 1912.

[19] Johannes Blümer, Ralph Engel, and Jörg R. Hörandel. Cosmic rays from the knee to the highest energies. *Progress in Particle and Nuclear Physics*, 63(2):293–338, Oct 2009.

[20] F. Aharonian et al. Primary particle acceleration above 100 TeV in the shell-type supernova remnant ¡ASTROBJ¿RX J1713.7-3946¡/ASTROBJ¿ with deep HESS observations. , 464(1):235–243, Mar 2007.

[21] A. R. Bell. The acceleration of cosmic rays in shock fronts - I. , 182:147–156, Jan 1978.

[22] F. A. Aharonian. *Very high energy cosmic gamma radiation : a crucial window on the extreme Universe*. World Scientific Publishing Co, 2004.

[23] Luke O. 'C. Drury. Origin of cosmic rays. *Astroparticle Physics*, 39:52–60, Dec 2012.

[24] V. L. Ginzburg and S. I. Syrovatskii. *The Origin of Cosmic Rays*. 1964.

[25] J.B. Tjus et al. Gamma-ray emitting supernova remnants as the origin of Galactic cosmic rays? *Astroparticle Physics*, 81:1–11, 2016.

[26] C.J. Cesarsky and T. Montmerle. Gamma rays from active regions in the galaxy: The possible contribution of stellar winds. *Space Sci. Rev.*, 237:236, 1983.

[27] G. E. Romero. Gamma Rays from Star-Forming Regions. In *AIP Conference Proceedings*, volume 1085, 2008.

[28] J.P. Cassinelli. Stellar Winds. *ARAandA*, 17(275), 1979.

[29] A. M. Bykov. Particle Acceleration and Nonthermal Phenomena in Superbubbles. *Space Sci. Rev*, 99(317), 2001.

[30] M. Casse and J. A. Paul. Local gamma rays and cosmic-ray acceleration by supersonic stellar winds. *ApJ*, 237:236–243, April 1980.

[31] J. Marti et al. HESS Observations of Massive Stellar Clusters. In *ASP Conference Series*, volume 422, 2010.

[32] Ruben Lopez-Coto. *Very-high-energy gamma-ray observations of pulsar wind nebulae and cataclysmic variable stars with MAGIC and development of trigger systems for IACTs*. PhD thesis, Universitat Autonoma de Barcelona, Jul 2015.

[33] M. de Groot. BOOKS (with comments): "Pulsars", by R. N. Manchester and J. H. Taylor. *Irish Astronomical Journal*, 13:142, Sep 1977.

[34] A. U. Abeysekara et al. Measurement of the Crab Nebula at the Highest Energies with HAWC. *arXiv e-prints*, page arXiv:1905.12518, May 2019.

[35] Hao Zhou. *Search for TeV Gamma-Ray Sources in the Galactic Plane with the HAWC Observatory*. PhD thesis, Michigan Technological University, 2015.

[36] Hugo A. A. Solares. *Search for High-Energy Gamma Rays in the Northern Fermi Bubble Region with the HAWC Observatory*. PhD thesis, Michigan Technological University, 2017.

[37] A. M. Hillas, D. J. Marsden, J. D. Hollows, and H. W. Hunter. Measurement of Primary Energy of Air Showers in the Presence of Fluctuations. In *12th International Cosmic Ray Conference (ICRC12), Volume 3*, volume 3 of *International Cosmic Ray Conference*, page 1001, Jan 1971.

[38] Kelly Malone. *A SURVEY OF THE HIGHEST-ENERGY ASTROPHYSICAL SOURCES WITH THE HAWC OBSERVATORY*. PhD thesis, Pennsylvania State University, 2018.

[39] A. Hoecker et al. Tmva - toolkit for multivariate data analysis, 2007.

[40] Samuel S. Marinelli. *CONSTRAINTS ON LORENTZ-INVARIANCE VIOLATION WITH THE HAWC OBSERVATORY*. PhD thesis, Michigan State University, 2019.

[41] B. Reipurth and N. Schneider. *Star Formation and Young Clusters in Cygnus*, page 36. December 2008.

[42] J. Knödlseder, M. Cerviño, J. M. Le Duigou, G. Meynet, D. Schaerer, and P. von Ballmoos. Gamma-ray line emission from OB associations and young open clusters. II. The Cygnus region. , 390:945–960, Aug 2002.

[43] Motte. F. et al. The earliest phases of high-mass star formation: a 3 square degree millimeter continuum mapping of cygnus x. *A&A*, 476:1243–1260, Jul 2007.

[44] Uyaniker, B. et al. The cygnus superbubble revisited. *A&A*, 371(2):675–697, 2001.

[45] J. Bally, W. D. Langer, A. A. Stark, and R. W. Wilson. Filamentary structure in the Orion molecular cloud. , 312:L45–L49, January 1987.

[46] N. Schneider and K. Brooks. The Bias of Molecular Clump Identification Programs: the Example of the Carina Molecular Clouds. *Publications of the Astronomical Society of Australia*, 21:290–301, 2004.

[47] J. Knödlseder. Cygnus OB2 - a young globular cluster in the Milky Way. *aap*, 360:539–548, Aug 2000.

[48] N. J. Wright, J. J. Drake, J. E. Drew, and J. S. Vink. The Massive Star-Forming

Region Cygnus OB2. II. Integrated Stellar Properties and the Star Formation History. *ApJ*, 713(2):871–882, Apr 2010.

[49] Nicholas J. Wright, Janet E. Drew, and Michael Mohr-Smith. The massive star population of Cygnus OB2. *MNRAS*, 449(1):741–760, May 2015.

[50] A. A. Abdo et al. Spectrum and Morphology of the Two Brightest Milagro Sources in the Cygnus Region: MGRO J2019+37 and MGRO J2031+41. *ApJ*, 753(2):159, Jul 2012.

[51] Aharonian, F. et al. The unidentified tev source (tev j2032+4130) and surrounding field: Final hegra iact-system results. *A&A*, 431(1):197–202, 2005.

[52] E. Aliu et al. Observations of the unidentified gamma-ray source TeV J2032+4130 by VERITAS. *ApJ*, 783, 2014.

[53] A. G. Lyne et al. The binary nature of PSR J2032+4127. , 451:581–587, July 2015.

[54] A. U. Abeysekara et al. Periastron Observations of TeV Gamma-Ray Emission from a Binary System with a 50-year Period. , 867(1):L19, Nov 2018.

[55] S. S. Wilks. The large-sample distribution of the likelihood ratio for testing composite hypotheses. *Ann. Math. Statist.*, 9(1):60–62, 03 1938.

[56] Gideon Schwarz. Estimating the dimension of a model. *Ann. Statist.*, 6(2):461–464, 03 1978.

[57] H. Fleischhack for the HAWC Collaboration. Multi-wavelength modeling of gamma Cygni. In *PoS*, volume 36th ICRC, 2019.

[58] A. U. Abeysekara et al. Extended gamma-ray sources around pulsars constrain the origin of the positron flux at Earth. *Science*, 358(6365):911–914, Nov 2017.

[59] Chad Brisbois. *UNDERSTANDING THE VERY HIGH ENERGY γ-RAY EMISSION FROM A FAST SPINNING NEUTRON STAR ENVIRONMENT*. PhD thesis, Michigan Technological University, 2019.

[60] A. M. Atoyan, F. A. Aharonian, and H. J. Völk. Electrons and positrons in the galactic cosmic rays. *Phys. Rev. D*, 52:3265–3275, Sep 1995.

[61] S. I. Syrovatskii. The Distribution of Relativistic Electrons in the Galaxy and the Spectrum of Synchrotron Radio Emission. , 3:22, Feb 1959.

[62] S. R. Kelner, F. A. Aharonian, and V. V. Bugayov. Energy spectra of gamma rays, electrons, and neutrinos produced at proton-proton interactions in the very high energy regime. *Physical Review D*, 74(3):034018, Aug 2006.

[63] Y. Butt. Beyond the myth of the Supernovaremnant origin of Cosmic Rays. *Nature*, 460:701, 2009.

[64] A. Kheirandish and J. Wood. IceCube Search for Galactic Neutrino Sources based on HAWC Observations of the Galactic Plane. In *PoS*, volume 36th ICRC, 2019.

[65] Felix Aharonian, Ruizhi Yang, and Emma de Oña Wilhelmi. Massive stars as major factories of Galactic cosmic rays. *Nature Astronomy*, 3:561–567, Mar 2019.

[66] C. Leitherer, C. Robert, and L. Drissen. Deposition of mass, momentum, and energy by massive stars into the interstellar medium. *ApJ*, 401:596–617, December 1992.

[67] T. A. Lozinskaya, V. V. Pravdikova, and A. V. Finoguenov. Searches for the Shell Swept up by the Stellar Wind from Cyg OB2. *Astronomy Letters*, 28:223–236, April 2002.

[68] A. M. Mel'Nik and Yu. N. Efremov. A new list of OB associations in our galaxy. *Astronomy Letters*, 21(1):10–26, Jan 1995.

[69] N. V. Kharchenko, A. E. Piskunov, E. Schilbach, S. Röser, and R. D. Scholz. Global survey of star clusters in the Milky Way. II. The catalogue of basic parameters. *AAP*, 558:A53, Oct 2013.

[70] F. Aharonian et al. An unidentified TeV source in the vicinity of Cygnus OB2. , 393:L37–L40, Oct 2002.

[71] V. Joshi and A. for the HAWC collaboration Jardin-Blicq. HAWC High Energy Upgrade with a Sparse Outrigger Array. In *PoS*, volume 35th ICRC, 2017.

[72] J for the HAWC Collaboration Linnemann. In *PoS*, volume 36th ICRC, 2019.

[73] The atnf pulsar database. http://www.atnf.csiro.au/people/pulsar/psrcat. Accessed: 2018-2-15.

[74] B. Hona. Correlated GeV-TeV Gamma-Ray Emission from Extended Sources in the Cygnus Region. In *PoS*, volume 35th ICRC, 2017.

[75] N. J. Wright et al. The Massive Star-Forming Region Cygnus OB2. I. Chandra Catalog of Association Members. *ApJS*, 184:84, 2009.

[76] A. Abramowski et al. The exceptionally powerful tev -ray emitters in the large magellanic cloud. *Science*, 347(6220):406–412, 2015.

[77] Mathieu de Naurois and H. E. S. S. Collaboration. The Galactic Sky seen by H.E.S.S. *Advances in Space Research*, 51(2):258–267, Jan 2013.

[78] S. Ohm, D. Horns, O. Reimer, J. Hinton, G. Rowell, E. O. Wilhelmi, M. V. Fernandes, F. Acero, and A. Marcowith. H.E.S.S. Observations of Massive Stellar Clusters. In J. Martí, P. L. Luque-Escamilla, and J. A. Combi, editors, *High Energy Phenomena in Massive Stars*, volume 422 of *Astronomical Society of the Pacific Conference Series*, page 265, May 2010.

[79] V. Zabalza. Naima: a Python package for inference of particle distribution properties from nonthermal spectra. In *34th International Cosmic Ray Conference (ICRC2015)*, volume 34 of *International Cosmic Ray Conference*, page 922, Jul 2015.

[80] M. Ajello et al. 3FHL: The Third Catalog of Hard Fermi-LAT Sources. *ApJS*, 232(2):18, Oct 2017.

[81] A. Abramowski et al. Acceleration of petaelectronvolt protons in the Galactic Centre. *NAT*, 531(7595):476–479, Mar 2016.

[82] M. Ackermann et al. A Cocoon of Freshly Accelerated Cosmic Rays Detected by Fermi in the Cygnus Superbubble. *Science*, 334(6059):1103, Nov 2011.

[83] Vladimir Ptuskin. Cosmic ray transport in the Galaxy. In *Journal of Physics Conference Series*, volume 47, pages 113–119, Oct 2006.

[84] I. M. Beerer et al. ASPITZERVIEW OF STAR FORMATION IN THE CYGNUS x NORTH COMPLEX. *The Astrophysical Journal*, 720(1):679–693, aug 2010.

Appendix A

Units

$1 \text{ eV} = 1.60218 \times 10^{-12} \text{ erg}$

$10^3 \text{ eV} = 1 \text{ KeV}(\text{Kilo} - \text{eV})$

$10^6 \text{ eV} = 1 \text{ MeV}(\text{Mega/Million} - \text{eV})$

$10^9 \text{ eV} = 1 \text{ GeV}(\text{Giga} - \text{eV})$

$10^{12} \text{ eV} = 1 \text{ TeV}(\text{Tera} - \text{eV})$

$10^{15} \text{ eV} = 1 \text{ PeV}(\text{Peta} - \text{eV})$

Appendix B

Corner plot with Bayesian Analysis

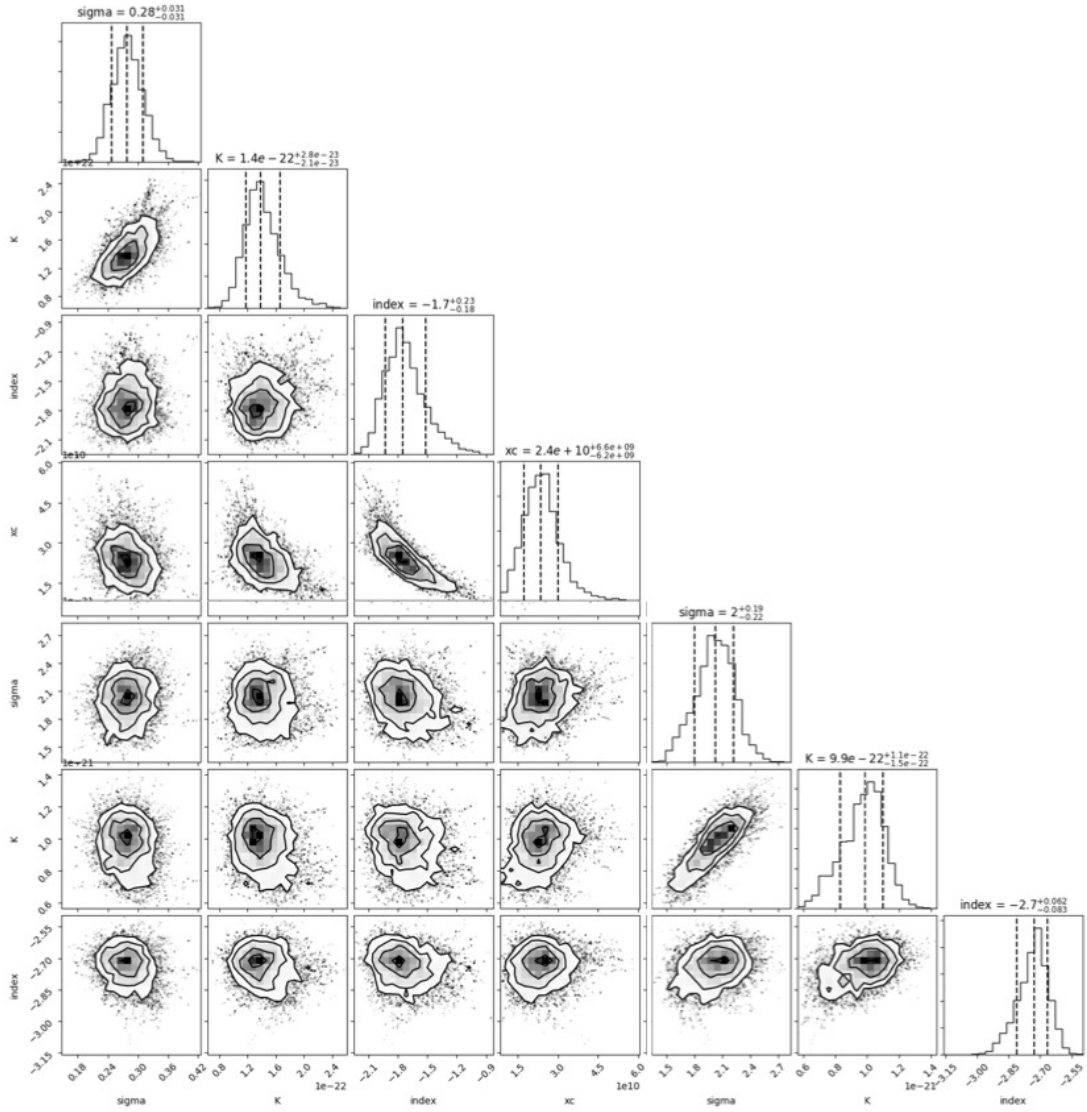

Figure B.1: Corner plot from the Bayesian analysis method showing the posterior probability distribution for the Bayesian model parameters: Gaussian width of the PWN, N_0, Γ, E_c for the PWN from the equation 5.3 and the Gaussian width of the HAWC Cocoon plus N_0, Γ for the HAWC Cocoon from the equation 5.2. The parameters are listed as they appear for the each row of the plot in the figure. For each parameter 2D contours and 1D distribution are shown. The black contours in the 2D contour plots are $1\sigma, 2\sigma and 3\sigma$ contours. In the 1D distribution, the middle black dashed line corresponds to the median of the distribution and the other two black dashed lines show 68% distribution. This plot was made using the threeML [16] software for number of walkers=50, number of burn in samples =100, number of samples=450.

Appendix C

SED of the three Sources

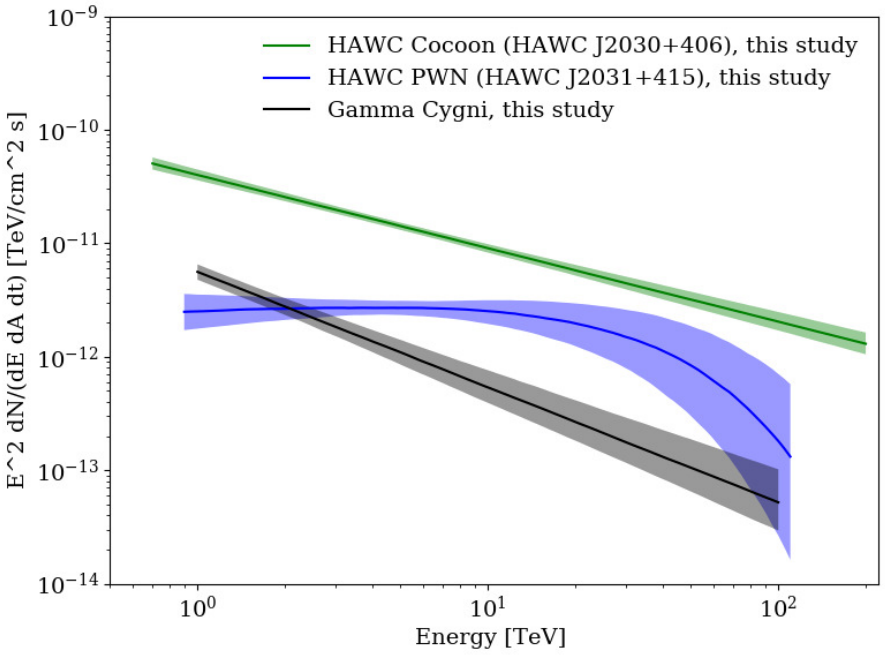

Figure C.1: Spectral energy distribution of the three sources in the ROI. **Green**: HAWC Cocoon, **blue**: HAWC PWN and **black**: Gamma Cygni. Uncertainties shown are only statistical.

Appendix D

Projected Density for 1/r CR Profile

Consider a spherically symmetric system shown in the Figure D.1

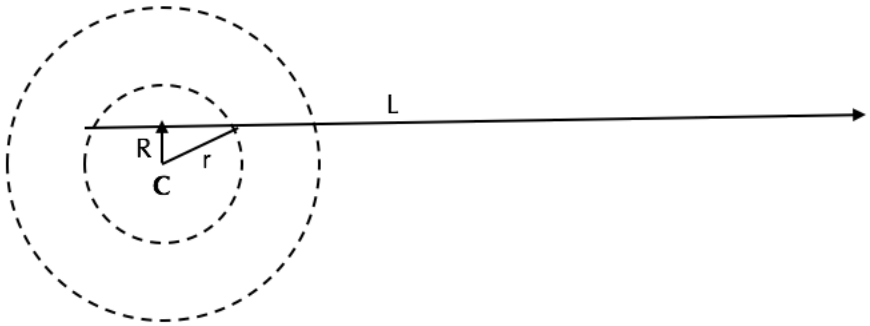

Figure D.1: Schematic of the spherically symmetric sphere and an observer at a distance for the projected density calculation

An observer, at large distance, observes the projected density distribution where,

L = distance along the line of sight

R = Projected radius from the center C

$r = \sqrt{L^2 + R^2}$

Then, averaging CR density ($w_{CR}(r)$) along L axis,

$$w_{CR}(> E, R) = \frac{1}{2L_{max}} \int_{-L_{max}}^{L_{max}} w_{CR}(> E, r) dL \tag{D.1}$$

$$\text{where, } \mathrm{L_{max}} = \sqrt{\mathrm{r_0^2 - R^2}} \tag{D.2}$$

$$\text{where, } \mathrm{r_0} \text{ is used as the radius of the sphere.} \tag{D.3}$$

$$Since, w_{CR}(> E, r) \sim \frac{1}{r} \tag{D.4}$$

$$w_{CR}(> E, R) = \frac{2}{2L_{max}} \int_{0}^{L_{max}} \frac{1}{\sqrt{L^2 + R^2}} \tag{D.5}$$

$$= \frac{1}{\sqrt{r_0^2 - R^2}} asinh \left(\frac{\sqrt{r_0^2 - R^2}}{R} \right) \tag{D.6}$$

$$\text{Using } \sinh^{-1}\mathrm{z} = \ln(\mathrm{z} + \sqrt{1 + \mathrm{z}^2}), \text{we get;} \tag{D.7}$$

$$w_{CR}(> E, R) = \frac{1}{\sqrt{r_0^2 - R^2}} ln \left(\frac{\sqrt{r_0^2 - R^2}}{R} + \sqrt{1 + \frac{r_0^2 - R^2}{R^2}} \right) \tag{D.8}$$

$$= \frac{1}{\sqrt{r_0^2 - R^2}} ln \left(\frac{\sqrt{r_0^2 - R^2}}{R} + \frac{r_0}{R} \right) \tag{D.9}$$

$$= \frac{1}{\sqrt{r_0^2 - R^2}} ln \left(r_0 + \sqrt{r_0^2 - R^2)/R} \right) \tag{D.10}$$